12-2009

Development and Implementation of a New Technique to Study (p,α) Reactions Relevant to Nucleosynthesis in Binary Systems

Brian Hossain Moazen
University of Tennessee - Knoxville

To the Graduate Council:

I am submitting herewith a dissertation written by Brian Hossain Moazen entitled "Development and Implementation of a New Technique to Study (p,α) Reactions Relevant to Nucleosynthesis in Binary Systems." I have examined the final electronic copy of this dissertation for form and content and recommend that it be accepted in partial fulfillment of the requirements for the degree of Doctor of Philosophy, with a major in Physics.

Kate Grzywacz-Jones, Major Professor

We have read this dissertation and recommend its acceptance:

Witek Nazarewicz, Mike Guidry, Larry Townsend

Accepted for the Council:
Carolyn R. Hodges

Vice Provost and Dean of the Graduate School

(Original signatures are on file with official student records.)

To the Graduate Council:

I am submitting herewith a dissertation written by Brian Moazen entitled "Development and Implementation of a New Technique to Study (p,α) Reactions Relevant to Nucleosynthesis in Binary Systems." I have examined the final electronic copy of this dissertation for form and content and recommend that it be accepted in partial fulfillment of the requirements for the degree of Doctor of Philosophy, with a major in Physics.

Kate Grzywacz-Jones

Major Professor

We have read this dissertation
and recommend its acceptance:

Witek Nazarewicz

Mike Guidry

Larry Townsend

Accepted for the Council:

Carolyn R. Hodges

Dean of Graduate Studies

(Original signatures are on file with official student records.)

Development and Implementation of a New Technique to Study (p,α) Reactions Relevant to Nucleosynthesis in Binary Systems

A Dissertation

Presented for the

Doctor of Philosophy

Degree

The University of Tennessee, Knoxville

Brian Hossain Moazen

December 2009

Dedication

This is for God, Mom, Dad, Granny and Papaw, my brother Christopher, and the rest of my family, as well as for my wonderful wife Marisa and her family. They, and a great cast of friends, have been my supporters and cheering section and I have leaned on every one of them.

Acknowledgments

"What a long, strange trip it's been" - The Grateful Dead

So I'm an aimless and confused 20 year old delivering pizzas and attending (somewhat) a community college in Chattanooga when I run into my old high school algebra teacher, Dr. Akhdary, on campus. He looks at me like he's seen a ghost and wants to know what the world I'm doing there, as he had expected me to be doing a lot more than this. I didn't really have an answer. It was right there that I decided I should maybe start trying a little harder.

I took classes a little more seriously and then ended up enrolling at Tennessee Technological University, literally because I was just driving around, saw a sign, and thought I would drive up to Cookeville to check it out (advertising works!). It was there that I met Ray Kozub, who would become my first mentor and give me my first big break by hiring me as a research assistant at ORNL.

Now I'm here. I'm not exactly sure how it happened, but I know that I'm not here without the help of a lot of people out there. It's been my privilege to spend the last several years with some of the smartest, nicest, funniest, craziest, and most interesting people I've ever known. Did I mention crazy? It's a madhouse around here and I love it.

To the teachers and mentors, many of whom I consider friends: Jeff Blackmon, a guy with an awesome beard whom I've had the privilege of learning closely from

for almost a decade (we...e...elllll), “Dollywood” Dan Bardayan, who has been great to me and whose wife makes awesome whoopee cakes, Kate Jones (a great advisor and dancer), the aforementioned Ray Kozub, Michael Smith, Mike Guidry, Witek Nazarewicz, John Shriner, and Larry Townsend - thank you for your patience and encouragement.

Special thanks also goes out to the people that run the HRIBF: Carl Gross (the Carlnivore), Mike Dinehart, Cliff LeCroy, Bryan Bryant, Jay Pruitt, Ray Juras, Alan Tatum, Martha Meigs, Darryl Dowling, Dan Stracener, Tony Mendez, Gerald Mills, Paul Mueller and Jim Beene. Without you, none of this would be possible, literally.

To the Astroboyz past and present: Jake Livesay (mwokay?), Andy Chae (the only man at the lab who can pull off wearing pink), Jeffry Thomas (J. Sweet T.) and his house rules, Ryan Fitzgerald, ”Superstar” Steve Pain (still too tall), Kelly Chipps, Catelin Matei (once won a poster contest even when he didn’t stand by it), Bill “Matches” Peters, Stephen Pittman and his loud racecar impressions, Milan Matoš put up with me for almost two weeks in Poland (pivo proshe), “The Alaskan Bear” Luke Roberts, Eric Lingerfelt and his ski pole, Ryan Kapler and his frequently sick pets, Kyle Schmitt needs to get off me, Patrick O’Malley (shout out to Soddy-Daisy!) - thanks for the laughs, encouragement, fellowship and frequent long lunches at Buffalo Grill and Super China Buffet. If we weren’t all crazy we would all go insane. As is tradition, I now officially put the following people on the clock: Stephen Pittman, Patrick O’Malley, Kyle Schmitt, “E & M” Enrique Merino, Brett (Favre-Peyton) Manning and Irena Spassova.

I learned so much from all of you and you helped make the last several years memorable. To anyone I left out, you know who you are and the next one is on me.

Abstract

The accurate determination of the strengths and energies of resonances in (p,alpha) reactions is important for understanding the influence of reaction cycles to element synthesis in many astrophysical environments. Thus far, (p,alpha) studies in inverse kinematics have employed solid polypropylene targets. These are not always advantageous, especially when the energy loss of the incoming beam in the solid target is significantly larger than the resonance width. At the Holifield Radioactive Ion Beam Facility, a new technique has been developed for measuring the strengths and energies of (p,alpha) reactions. In this technique, a large differentially-pumped scattering chamber is filled with hydrogen gas at pressures up to 4 Torr. No windows or foils obstruct the incoming beam and reaction products are detected in coincidence by two silicon strip arrays. The vertex of the (p,alpha) reaction is determined from the known kinematics of the alpha particle and heavy recoil.

This new technique was applied to study the strength of the 183 keV resonance in ^{17}O(p,alpha)^{14}N reaction that was previously reported to significantly increase the reaction rate at nova temperatures and decrease ^{18}F production by as much as a factor of 10 in low-mass ONeMg novae. This larger strength was confirmed using the new technique and nova simulations showed a substantial decrease in ^{18}F production in lower-mass novae though a much smaller effect was seen in higher-mass novae.

Low-energy resonances in ^{31}P(p,alpha)^{28}Si and ^{35}Cl(p,alpha)^{32}S were also studied using the same technique in order to gain a better understanding of reaction cycling in the Si-Ar region. Resonance strengths at E_{CM} = 599 and 622 keV in ^{31}P(p,alpha)^{28}Si were measured as well as the E_{CM} = 611 keV resonance in ^{35}Cl(p,alpha)^{32}S, the lowest energy that any resonance in this reaction has been observed. The strengths of these resonances were found to be lower than previously determined through indirect methods, resulting in weak cycling in the Si-Ar region.

Contents

List of Tables

List of Figures

Chapter 1

Introduction

1.1 Nuclear Astrophysics

Nuclear astrophysics is the study of nuclear structure and reactions with an aim of understanding the synthesis of elements in the universe as well as stellar structure and evolution. It was suggested by Eddington in 1920 that gravitational forces were the source of energy production in stars, a theory known as the *contraction hypothesis* [Edd20]. In this hypothesis, energy would be released by the complete annihilation of matter, where the energy released is given by $E=mc^2$. However, using this gave the prediction that the age of the sun was around 20 million years, which was in disagreement with the evidence at that time which suggested an age of around one billion years [Bol07]. Around 1929, another explanation was offered by Atkinson and Houterman where, due to the high temperatures in the interior of stars, nuclei could overcome their mutual repulsion due to the Coulomb barrier and fuse together to release energy through nuclear reactions [Bet67]. In the early 1930's particle accelerators were being built in order to observe some of these nuclear reactions. In 1957, a theory of nucleosynthesis was presented which showed that all elements heavier than

helium could be synthesized in the interior of stars [Bur57]. Our present understanding is that the lighter elements up to lithium were produced shortly after the *big bang*, while heavier elements were synthesized by nuclear reactions in stellar interiors and stellar explosions such as novae, supernovae and x-ray bursts.

1.2 Stellar Explosions in Binary Systems

1.2.1 Binary Systems

Most stars found in our galaxy are in binary systems [Rol88]. These stars revolve around the common center of gravity of the binary system, and the system has a gravitational equipotential surface defined by a *Roche lobe*. There are three different classifications of binary star systems (Figure 1.1). A *detached binary* is where both stars are well within their respective Roche lobe. In a *semidetached binary*, one of the stars has filled its Roche lobe while in the case of a *contact binary* or WUMa stars, both stars have filled their respective Roche lobe and a "neck" can develop between the stars [Gui].

As long as each star is confined within its respective Roche lobe, the system is stable. However, if one of the stars becomes significantly larger during its evolution, it can fill its Roche lobe to become a semidetached binary and begin to accrete matter (mostly H and He) onto the surface of the companion star. This accretion can lead to several different types of astrophysical phenomenona such as novae, Type Ia supernovae, and X-ray bursts.

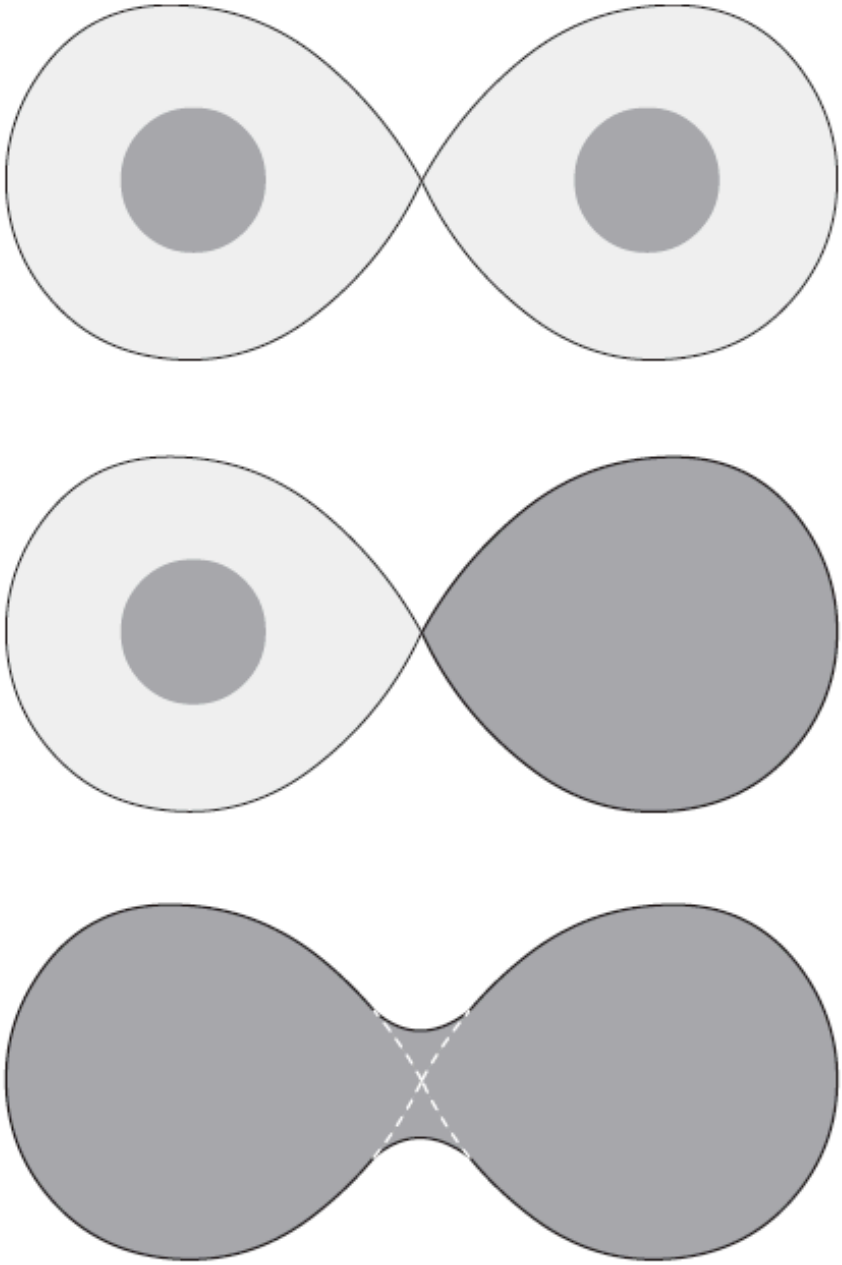

Figure 1.1: Classifications of binary systems. The darker regions define the boundaries of each star in the system. The top figure shows a detached binary, the middle figure shows a semidetached binary, and the bottom figure shows a contact binary. Figure taken from Ref. [Gui].

1.2.2 Novae

Accretion from a companion star (typically a red giant) onto a white dwarf can lead to a stellar explosion known as a nova (Figure 1.2). White dwarfs are remnants of stars that have exhausted all of their available nuclear fuel for burning and consist primarily of degenerate oxygen and carbon, though some dwarfs consisting of oxygen, neon, and magnesium (ONeMg) are known to exist [Chi09]. Accreted gas from the companion star approaches the white dwarf at an extremely high velocity and releases energy upon impact with the surface, thus raising the temperature [Rol88]. At lower temperatures, the gas of electrons on the surface of the white dwarf is degenerate, so the layer of accreted gas gathering on the surface does not affect the pressure while still raising the temperature.

When the temperature is sufficiently raised (T $\approx$ 20 x 10^6 K), the rate of nuclear reactions increase exponentially on the surface of the white dwarf, proceeding primarily through the CNO and hot-CNO cycles as well as the rapid proton capture process (*rp* process) (section 1.3), using the accreted hydrogen as fuel. Eventually the increasing temperature will lift the degeneracy of the gas and the pressure will increase with temperature, typically reaching up to T $\approx$ 0.4 GK. The resulting thermonuclear reactions (called a *thermonuclear runaway*) will blow the outer layer of the white dwarf away and the sequences of nuclear reactions during the explosion can produce heavy elements up to nickel (Table 1.1).

The duration of a typical novae explosion is 100-1000 seconds with the explosion ejecting $\approx 10^{-4}$ of the total mass of the white dwarf, leaving open the possibilty for the nova to reoccur, which has been observed [Gui]. The positron annihilation resulting from the β-decay of ^{18}F is the largest source of γ-rays in a nova explosion. Due to the relatively long half-life of ^{18}F ($\tau \approx 2$ hr), the ^{18}F isotope can survive the

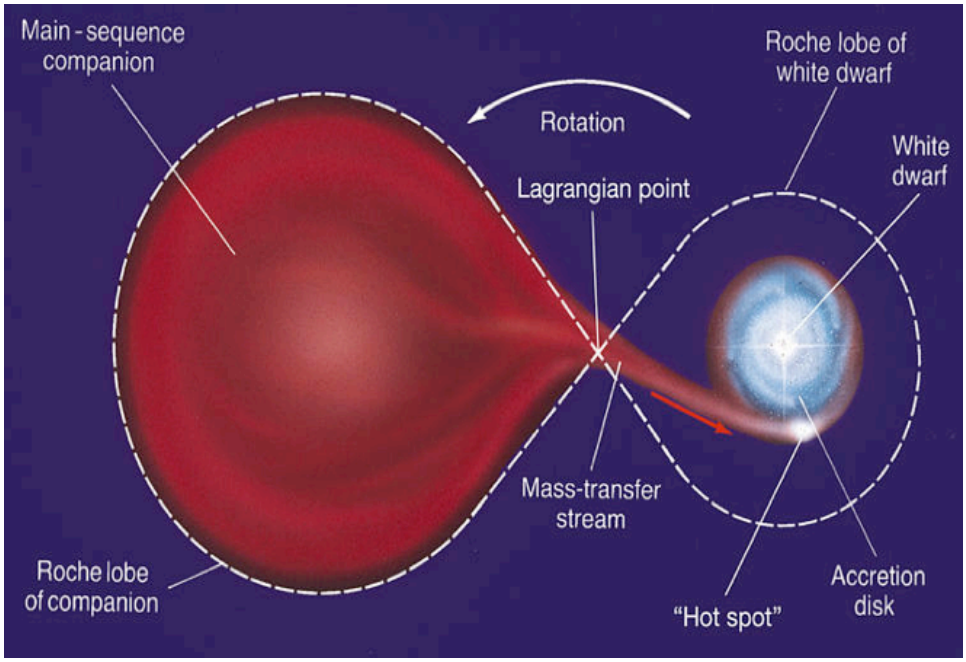

Figure 1.2: Schematic of the accretion of hydrogen and helium from a main-sequence star onto the surface of a white dwarf. Figure taken from Ref. [Pea05].

Table 1.1: Inferred elemental abundances relative to hydrogen from the Nova Cygni 1992 explosion. Values taken from [Gui].

Chemical Element	Abundance
He	4.5
C	70.6
N	50.0
O	80.0
Ne	250.0
Na	37.4
Mg	129.4
Al	127.5
Si	146.6
S	1.0
Ar	5.0
Ca	46.8
Fe	8.0
Ni	36.0

initial explosion [Coc00]. Observing the γ-rays from the β-decay of ^{18}F after the explosion could be extremely useful in constraining nova models. Therefore, nuclear reactions leading to the production and destruction of the ^{18}F isotope are critical for understanding final isotopic abundances in novae.

1.2.3 Type Ia Supernovae

If the accreted hydrogen and helium onto the white dwarf from the companion star proceeds without thermonuclear runaway occuring due to a sufficiently fast accretion rate, the mass of the star could reach that of the Chandrasekhar limit given by [Rol88]:

$$M_c \approx \frac{\pi\sqrt{6}}{32}(1+X)^2\frac{1}{m_H^2}\left(\frac{hc}{2\pi G}\right)^{3/2} \approx 1.4M_\odot \tag{1.1}$$

where X is the mass fraction for hydrogen for the white dwarf, $m_H = 1$ amu is the mass of hydrogen, h is Planck's constant, c is the speed of light in vacuum, G is

the gravitational constant, and $M_{\odot}$ is the mass of the white dwarf in units of solar masses. A white dwarf that approaches this mass is no longer supported by the electron degeneracy pressure in the star and becomes gravitationally instable against collapse. This instability can ignite the carbon and oxygen in the core of the star and a type Ia supernova can occur, in which the entire star is consumed in a thermonuclear flash. Most of the star burns to ^{56}Ni, which then β-decays to ^{56}Co and ^{56}Fe. Type Ia supernovae explosions have been suggested to be significant contributors to the total abundance of elements from silicon to the iron group elements in the Galaxy [Rol88].

1.2.4 X-ray Bursts

The mechanism for an X-ray burst is similar to that of novae, except that accreted matter from the companion star collects onto a neutron star instead of a white dwarf. Since a neutron star is much denser than a white dwarf, its gravitational field is much stronger, thus accreted matter falls onto the neutron star at a high velocity, resulting in the emission of radiation in the X-ray region. Due to the higher velocities of the accreted matter, the thermonuclear runaway on the surface of the neutron star proceeds at a much higher temperature (T $\geq$ 1 GK) than that of novae, and X-ray bursts are thought to be powered primarily through the hot-CNO cycle and *rp* process [Sch98]. The time scale for X-ray bursts are typically a few seconds and can take as little as a few hours to re-occur [Gui].

1.3 Reactions and Nucleosynthesis in Binary Systems

1.3.1 The CNO I-III and Hot-CNO Reaction Cycles

The main sequence of nuclear reactions occuring in stellar explosions in binary systems is known as the carbon-nitrogen-oxygen (CNO) cycle. The sequence of reactions in the main CNO cycle (also called "cold" CNO cycle) is (labeled as I in Figure 1.3):

$$\begin{aligned} {}^{12}C + p &\rightarrow {}^{13}N + \gamma \\ {}^{13}N &\rightarrow {}^{13}C + e^{+} + \nu_e \\ {}^{13}C + p &\rightarrow {}^{14}N + \gamma \\ {}^{14}N + p &\rightarrow {}^{15}O + \gamma \\ {}^{15}O &\rightarrow {}^{15}N + e^{+} + \nu_e \\ {}^{15}N + p &\rightarrow {}^{12}C + {}^{4}He \end{aligned} \tag{1.2}$$

The above set of reactions is also sometimes called the CN cycle since only the carbon and nitrogen reacts with hydrogen. Since no carbon, oxygen, or nitrogen is actually consumed in the sequence, they serve only as a catalysts, or spectators, and the cycle can be initiated by any of the above reactions. The net effect of the CNO cycle is the conversion of 4 protons into helium 4:

$${}^{12}C + 4p \rightarrow {}^{12}C + {}^{4}He + 2\beta^{+} + 2\nu \tag{1.3}$$

liberating 26.8 MeV of energy each time the cycle is performed. The limiting reaction in the CNO cycle is ^{14}N(p,γ)^{15}O which proceeds at the slowest rate compared to the

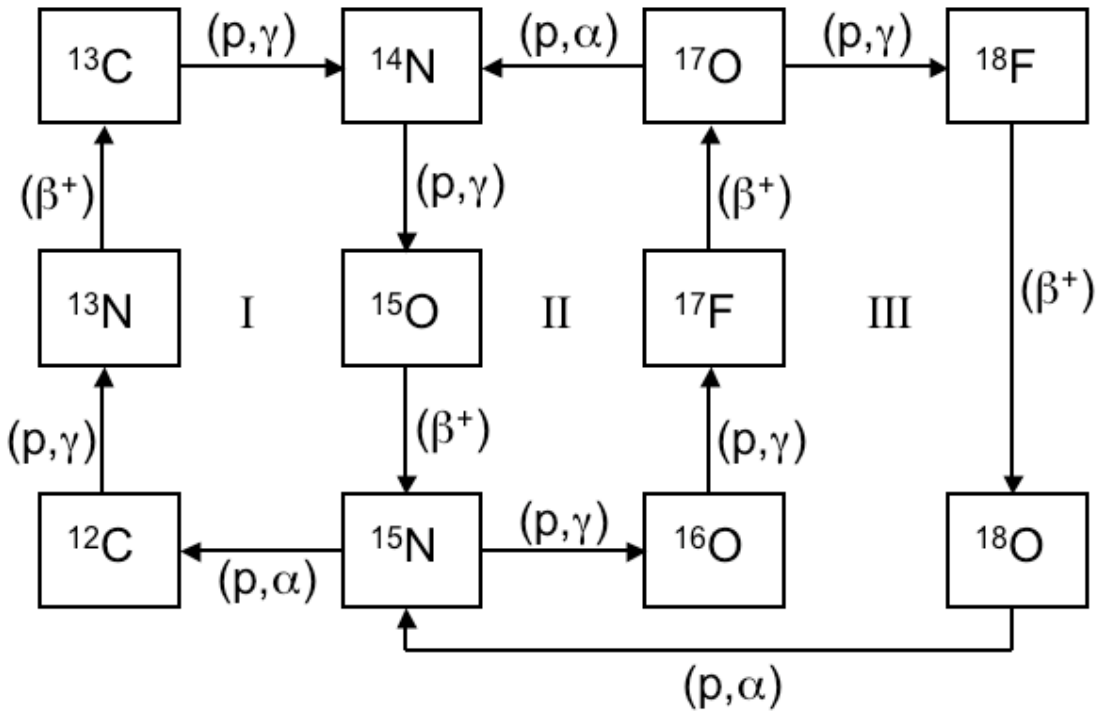

Figure 1.3: The sequence of reactions in the CNO I-III cycles

Table 1.2: Reaction rates (in reactions/second) for the reactions of the CNO cycle at a temperature of T = 10 MK, density = 100 g/cm^{-3}, and $X_H = 0.5$ (fraction of total hydrogen mass to the total mass). Value taken from [Rol88].

Reaction	Reactions/second (x 10^{16})
^{12}C(p,γ)^{13}N	0.05
^{13}C(p,γ)^{14}N	0.3
^{14}N(p.γ)^{15}O	0.0002
^{15}N(p.α)^{12}C	3.2

other reactions in the cycle. Table 1.2 shows the reaction rates for the ^{12}C(p,γ)^{13}N, ^{13}C(p,γ)^{14}N, ^{14}N(p,γ)^{15}O, ^{15}N(p,α)^{12}C reactions. It can easily be seen from the table that since the ^{14}N(p,γ)^{15}O reaction is slower by approximately two orders of magnitude than the next slowest reaction, it acts essentially as a "bottleneck" for the CNO cycle.

The ^{15}N in the CNO cycle reacts with hydrogen through the ^{15}N(p,α)^{12}C reaction. However, the CNO cycle can branch out through the ^{15}N(p,γ)^{16}O reaction about 1 out of every 1000 cycles (for temperatures less than 10^8 K) [Cla83] and another cycle known as CNO-II can emerge (labeled as II in Figure 1.3):

$$\begin{aligned} {}^{14}N + p &\rightarrow {}^{15}O + \gamma \\ {}^{15}F &\rightarrow {}^{15}N + e^+ + \nu_e \\ {}^{15}N + p &\rightarrow {}^{16}O + \gamma \\ {}^{16}O + p &\rightarrow {}^{17}F + \gamma \\ {}^{17}F &\rightarrow {}^{17}O + e^+ + \nu_e \\ {}^{17}O + p &\rightarrow {}^{14}N + \alpha \end{aligned} \tag{1.4}$$

The ^{17}O(p,α)^{14}N reaction feeds the CNO bi-cycle back into the original CNO cycle. Still another cycle (CNO-III) is also possible at higher temperatures through the

^{17}O(p,γ)^{18}F reaction:

$$\begin{aligned} {}^{17}O + p &\rightarrow {}^{18}F + \gamma \\ {}^{18}F &\rightarrow {}^{18}O + e^{+} + \nu_e \\ {}^{18}O + p &\rightarrow {}^{15}N + \alpha \end{aligned} \tag{1.5}$$

The net effect of any of these additional cycles is still the conversion of 4 protons into ^{4}He. Breakout from the CNO cycles to higher mass isotopes can occur through the ^{18}O(p,γ)^{19}F reaction that competes with the ^{18}O(p,α)^{15}N reaction, with the ratio of the ^{18}O(p,γ)^{19}F reaction rate to that of ^{18}O(p,α)^{15}N equal to roughly 1:150 in the temperature range $0.02 \leq \mathrm{T} \leq 0.7$ GK [Rol88].

Since branching out of the main CNO cycle to the CNO II and III cycles is relatively weak, the CNO II and III cycles do not appreciably contribute to the overall energy production. However, these additional cycles are critical to nucleosynthesis since breakout from these cycles might possibly be connected with higher mass reaction cycles such as the NeNa cycle, where nuclei up to ^{23}Na can be synthesized. Overall, the isotope with the largest abundance left over after the CNO cycle is ^{14}N, due to its slow hydrogen burning rate as stated previously [Rol88].

The beta decay of ^{13}N in the CNO I cycle is a weak interaction process and thus has little dependence on temperature. However, ^{13}N can also undergo proton capture through the ^{13}N(p,γ)^{14}O reaction which is strongly temperature-dependent. At lower temperatures, the beta decay dominates, but at temperatures reached during the initial nova explosion of $\mathrm{T} \geq 0.2$ GK, the (p,γ) reaction begins to dominate over the beta decay and a new cycle known as the hot-CNO cycle characterizes the reaction

flow [Gui]. The reactions of the hot CNO cycle are given by (see Figure 1.4):

$$\begin{aligned} {}^{12}C + p &\rightarrow {}^{13}N + \gamma \\ {}^{13}N + p &\rightarrow {}^{14}O + \gamma \\ {}^{14}O &\rightarrow {}^{14}N + e^{+} + \nu_e \\ {}^{14}N + p &\rightarrow {}^{15}O + \gamma \\ {}^{15}O &\rightarrow {}^{15}N + e^{+} + \nu_e \\ {}^{15}N + p &\rightarrow {}^{12}C + \alpha \end{aligned} \tag{1.6}$$

At temperatures exceeding T = 0.4 GK (not believed to be reached in novae), the ^{14}O from the previous set of reactions can also react with ^{4}He through the ^{14}O(α,p)^{17}F reaction to form a bi-cycle (Figure 1.4) reaching up to neon. The main breakout reactions of the hot-CNO cycle are the ^{18}F(p,γ)^{18}Ne (T $\geq$ 0.5 GK) and ^{18}Ne(α,p)^{21}Na (T $\geq$ 0.8 GK) reactions. The hot-CNO cycle is believed to be the main source of energy production and nucleosynthesis in novae.

1.3.2 The *rp*-process

At the higher temperatures achieved in an X-ray burst (T $\geq$ 1 GK), the hot-CNO cycle can breakout into a series of proton captures, alpha captures, and beta decays known as the*rp*-process. This processs, thought to be the main source of energy production and nucleosynthesis in X-ray bursts, can proceed up to ^{56}Ni or even beyond [Sch98]. The *rp*-process may be responsible for the synthesis of proton-rich isotopes in X-ray bursts, though it is unclear whether or not material made in the explosion can escape the gravity of the neutron star [Gui].

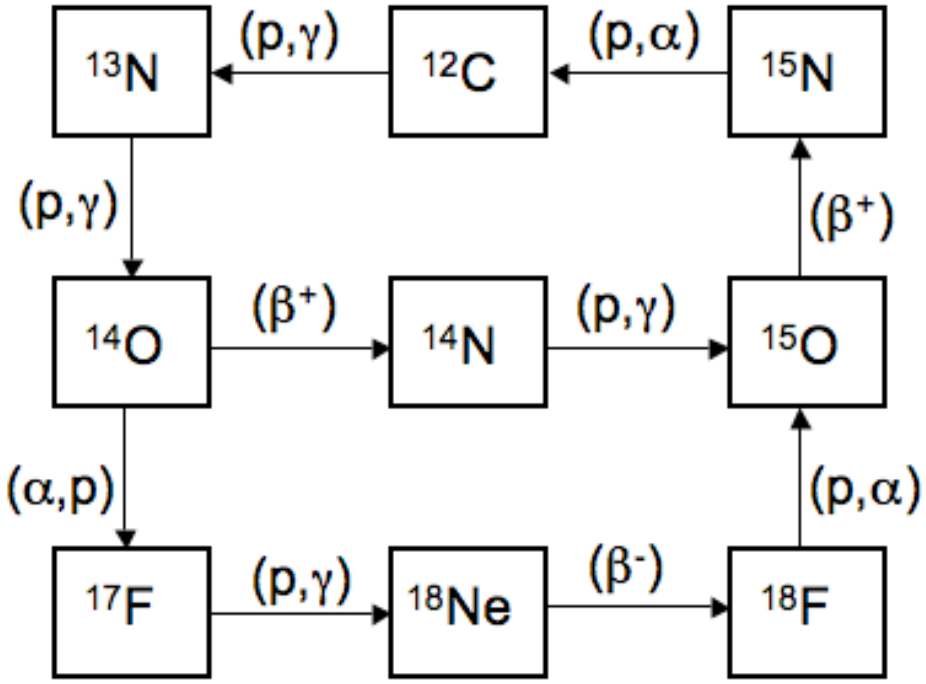

Figure 1.4: The sequence of reactions in the hot-CNO cycle.

Though the hot-CNO cycle dominates the reaction flow in novae, the *rp*-process can play a role in more energetic novae. However, due to the lower temperatures and densities in novae, the burning does not proceed beyond mass 40 (Figure 1.5). The higher mass abundances in Table 1.1 most likely come from pre-existing iron and nickel in the white dwarf.

1.4 Reaction Rate Formalism

1.4.1 Stellar Reaction Rates

The nucleosynthesis and energy production in stars as well as in stellar explosions are determined by reaction rates. The probablility that two nuclei will react is proportional to the flux of the incident particles as well as the "geometric area", expressed as a nuclear cross section. If the two interacting nuclei have number densities given by N_x and N_y, relative velocity v, cross section $\sigma(v)$, and flux J, the reaction rate is is defined to be [Cla83]:

$$r_{xy} = JN_y\sigma(v) \tag{1.7}$$

where the flux J is the particles per unit volume times their velocity and is given by:

$$J = N_x v \tag{1.8}$$

Equation 1.7 is usually written as:

$$r_{xy} = N_x N_y v\sigma(v) \tag{1.9}$$

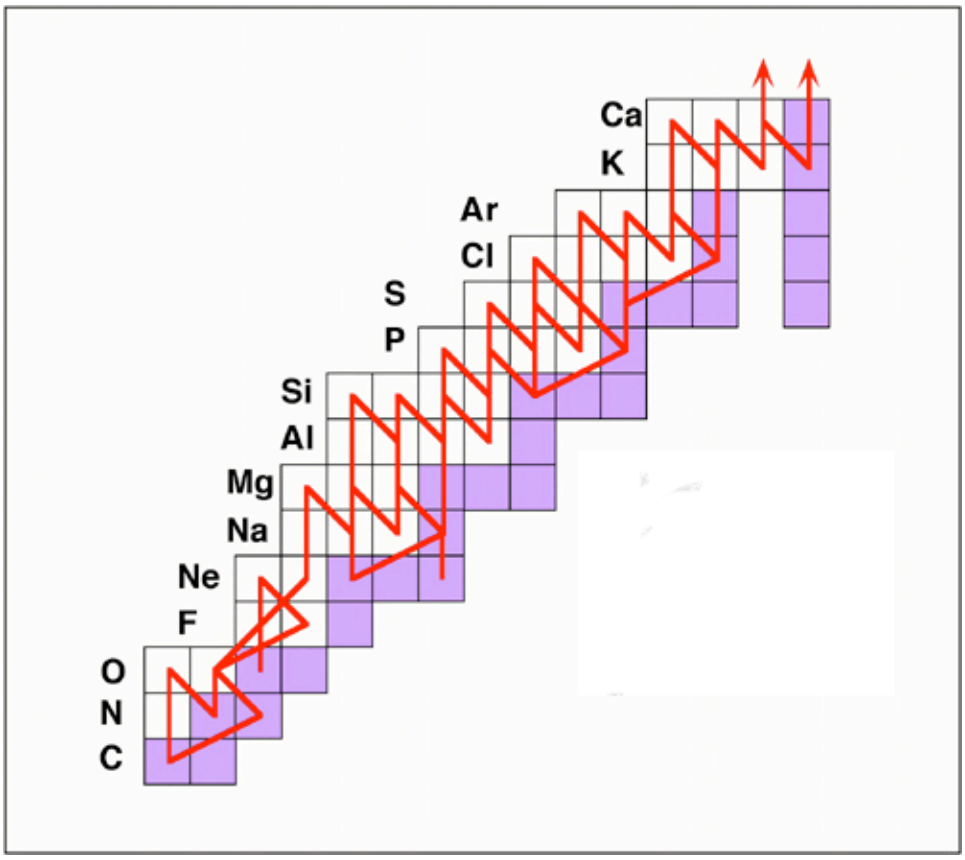

Figure 1.5: The *rp*-process in more energetic novae. Figure taken from Ref. [Cha92].

In a stellar environment, much like a gas, the velocities of particles are widely distributed, therefore the quantity $v\sigma(v)$ must be thermally-averaged over all values of v such that:

$$< \sigma v >= \int_0^\infty \phi(v) v\sigma(v) dv \tag{1.10}$$

where $\phi(v)$ is a velocity distribution and gives the probablility that a particle will have a velocity between v and v + dv. Replacing the quantity $v\sigma(v)$ in equation 1.9 with the thermally-averaged $< \sigma v >$ gives:

$$< \sigma v >= \frac{r_{xy}}{N_x N_y} \tag{1.11}$$

where $< \sigma v >$ is known as the *reaction rate per particle pair*.

Since the gas in stellar environments is normally non-degenerate and the nuclei do not reach relativistic speeds [Rol88], the Maxwell-Boltzmann velocity distribution is applicable:

$$\phi(v) = 4\pi v^2 \left(\frac{\mu}{2\pi kT}\right)^{3/2} exp\left(-\frac{\mu v^2}{2kT}\right) \tag{1.12}$$

where μ is the reduced mass of the interacting nuclei ($= m_x m_y/(m_x + m_y)$), k is the Boltzmann constant, and T is the temperature. This gives for the reaction rate per particle pair:

$$< \sigma v >= 4\pi v^2 \left(\frac{\mu}{2\pi kT}\right)^{3/2} \int_0^\infty v^3 \sigma(v) exp\left(-\frac{\mu v^2}{2kT}\right) dv \tag{1.13}$$

Rewritting this in terms of the center-of-mass energy $E_{CM} = 1/2^* \mu v^2$ gives:

$$< \sigma v >= \left(\frac{8}{\mu\pi}\right)^{1/2} \left(\frac{1}{kT}\right)^{3/2} \int_0^\infty E\sigma(E) exp\left(-\frac{E}{kT}\right) dE \tag{1.14}$$

Therefore, what is needed experimentally in order to determine stellar reactions rates at given temperatures are the nuclear cross sections for the reactions over a wide range of energies.

1.4.2 Nonresonant reaction rates and the Gamow window

Nuclear reactions of charged particles in stellar environments are hampered by the repulsion between positively-charged nuclei due to the Coulomb potential. The potential energy between two charged particles can be written as:

$$V_C(r) = \frac{Z_1 Z_2 e^2}{r} \tag{1.15}$$

where Z_1 and Z_2 are the numbers of protons of the respective nuclei, e is the fundamental charge constant, and r is the distance between the nuclei. Typically, kT $\ll$ E_C, so clasically, the vast majority of particles are not able to overcome this barrier in order to reach the attractive nuclear potential at small distances. However, from quantum mechanics, there is a small but finite probablility for particles with energy E $<$ $E_{coulomb}$ to penetrate the Coumlomb barrier, given by:

$$P = exp(-2\pi\eta) \tag{1.16}$$

where η is the Sommerfield parameter and is equal to:

$$\eta = \frac{Z_1 Z_2 e^2}{\hbar v} \tag{1.17}$$

The exponential in equation 1.16 can be rewritten as:

$$2\pi\eta = 31.29 Z_1 Z_2 \left(\frac{\mu}{E}\right)^{1/2} \tag{1.18}$$

where the center-of-mass energy E is given in keV and μ in amu. This expression for the probability of tunneling is commonly referred to as the Gamow factor [Rol88].

The cross section $\sigma(E)$ is proportional to the probability for tunneling:

$$\sigma(E) \propto exp(-2\pi\eta) \tag{1.19}$$

as well as the de Broglie wavelength:

$$\sigma(E) \propto \pi \left(\frac{\lambda}{2\pi}\right)^2 \tag{1.20}$$

Neither of these terms have any dependence upon nuclear effects. However, it would be expected that the cross section would exhibit some sort of dependency on nuclear effects. To account for this, an extra factor *S(E)*, known as the nuclear or astrophysical S-factor, is inserted into the cross section so that overall the cross section is given by:

$$\sigma(E) = \left(\frac{1}{E}\right) exp(-2\pi\eta) S(E) \tag{1.21}$$

Any part of the probability for a reaction that arises from nuclear effects is absorbed into the S-factor $S(E)$. One significant advantage of the S-factor is that in regions where there are no resonances, it is typically a smoothly-varying function of energy (compared to the energy dependence of the cross section), so that it is much easier to extrapolate to lower energies [Cla83].

Equation 1.21 can be inserted into equation 1.14 to give for the reaction rate per particle pair:

$$< \sigma v >= \left(\frac{8}{\mu\pi}\right)^{1/2} \left(\frac{1}{kT}\right)^{3/2} \int_0^\infty S(E) exp\left(-\frac{E}{kT} - \frac{b}{E^{1/2}}\right) dE \tag{1.22}$$

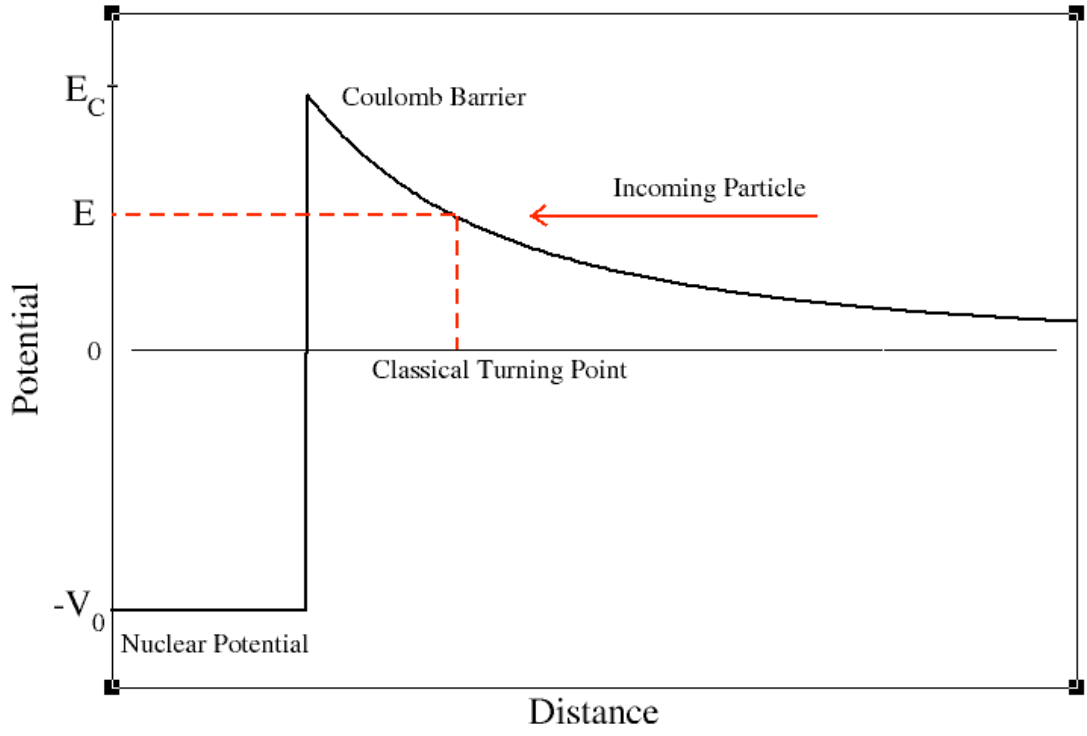

Figure 1.6: Schematic of the combined nuclear and coulomb potentials. Figure not drawn to scale.

where

$$b = (2\mu)^{1/2}\pi e^2 Z_x Z_y/\hbar = 0.989 Z_x Z_y \mu^{1/2}(MeV)^{1/2} \tag{1.23}$$

The quantity b^2 is known as the *Gamow energy*, E_G [Rol88]. Most of the energy dependence in the integrand of equation 1.22 lies in the two exponential factors: the Coulomb penetration factor, $exp[-b/E^{-1/2}]$, which is very small at low energies but increases rapidly, and the Maxwell-Boltzmann term, *exp[-E/kT]*, which peaks at kT and decreases rapidly with increasing energy. The combination of the two factors causes a sharp peak in the integrand known as the *Gamow peak* (see Figure 1.7). The range of energies inside the Gamow window is where, for a given temperature, nuclear reactions are much more to likely take place. Since over this small window in energy the S-factor will not change dramatically, $S(E)$ can be approximated by its value at the peak of the curve, E_0, and equation 1.22 can be approximated as:

$$< \sigma v >= \left(\frac{8}{\mu\pi}\right)^{1/2} \left(\frac{1}{kT}\right)^{3/2} S(E_0) \int_0^\infty \exp\left(-\frac{E}{kT} - \frac{b}{E^{1/2}}\right) dE \tag{1.24}$$

The peak of the Gamow window, E_0, can be found by taking the first derivative of the integrand in equation 1.24, giving:

$$E_0 = \left(\frac{bkT}{2}\right)^{2/3} = 1.22(Z_X^2 Z_Y^2 \mu T_6^2)^{1/3} keV \tag{1.25}$$

and the width in energy can be found by approximating the Gamow window by a Gaussian function:

$$\exp\left(-\frac{E}{kT} - \frac{b}{E^{1/2}}\right) = I_{max} \exp\left[-\left(\frac{E - E_0}{\Delta/2}\right)^2\right] \tag{1.26}$$

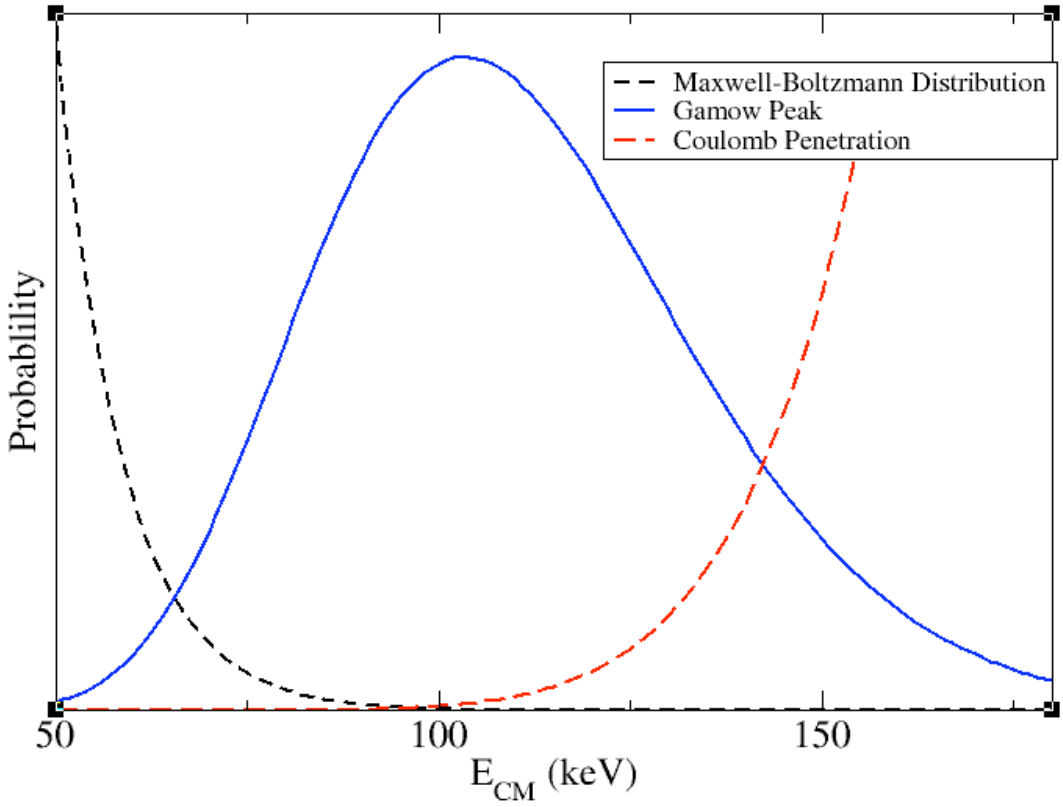

Figure 1.7: The Gamow window for the ^{17}O + p system for a stellar temperature of $T_9 = 0.1$. The values of each curve have been multiplied by different factors for purposes of comparison.

where the width in energy, Δ is:

$$\Delta = \frac{4}{3^{1/2}}(E_0 kT)^{1/2} = 0.749(Z_X Z_Y \mu T_6^5)^{1/6} keV \tag{1.27}$$

and

$$I_{max} = \exp\left(-\frac{3E_0}{kT}\right) \tag{1.28}$$

The majority of nuclear burning takes place at energies between E_0 and $E_0 \pm \Delta/2$. One of the major hurdles in experimental nuclear astrophysics is that E_0 is typically in a region where cross sections are extremely small, thus large beam intensities and long running times for experiments are required. Therefore, making direct measurements of $\sigma(E)$ (and hence $S(E)$) near E_0 can be extremely difficult [Rol88]. Typically, measurements of $S(E)$ are performed at higher energies and the value of $S(E_0)$ is extrapolated.

Overall, inserting equation 1.26 into equation 1.24 and integrating the Gaussian approximation for the Gamow window gives for the nonresonant reaction rate [Rol88]:

$$< \sigma v >= \left(\frac{2}{\mu}\right)^{1/2} \frac{\Delta}{(kT)^{3/2}} S(E_0) \exp\left(-\frac{3E_0}{kT}\right) \tag{1.29}$$

1.4.3 Resonant Reaction Rates for Narrow Resonances

In regions where no resonances are present, the non-resonant reaction rate in equation 1.29 dominates the overall reaction rate. However, in many energy regions the reaction rate can be dominated by resonances, where the initial nuclei X and Y fuse together to form a compound nucleus in an excited state which can then decay through particle emmision or γ-decay to a lower-lying state. In these cases, the cross section

is enhanced and the S-factor is no longer a smoothly varying function compared to regions without a resonance.

An excited state of a nucleus is characterized by a mean lifetime τ_0, which is related to a width in energy by the uncertainty principle ($\Gamma\tau_0 = \mathrm{h}/2\pi$) [Rol88]. The total width of an excited state is related to the partial widths of all allowed decay channels by:

$$\Gamma = \Sigma_i \Gamma_i \tag{1.30}$$

where each Γ_i is the partial width for a decay channel. The Breit-Wigner formula for a nuclear cross section is given by:

$$\sigma_{BW}(E) = \pi \left(\frac{\lambda}{2\pi}\right)^2 \frac{2J+1}{(2J_X+1)(2J_Y+1)}(1+\delta_{XY})\frac{\Gamma_a\Gamma_b}{(E-E_R)^2+(\Gamma/2)^2} \tag{1.31}$$

where J, J_X, and J_Y are the spins of the excited state in the compound nucleus and the interacting particles X and Y, respectively, $\lambda = h/(2\mu E)$ is the de Broglie wavelength, and Γ_a, Γ_b, and Γ are the partial widths of the exit channels a and b and the total width respectively. The delta function δ_{XY} is present since the cross section is doubled for identical interacting particles. Using equations 1.14 and 1.31, the reaction rate per particle pair can be written as:

$$< \sigma v >= \left(\frac{8}{\pi\mu}\right)^{1/2} \left(\frac{1}{kT}\right)^{3/2} \int_0^\infty \sigma_{BW}(E) E \exp\left(-\frac{E}{kT}\right) dE \tag{1.32}$$

In the case of a narrow resonance, the Maxwell-Boltzmann distibution factor $Eexp[-E/KT]$ remains fairly constant over the energy region of the resonance, therefore it can be approximated by its value at the resonance energy:

$$< \sigma v >= \left(\frac{8}{\pi\mu}\right)^{1/2} \left(\frac{1}{kT}\right)^{3/2} E_R \exp\left(-\frac{E_R}{kT}\right) \int_0^\infty \sigma_{BW}(E)\, dE \tag{1.33}$$

If the resonance is narrow ($\Gamma \ll \mathrm{E}_R$), the integral in equation 1.33 reduces to:

$$\int_0^\infty \sigma_{BW}(E)dE = 2\pi^2 \left(\frac{\lambda_R}{2\pi}\right)^2 \omega\gamma \tag{1.34}$$

where

$$\omega = \frac{2J+1}{(2J_X+1)(2J_Y+1)} \tag{1.35}$$

$$\gamma = \frac{\Gamma_a \Gamma_b}{\Gamma} \tag{1.36}$$

and the quantity $\omega\gamma$ is referred to as the *strength* of a resonance. Using equations 1.33 and 1.34 gives for the resonant reaction rate:

$$< \sigma v >= \left(\frac{2\pi}{\mu kT}\right)^{3/2} \left(\frac{h}{2\pi}\right)^2 (\omega\gamma) \exp\left(-\frac{E_R}{kT}\right) \tag{1.37}$$

If there are several isolated, narrow resonances present, the total resonant reaction rate is found by summing the contributions of each resonance:

$$< \sigma v >= \left(\frac{2\pi}{\mu kT}\right)^{3/2} \left(\frac{h}{2\pi}\right)^2 \Sigma_i(\omega\gamma)_i \left(-\frac{E_i}{kT}\right) \tag{1.38}$$

Often it is useful to express the resonant reaction rate in units of reactions per particle density per second:

$$N_A < \sigma v >= 1.54x10^{11} \mu^{-3/2} (\omega\gamma) T_9^{-3/2} \exp\left(-\frac{11.61 E_R}{T_9}\right) \tag{1.39}$$

where $\mathrm{N}_A < \sigma v >$ has units of $\mathrm{cm^3 mol^{-1} s^{-1}}$, μ is in units of amu, $\omega\gamma$ and E_R in MeV, and $\mathrm{T_9}$ is the temperature in GK.

Chapter 2

New Experimental Technique to Study (p,α) Reactions

2.1 Motivation

To study a particular nuclear reaction in regular kinematics, an ion beam consisting of light particles bombards a heavy solid or gas target. Using this technique in a ^{17}O(p,α)^{14}N study for example, a proton beam would impinge upon a target consisting of ^{17}O gas. However, this reaction could also be studied using a solid target enriched with hydrogen or by using a target of hydrogen gas. In this case, the incoming beam would be ^{17}O and the reaction would be performed in *inverse kinematics*, where the mass of the incoming beam is much larger than the target. Using inverse kinematics can be advantageous over regular kinematics when it is difficult to make a target of the heavy ion, as is the case in ^{17}O or ^{35}Cl where a solid target can only be made as part of a compound. Inverse kinematics also works well for reaction studies using radioactive beams since the use of radioactive targets can be extremely limited due to decay of the target.

Previous (p,α) studies in inverse kinematics have been performed by using solid foil targets. This can become problematic at lower resonance energies where the widths of resonances can be comparable to the energy loss of the beam through even the thinnest of targets. Furthermore, due to the presence of inactive contaminants in solid targets (carbon in the CH_2 target in the previous $^{17}O(p,\alpha)^{14}N$ study for example [Cha05]), the yield from the (p,α) reaction is not maximized. The target stoichiometry can change throughout an experiment due to degradation of the target foil as well. One way to minimize these effects would be to use pure hydrogen gas as the target instead of foils.

2.2 Experimental Setup

At the Holifield Radioactive Ion Beam (HRIBF) at Oak Ridge National Laboratory (ORNL) a new technique was developed to measure the strengths and energies of narrow resonances of (p,α) reactions. A schematic of the experimental setup is shown in Figure 2.1. In this technique, the incident ion beam enters a large scattering chamber (43 cm x 43 cm) filled with ultra high purity hydrogen gas (>99.9999% H_2) at pressures of up to 4 Torr. The chamber is differentially pumped (section 2.3), so no windows or foils contain the gas or obstruct the beam.

The α particles and heavy recoils from the (p,α) reaction are detected in coincidence by an array of silicon strip detectors within the hydrogen gas [Moa07]. The placement of the SIDAR silicon detector array (section 2.4) is located approximately 115 mm from the entrance of the chamber in order to detect alpha particles from the (p,α) reaction. This position for the SIDAR array was found to give a resonable amount of target thickness while still allowing for the thickness to be adjusted. Heavy recoils from the (p,α) reaction pass through the center of the SIDAR array and are

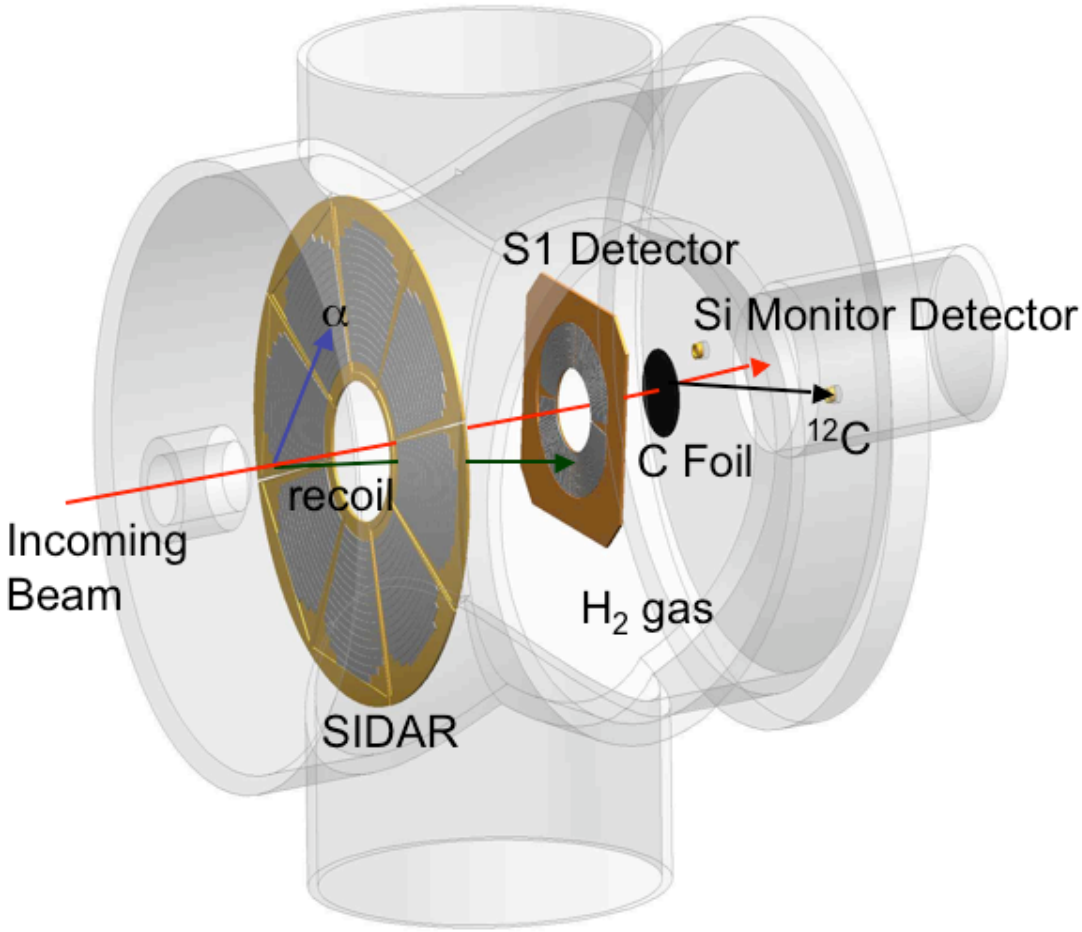

Figure 2.1: Schematic of the experimental setup. The differential pumping stages are not shown.

detected by an annular type S1 silicon strip detector (also known as CD or MINI detector) (section 2.4). The distance between the S1 detector and the SIDAR array is dependent on the kinematics of the particular (p,α) reaction being studied.

Unreacted beam passes through the centers of both detectors and impinges on a carbon foil placed 10 cm downstream from the S1 detector. Scattered carbon atoms are detected in two silicon monitor detectors mounted 27 cm from the foil at $\theta_{lab} \approx 33^o$. Yields from the ^{12}C(x,^{12}C)x (where x is the scattered beam) elastic scattering reaction are used together with the Rutherford cross section for scattering to determine the integrated beam current to use in normalization.

There are several advantages to this technique over the use of foils. The most significant advantage is that the pure nature of the target maximizes the yield from the (p,α) reaction. The pressure of the hydrogen gas inside the target chamber can also be adjusted in order to match the areal target density to the expected resonance width, thus minimizing yield from off-resonance reactions and reducing background. This approach is also well-suited for use with radioactive ion beams (section 5.2).

2.3 Differential Pumping System

The differential pumping system used in the (p,α) studies is essentiallly the same system used for the windowless gas target (WGT) developed at the HRIBF for use in (p,γ) studies [Fit05]. Upstream of the target chamber, there are two cubes, each bisected into two separate pumping stages and coupled to each other through 5 cm long (5 mm diameter) brass apertures to restrict the flow of gas upstream. To furthur contain the gas within the target chamber, a plate with a 5 mm diameter hole is attached at the entrance of the chamber.

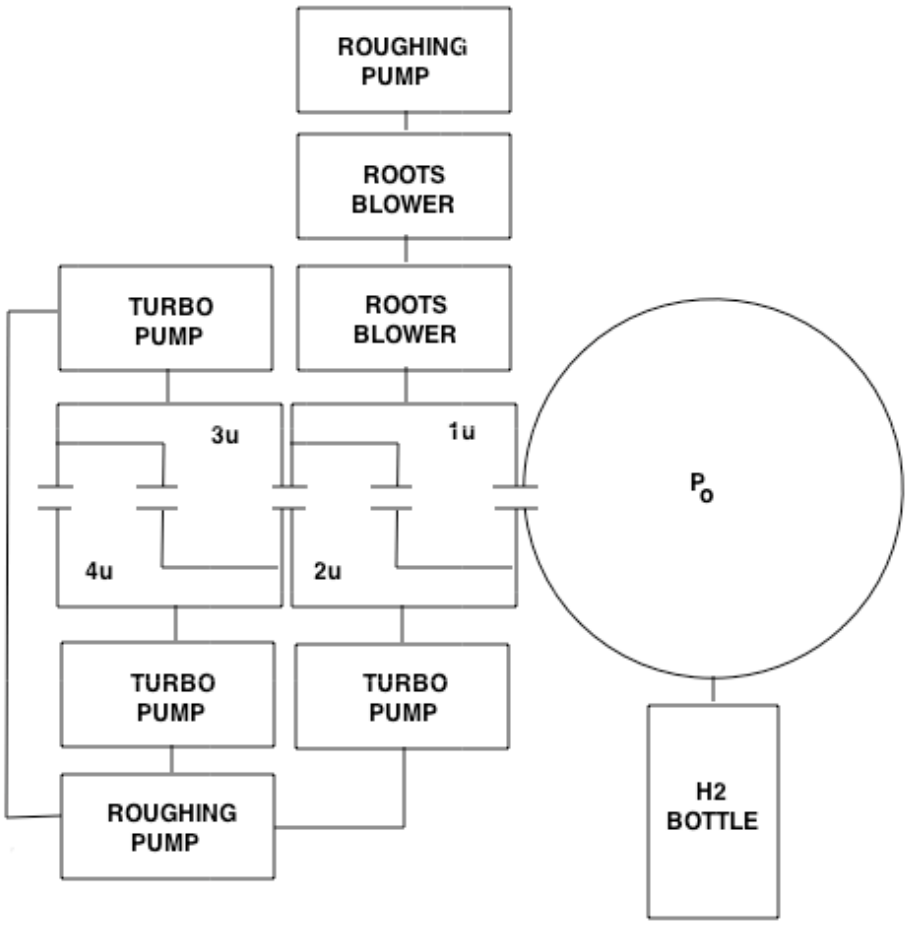

Figure 2.2: Schematic of the differential pumping system

The first stage located upstream of the target (labeled *1u* in Figure 2.2) is pumped by two large WSU 501 roots blowers and backed by a roughing pump. The next three upstream stages (*2u*, *3u*, and *4u*) each have a separate turbo pump backed by a common roughing pump. Unlike the WGT, there is no pumping downstream of the target.

Each individual pumping stage decreases the pressure by a few orders of magnitude. Using this setup, gas pressures as high as 5-6 Torr can be present inside the target chamber with a pressure of $\approx 10^{-6}$ Torr at the entrance aperture upstream of the target. Though higher pressures within the chamber would increase the yield of the (p,α) reaction and better localize the reaction vertex, the maximum achievable pressure inside the chamber is limited by the load on the upstream pumps, which must reduce the pressure to $< 10^{-6}$ Torr in order to connect to the beamline.

The pressure inside the chamber is monitored using a MKS 10 Torr full-scale Absolute Capacitance Baratron rated to 1 millitorr, which is mounted on the target chamber. For an additional measurement of the central pressure, a thermocouple was placed on the chamber. The pressure inside the chamber can be regulated to better than ± 5 millitorr. Thermocouples were also located at each differential pumping stage to ensure that the pressure adequetly decreases in each stage.

2.4 Detectors and Electronics

In order to identify the (p,α) reaction, as well as calculate the reaction vertex and normalize data to the number of incident beam particles, the reaction products must be detected with good efficiency and energy resolution. In our (p,α) studies, we employed several detectors in order to achive this.

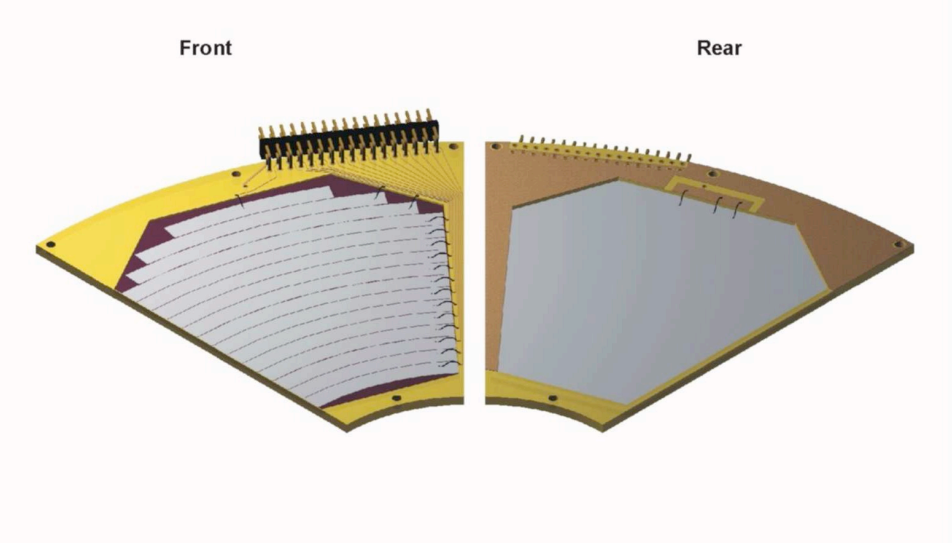

Figure 2.3: MSL-type YY1 wedge. Figure taken from Ref. [Mic05]

Figure 2.4: MSL Design S1 annular detector. Figure taken from Ref. [Mic05]

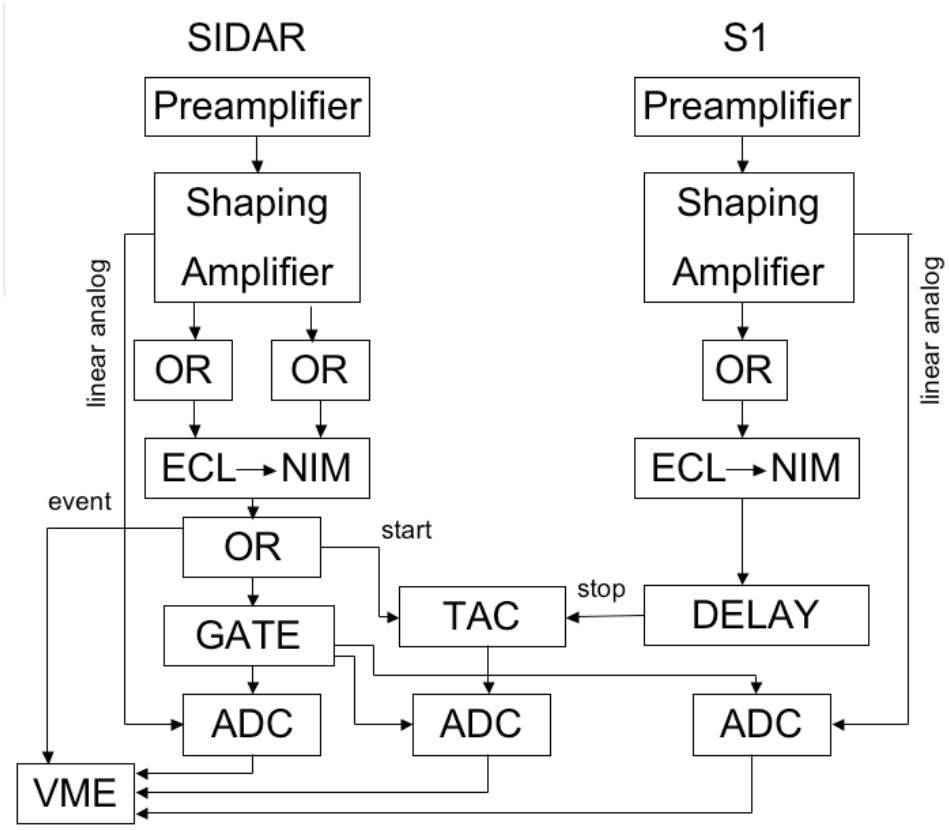

Figure 2.5: Schematic of the electronics setup for the SIDAR and S1 detectors.

The α particles from the (p,α) reaction studies were detected by the SIDAR silicon array (one wedge is shown in Figure 2.3) located 120 mm from the entrance of the chamber. The array consists of 8 YY1 wedges with 16 annular strips per wedge, manufactured by Micron Semiconductor, Ltd [Tho05]. The thicknesses of the wedges used in these studies were 300 μm and 500 μm. The wedges are arranged perpendicular to the axis of the incoming beam so that each strip is concentric with the beam.

Heavy recoils from the (p,α) reaction are detected in a Type S1 detector [Mic05], also know as the CD or MINI detector. This detector is shaped like a compact disc and has an inner(outer) radius of 24 mm (48 mm) with 16 annular strips, sectioned into quadrants (see Figure 2.4). The placement of the S1 detector varied in each study so as to maximize the probablity of detecting the α particle and heavy recoil in coincidence. For the ^{17}O(p,α)^{14}N study, the maximum angle at which the ^{14}N recoils can be emitted is $\theta_{lab} \approx 21^o$, while for the ^{31}P(p,α)^{28}S and ^{35}Cl(p,α)^{32}S studies the maximum heavy recoil angles were $\approx 8^o$ and 7^o respectively (2.5). In order to maximize the efficiency for the detection of the α particle and heavy recoil in coincidence, the S1 detector was placed 14 mm (for the ^{17}O(p,α)^{14}N study) and 210 mm (for the ^{31}P(p,α)^{28}S and ^{35}Cl(p,α)^{32}S studies) downstream of SIDAR. A summary of the geometric and operational parameters for the SIDAR array and S1 detector can be seen in Table 2.1.

A schematic of the electronics setup for the SIDAR array and S1 detector can be seen in Figure 2.5. The signals from each detector are amplified using a preamplifier then sent to a shaping amplifier. The shaping amplifier sends a signal, the height of which is proportional to the detected particle's energy, to the analog-to-digital converter (ADC). The digitized signals from the ADC are sent via the VME bus to a single-board computer and via ethernet to a DAQ workstation. Logic signals from a

leading-edge discriminator are also sent from the shaping amplifiers through a series of OR modules and ECL-NIM converters into a time-to-amplitude converter (TAC) module.

The TAC module creates a signal whose height is proportional to the time between a particle striking a SIDAR detector and a particle striking the S1 detector, with a delay added to the S1 signal. The TAC module starts on the signal from SIDAR and ends with a signal from S1. The time between a signal from SIDAR and the S1 detector can be useful in filtering out unwanted events, since the signals from an α particle in SIDAR and a heavy recoil in the S1 detector will be time-correlated. A gate signal is also created using the SIDAR signal from the OR module, which is sent to the ADC. This gate signal is used to tell the ADC to start searching for a signal from SIDAR. Each ADC is then connected to the VME.

Unreacted beam that scatters off the carbon foil is detected by a two single-collimated silicon surface barrier detectors located at angles of 36^o and 38^o from the beam axis. The solid angle subtended by these detectors was measured, in a separate measurement, using a ^{244}Cm α-source of known decay rate that was placed at the same postion as the carbon foil and illuminated the detector. If the decay rate is R, and the number of α particles hitting the detectors in elasped time Δt is N, then the fraction of the solid angle to the total solid angle subtended by the detector is given by:

$$\frac{\Delta\Omega}{4\pi} = \frac{N}{R\Delta t}$$

The solid angle for the monitor detectors were found to be 1.89 and 1.62 msr in the ^{31}P(p,α)^{28}Si and ^{35}Cl(p,α)^{32}S studies. By comparing the relative yields of ^{12}C and

scattered beam, the angles of each detector can be found using Rutherford scattering ($\theta = 36^o$ and 38^0).

To normalize the data to the integrated incident beam, yields from the ^{12}C(x,^{12}C)x elastic scattering reaction (where x is the incoming beam) are used together with the Rutherford cross section for scattering to determine the integrated beam current for normalization. The thickness of the carbon foil was determined by measuring the energy loss of α particles from a ^{244}Cm source passing through the foil. The carbon areal target density was determined by using the stopping power for α particles in carbon from a SRIM fit to experimental data points (ϵ = (14.5 $\pm$ 0.8) x 10^{-15} eV cm^2). Using this technique, the thickness of the carbon foil used in the (p,α) reaction studies was found to be 32μg/cm^2. [Zie03].

2.5 Reconstructing the (p,α) reaction vertex

The efficiency for detecting both the α particle and the heavy recoil in coincidence is a function of the position of the reaction vertex. When using solid targets, the vertex is automatically known, as it is constrained to be located within an extremely small range within the thin foil. However, when using an extended gas target, the reaction vertex can occur at any place along the beam axis. For this reason, the vertex must be determined on an event-by-event basis using known kinematics of the reaction products.

The energy of the emitted α particle (in channels) from the (p,α) reaction can be obtained from the SIDAR array. Converting this to an energy (in MeV) can be done by knowing the conversion factor from channels to energy (the gain). For this to be of the accuracy needed for the vertex calculation, extremely good gain-matching is needed. From this energy, a small correction for the energy loss of the α particle as it

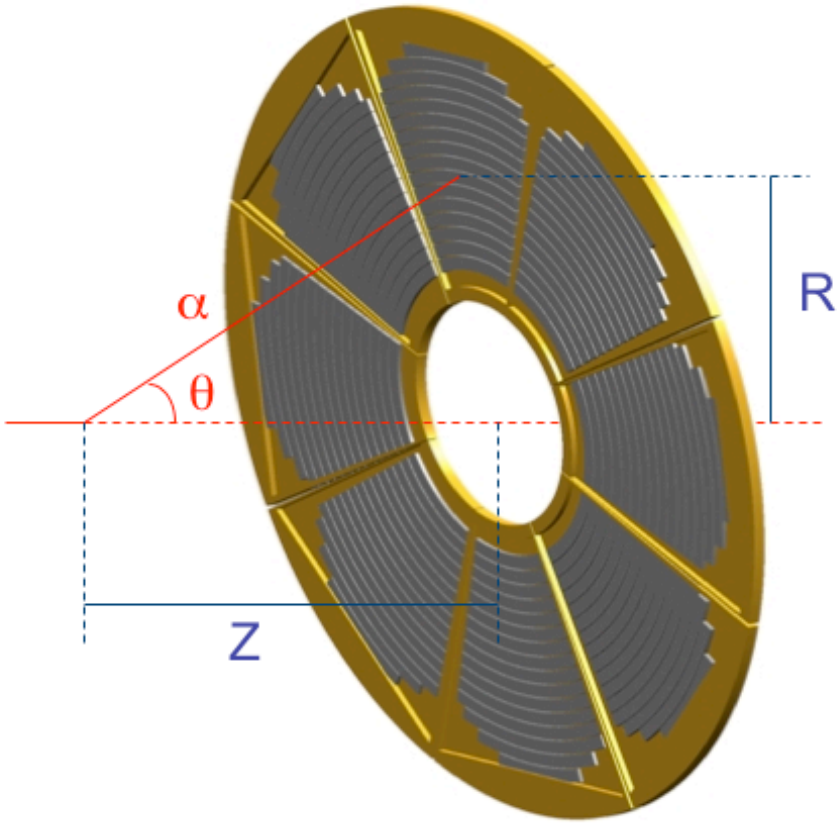

Figure 2.6: Reconstructing the reaction vertex using the segmentation of the SIDAR detector and the energy. In the figure, z is the distance from the reaction vertex to the plane of SIDAR, R is the distance from the beam axis to the strip in which the alpha is detected, and θ is the laboratory angle of the α from the (p,α) reaction.

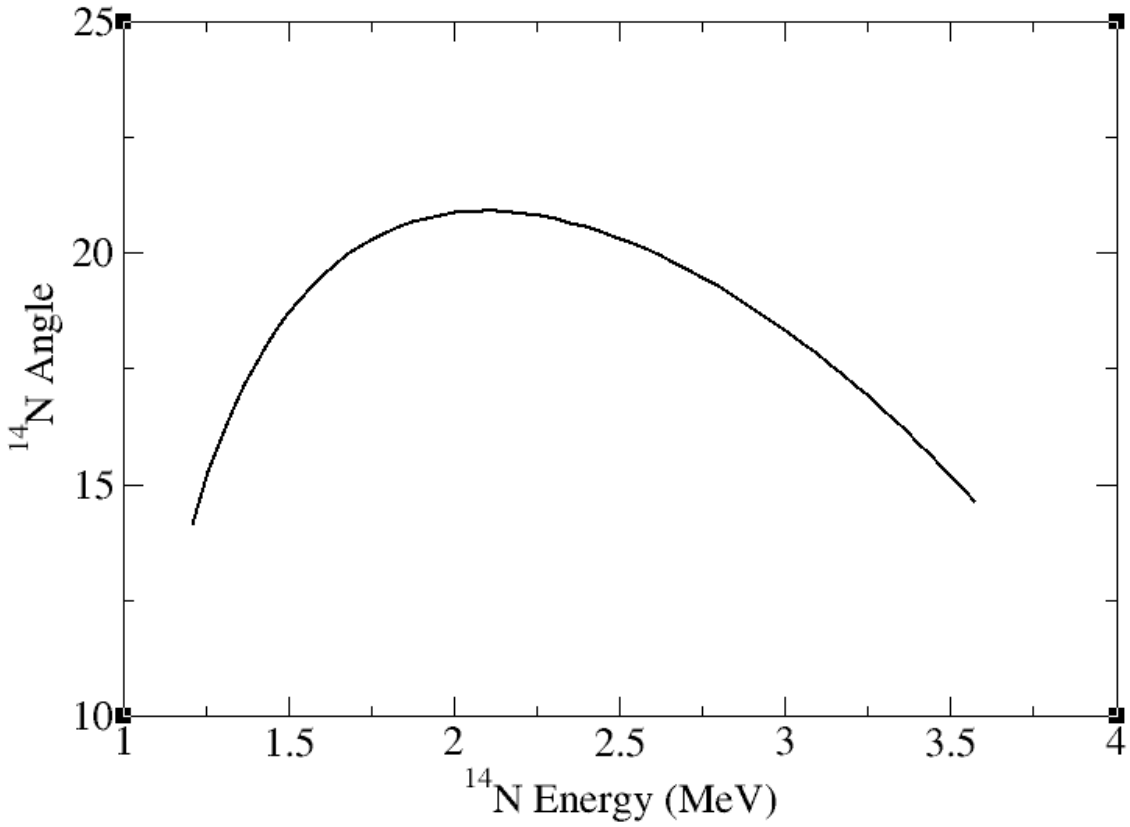

Figure 2.7: Calculated Angle vs. Energy for the ^{14}N recoils in the ^{17}O(p,α)^{14}N reaction at a beam energy of 3.27 MeV. The turnaround angle can be seen to be located at 21^o

travels through the hydrogen gas must be taken into account, which is obtained from a SRIM calculation [Zie03], as well as a correction for the energy loss of the particle as it travels through the dead layer of SIDAR. Overall, the energy of the α particle is given by:

$$E_\alpha = E_{SIDAR} + \Delta E_{gasloss} + \Delta E_{deadlayerloss} \tag{2.1}$$

where E_{SIDAR} is the energy deposited in the SIDAR detector, $\Delta E_{gasloss}$ is the energy lost by the α particles as it travels through the hydrogen gas, and $\Delta E_{deadlayerloss}$ is the energy lost by the α particle going through the dead layer of SIDAR.

The energy of the α particle can be shown from conservation of energy and momentum to be [Kra88]:

$$E_\alpha^{1/2} = \frac{(m_X m_\alpha E_X)^{1/2} cos\theta \pm \left[m_X m_\alpha E_X cos^2\theta + (m_Y + m_\alpha)(m_Y Q + (m_Y - m_X)E_X\right]^{1/2}}{m_Y + m_\alpha} \tag{2.2}$$

where the original labeling from [Kra88] of the reaction X(a,b)Y has been replaced with that of a (p,α) reaction in inverse kinematics (p(X,α)Y). In the above expression, E_α and E_X are the energies of the alpha particle from the (p,α) reaction and the incident beam (assumed to be the resonance energy) respectively, m_X, m_α, and m_Y are the masses of the incoming beam, α particle and heavy recoil, Q is the reaction Q-value, and θ is the laboratory angle of the emitted α particle.

Equation 2.2 can be solved for cosθ (using the plus sign in Eqn 2.2 since only extremely low incident beam energies exhibit double-valued behavior):

$$cos\theta = \frac{A}{\sqrt{E_X E_\alpha}}\left[B^2 E_\alpha - B(m_Y Q + (m_Y - m_X)E_X)\right] \tag{2.3}$$

where

$$A = \frac{1}{2(m_Y + m_\alpha)\sqrt{m_X m_\alpha}}$$

$$B = m_Y + m_\alpha$$

By using the segmentation of the SIDAR array, the distance from the axis of the incoming beam to which the alpha particle struck the SIDAR array (labeled by R in Figure 2.6) can be found. Combining this with the inferred angle from equation 2.3 will give the reaction vertex measured from the plane of SIDAR.

There exists a maximum angle in which the heavy recoils can be emitted in the (p,α) reaction. The heavy recoil angle in the laboratory frame is given by:

$$\phi_{recoil}^{lab} = sin^{-1}\left[sin(\theta_\alpha^{lab})\sqrt{\frac{m_p E_\alpha^{lab}}{m_Y E_{recoil}^{lab}}}\right] \tag{2.4}$$

In Figure 2.7, this angle is plotted against the energy for ^{14}N in the ^{17}O(p,α)^{14}N with an initial beam energy of 3.27 MeV (near the 183 keV resonance energy). The maximum angle at which the ^{14}N recoils can emerge is $\theta \approx 21^o$, corresponding to an angle for the α particle of $\approx 38^o$. If this maximum angle is seen in the S1 detector (showing up as the maximum strip in which ^{14}N recoils from the (p,α) reaction are seen), it can be used in conjunction with the segmentation of the S1 detector to provide a determination of the reaction vertex, independent of SIDAR and the energies of the reaction products.

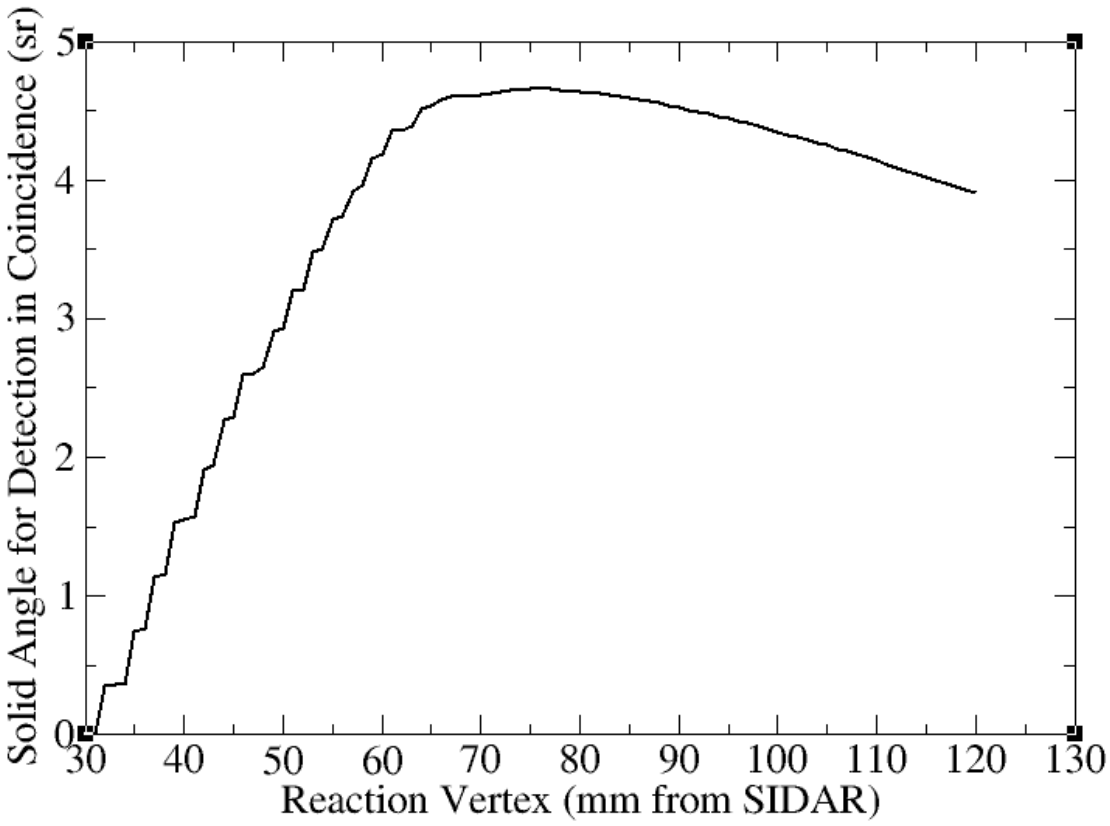

Figure 2.8: Solid angle versus reaction vertex for the 622 keV resonance in the ^{31}P(p,α)^{28}Si reaction.

2.6 Calculating the efficiency for detection in coincidence

In order to properly normalize the data collected in our (p,α) studies, we must calculate the efficiency for detecting the α particle and recoil in coincidence in the SIDAR array and S1 detector, respectively. The efficiency (or solid angle of detection) does not merely encompass the geometric solid angle of the detectors at each reaction vertex, but must also take into account the efficiencies of individual strips in SIDAR and S1 and well as whether or not an α particle striking the SIDAR array will have the corresponding heavy recoil strike the S1 detector. For these reasons we must use the known relative kinematics of the reaction products as well as the measured efficiencies of the strips in the SIDAR and S1 detectors to determine the overall efficiency at a given reaction vertex.

At a given reaction vertex, z, the smallest and largest angle that an alpha particle can strike a given SIDAR strip is given by:

$$\theta_{low} = tan^{-1}\frac{50 + 5(i-1)}{z} \tag{2.5}$$

$$\theta_{high}^{lab} = tan^{-1}\frac{50 + 5i}{z} \tag{2.6}$$

where i is the strip number and the inner diameter and strip width of the SIDAR array (50 mm and 5 mm respectively, 2.4) are used. Each angle corresponds to a unique α energy (equation 2.2) which, for puropses of simplifying the subsequent calculations, can be rewritten as:

$$E_{\alpha}^{lab} = E_T B\left[cos(\theta^{lab}) + \sqrt{D/B - sin^2\theta^{lab}}\right]^2 \tag{2.7}$$

where

$$E_T = Q + E_X$$

$$A = m_X m_Y \frac{E_X}{E_T} \frac{1}{(m_X + m_\alpha)(m_p + m_Y)}$$

$$B = m_X m_\alpha \frac{E_X}{E_T} \frac{1}{(m_X + m_\alpha)(m_p + m_Y)}$$

$$C = m_p m_\alpha \left(1 + \frac{m_X}{m_p}\frac{Q}{E_T}\right) \frac{1}{(m_X + m_\alpha)(m_p + m_Y)}$$

$$D = m_p m_Y \left(1 + \frac{m_X}{m_p}\frac{Q}{E_T}\right) \frac{1}{(m_X + m_\alpha)(m_p + m_Y)}$$

and θ_α will be the angle in the middle of the strip. It must be determined if an α particle originating from given vertex z and having energy E_α^{lab} (given by equation 2.7) will have the corresponding heavy recoil strike the S1 detector. This is most easily determined in the laboratory frame. The energy of the recoil in the laboratory frame is straightforward from conservation of energy:

$$E_{recoil}^{lab} = E_T - E_\alpha^{lab}$$

The strip (if it exists) that the heavy recoil strikes the S1 detector is then given by:

$$m = \frac{((z + x)tan(\phi_{recoil}^{lab}) - 24.75)}{1.5} \tag{2.8}$$

where ϕ_{recoil}^{lab} is given by equation 2.4 and the inner radius and strip width of the S1 detector (24 mm and 1.5 mm respectively, section 2.4) are used and x is the distance between the detectors. In equation 2.8, an extra 0.75 mm (half of the strip width of S1) is added to the inner radius of the S1 detector so that the expression gives the strip as if the middle of the strip was hit (rather than the edge). If the value of m in

equation 2.8 is between 1 and 16 (the number of strips in the S1 detector), the heavy recoil strikes the S1 detector and the reaction products are detected in coincidence.

To calculate the center-of-mass (CM) solid angle for detection in coincidence, the low and high angles in SIDAR can be converted to CM by:

$$\theta_{low}^{CM} = \pi - cos^{-1}\left[\frac{E_{low}^{lab}/E_T - B - D}{2\sqrt{AC}}\right]$$

$$\theta_{high}^{CM} = \pi - cos^{-1}\left[\frac{E_{high}^{lab}/E_T - B - D}{2\sqrt{AC}}\right]$$

where E_{low}^{lab} and E_{high}^{lab} are the alpha particle energies from the angles in equations 2.5 and 2.6.

Then the CM solid angle for the given reaction vertex z and SIDAR strip i is given by:

$$\Delta\Omega_i^{CM} = -2\pi\left[cos(\theta_{low}^{CM}) - cos(\theta_{high}^{CM})\right]\epsilon_{SIDAR}(i)\epsilon_{S1}(m) \tag{2.9}$$

where ϵ_{SIDAR}(i) and ϵ_{S1}(m) are the efficiencies for the corresponding SIDAR and S1 strips (section 2.4). Equation 2.9 must be summed over all of the SIDAR strips(i) to get the total CM solid angle at the given vertex. Overall, the CM solid angle for detection in coincidence at a given reaction vertex is given by:

$$\Delta\Omega^{CM} = -2\pi\Sigma_i\left[cos(\theta_{low}^{CM}(i)) - cos(\theta_{high}^{CM}(i))\right]\epsilon_{SIDAR}(i)\epsilon_{S1}(m)\delta_{\alpha,recoil} \tag{2.10}$$

where

$$\begin{aligned}\delta_{\alpha,recoil} &= 1 \text{ if the } \alpha \text{ and heavy recoil are detected in coincidence}\\ &= 0 \text{ otherwise}\end{aligned}$$

If the emitted α particles from the (p,α) reaction have an isotropic distribution, then the solid angle for detection at a reaction vertex is given completely by equation 2.10. However, if there is some sort of angular distribution, an additional angular dependent factor ($W(\theta_\alpha)$) must be inserted in equation 2.10.

The solid angle versus reaction vertex curve for the 622 keV resonance (with an isotropic distribution) in ^{31}P(p,α)^{28}Si is shown in Figure 2.8. The curve peaks at z = 80 mm from SIDAR and begins to drop off rapidly at z = 65 mm. The rapid drop in solid angle has a step-like behavior as each individual S1 strip (from outer to inner) falls beyond the maximum ^{28}Si recoil angle until finally at z $\approx$ 30 mm, all recoils pass through the center of the S1 detector.

2.7 Limitations of the technique

Though this technique can be employed for many different (p,α) studies, the major limiting factor that determines if it is advantageous over the use of foils concerns the maximum angle of the heavy recoil. The placement of the S1 detector should be such that this maximum angle can be seen. As seen in Figure 2.7, the larger the incoming beam energy or mass, or reaction Q-value the smaller the maximum recoil angle. In order to detect smaller recoil angles, the S1 detector must be positioned further and further back from the SIDAR detector.

However, some scattering of the incoming beam off of the aperture closest to the chamber as well as scattering off the 5 mm hole in the plate inside the chamber is unavoidable since the beam has some diameter (typically a few millimeters). These scatterings are heavily forward focused in the laboratory frame. If the S1 detector is positioned far enough from the entrance of the chamber so that scattered incoming beam impinges upon it, the count rate in the detector could become too large. Also,

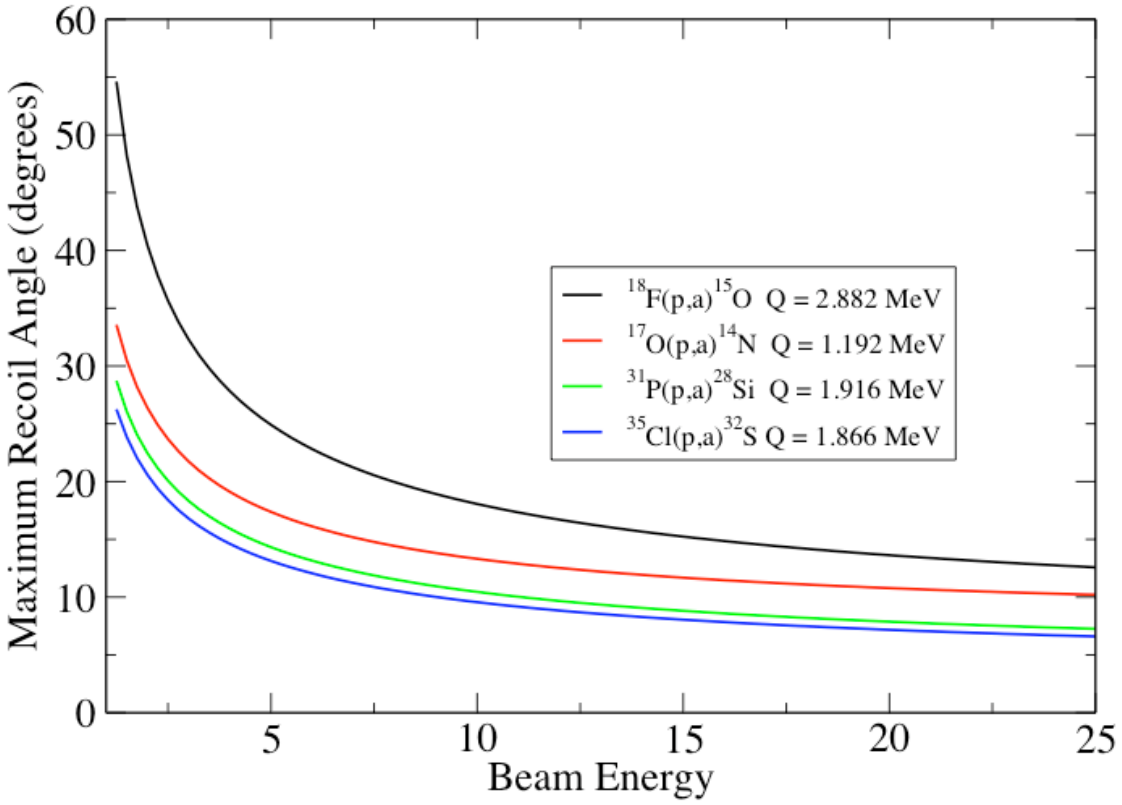

Figure 2.9: Maximum recoil angle (degrees) versus incoming beam energy (MeV) for several (p,α) reactions

since the energy of the scattered beam will be very close to the incoming beam energy, it could pose problems in distinguishing heavy recoils with larger energies from the (p,α) reaction from the scattered beam. Therefore, this technique is best suited for (p,α) reactions with lower mass incoming beams and larger Q-values.

Table 2.1: Operational and Geometric parameters for the SIDAR and S1 detectors

	SIDAR	S1
Inner Radius (mm)	50	24
Outer Radius (mm)	130	48
Number of Strips	16	16
Strip Width (mm)	5	1.5
Strip Efficiencies		
1	0.933	1.000
2	0.933	1.000
3	0.933	0.933
4	0.933	0.985
5	0.933	0.978
6	0.933	0.971
7	0.933	0.964
8	0.933	0.956
9	0.933	0.949
10	0.933	0.942
11	0.933	0.935
12	0.933	0.927
13	0.933	0.920
14	0.800	0.878
15	0.622	0.777
16	0.400	0.804

Chapter 3

The ^{1}H(^{17}O,α)^{14}N Reaction Study

3.1 Motivation

The rates of the ^{17}O(p,α)^{14}N and ^{17}O(p,γ)^{18}F reactions are important for understanding isotopic abundances in giant stars and novae. The ^{17}O isotope is abundantly produced in novae and may be the dominant contributor to ^{17}O production in the galaxy [Jos98]. The ^{17}O(p,γ)^{18}F reaction leads to the production of ^{18}F, whose potentially observable beta-decay γ-rays have made it a proposed target of γ-ray astronomy since its relatively long half-life ($\tau \approx 2$ hr) means that it can survive the inital explosion. However, the ^{17}O(p,α)^{14}N reaction bypasses production of the ^{18}F isotope. The competition between the (p,α) and (p,γ) reactions on ^{17}O can have a profound effect on the final abundance of ^{18}F in a nova explosion.

The properties of a resonance at $E_{cm} = 183$ keV have been shown to dominate the ^{17}O(p,α)^{14}N and ^{17}O(p,γ)^{18}F reaction rates in the temperature range T $\approx$ 1-4 GK, which are relevant to novae and asymptotic giant branch (AGB) stars. The strength of this resonance in the ^{17}O(p,α)^{14}N reaction was measured at Orsay ($\omega\gamma_{p\alpha} = 1.6 \pm 0.2$ meV) [Cha05], and found to be over 50 times greater than the inferred strength from

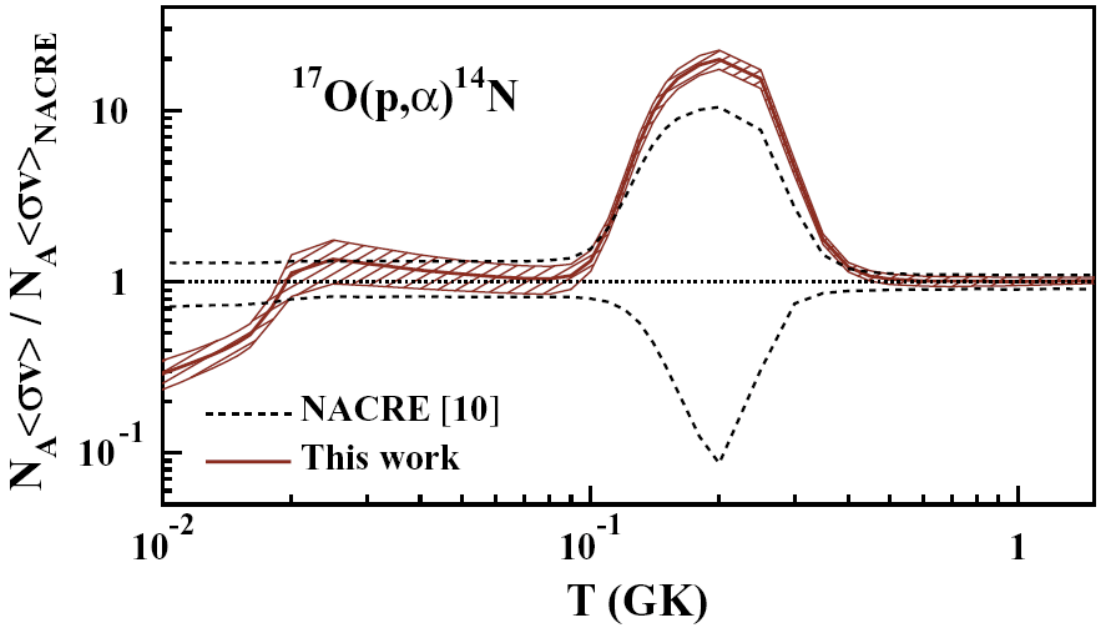

Figure 3.1: The ratio of the ^{17}O(p,α)^{14}N reaction rate (solid line) [Cha07] to the previous rate [Ang99] (also known as the NACRE rate). The dashed lines indicate the previous [Ang99] lower and upper limits for the total rate. Figure taken from Ref. [Cha07].

an ^{17}O(p,γ)^{18}F study at Triangle Universities Nuclear Laboratory (TUNL) ($\omega\gamma_{p\alpha} <$ 0.03 meV) [Fox04]. This discrepancy in the strength of the 183 keV resonance has a large impact on the isotopic abundances of ^{17}O and ^{18}F, with a reduction of as much as a factor of 8 in ^{18}F production in novae using the higher ^{17}O(p,α)^{14}N rate [Cha05]. Figure 3.1 shows the reaction rate using the larger resonance strength as compared to the previous result [Ang99]. An independent measurement of this resonance strength would resolve this descrepancy. This measurement would also serve as a good test of the newly-developed experimental technique described in chapter 2.

3.2 Experimental Approach and Data

The experimental setup was the same as that described in section 2.2. Low-energy pure beams of stable ^{17}O with an intensity of $\approx$ 1 pnA from the Holifield Radioactve Ion Beam Facility (HRIBF) bombarded hydrogen gas which filled the scattering chamber at pressures of up to 4 Torr.

The α and ^{14}N recoils from the ^{1}H(^{17}O,α)^{14}N reaction were detected in coincidence within the gas-filled chamber by the SIDAR silicon detector array and the S1 detector, respectively (section 2.4). The SIDAR array was located 115 mm from the entrance of the chamber, while the S1 detector was positioned 14 mm downstream of SIDAR. Both detectors were individually calibrated using a ^{244}Cm source.

The solid angle for detection of both recoils in coincidence (section 2.6) is plotted against the reaction vertex (as measured fron the plane of the SIDAR array) in Figure 3.2. The efficiency for detection in coincidence is nearly constant for most of the range of vertices, but falls rapidly for positions closer to SIDAR as ^{14}N recoils begin to pass throught the center of the S1 detector.

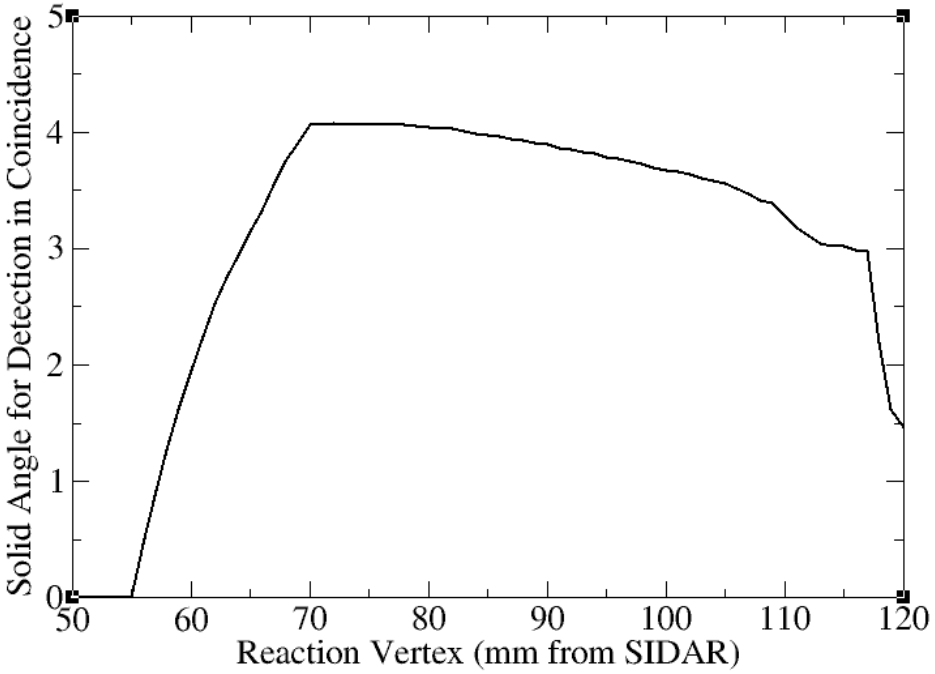

Figure 3.2: Total solid angle (center-of-mass frame) for detection of α particles in coincidence with detection of the ^{14}N recoil versus the reaction vertex (measured from the plane of SIDAR) for the E_{cm} = 183 keV resonance in ^{17}O(p,α)^{14}N

The kinematics and relative timing of the two detected particles allowed the ^{1}H(^{17}O,α)^{14}N events to be clearly identified. In Figure 3.3, the energies of the particles detected by the S1 detector are plotted against the energies detected by SIDAR for events coincident within 0.4 μs. The data shown are for two bombarding energies (3.29 MeV (off-resonance) and 3.34 MeV (on-resonance)) with comparable integrated incident beam. The ^{1}H(^{17}O,α)^{14}N events can be distiguished as a straight line with a constant energy sum, indicative of the reaction Q-value. The gate drawn in Figure 3.3 determined the number of ^{1}H(^{17}O,α)^{14}N events, Y.

The segmentation of SIDAR and the energy of the emitted α particle were used to determine the reaction vertex for ^{1}H(p,α)^{14}N events (section 2.5). In Figure 3.4, the reaction yield is plotted versus distance from the reaction vertex to the plane of SIDAR, z, for two different bombarding energies. All of the ^{1}H(p,α)^{14}N events originate from a narrow range inside the chamber, indicative of a narrow resonance. Small corrections to the measured α energy were made for the energy loss of the particle as it traveled through the hydrogen gas and the energy loss as the particle traveled through the dead layer of SIDAR (1% and 6%, respectively for a 2 MeV α particle at $\theta_{lab} = 45^{o}$). The energy loss of the incident ^{17}O beam ($\approx$ 2%) does not significantly contribute since the reaction originates from a well-defined resonance energy.

The reaction vertex varies linearly with incident beam energy and a least-squares fit to the data gives the stopping power of oxygen ions in hydrogen to be $\epsilon = (63 \pm 1)$ x 10^{-15} eV cm^{2} at E(^{17}O) = 194 keV/u. This result is interesting in itself since it is the only measurement of the stopping power of oxygen ions in hydrogen near the peak of the Bragg curve.

The reaction vertex was also determined using the ^{14}N recoils and the segmentation of the S1 detector (secion 2.5). In Figure 3.5, the best fit to the distribution

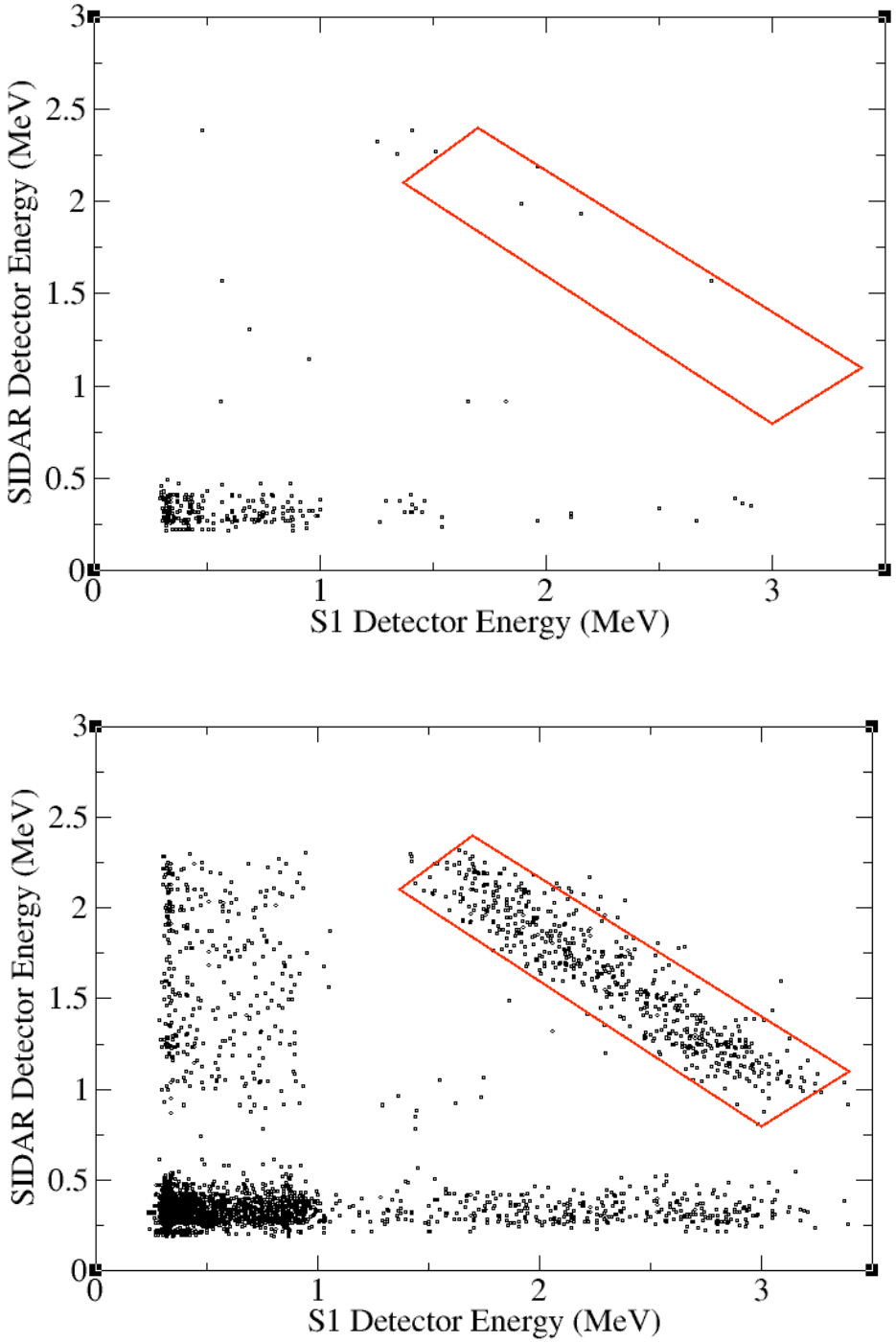

Figure 3.3: The energy of particles detected in the S1 detector plotted against the energy of coincident particles in SIDAR for incident ^{17}O energies of 3.29 MeV (off-resonance - top figure) and 3.34 MeV (on-resonance - bottom figure). The drawn box is where (p,α) events are expected to fall.

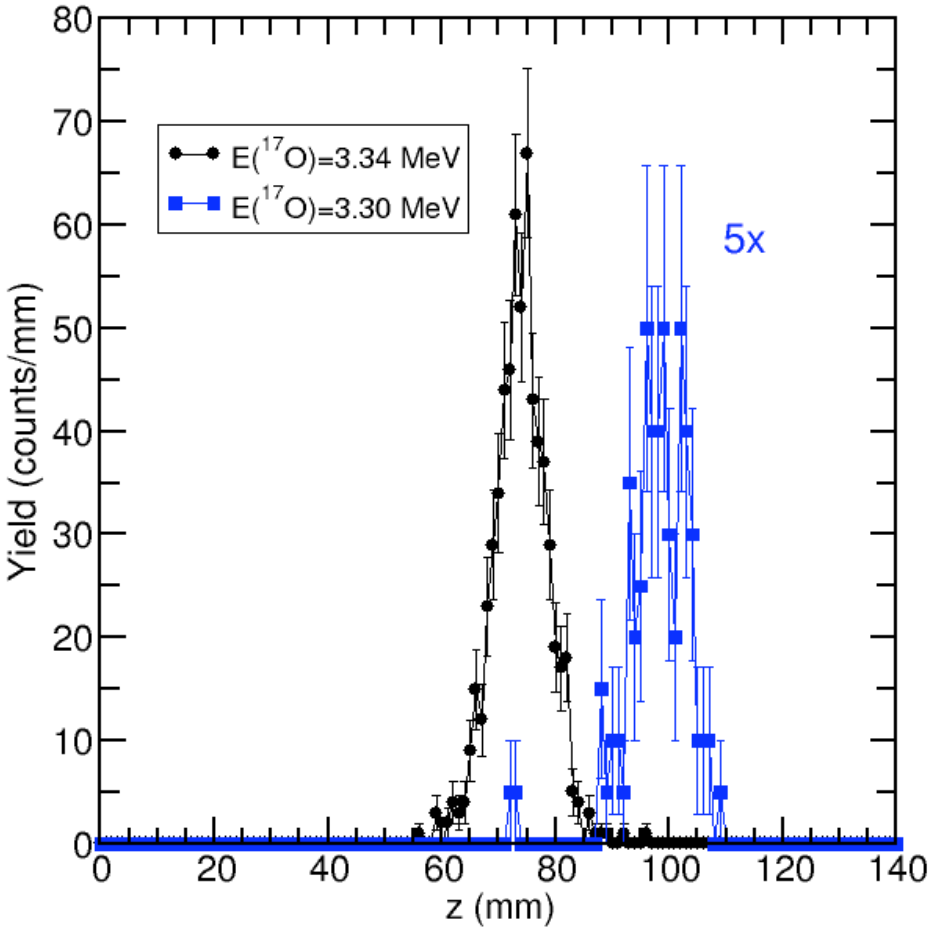

Figure 3.4: The distribution of ^{1}H(^{17}O,α)^{14}N events as a function of the distance (z) from the plane of SIDAR (mm) at a pressure of 4 Torr. The 3.30 MeV yield has been multiplied by a factor of 5 for purposes of comparison.

Table 3.1: Results for the stopping power for oxygens in hydrogen gas at 193 keV/u compared to the semi-empirical models SRIM 2003 [Zie03] and MSTAR [Pau03]

	ϵ (10^{-15} eV cm^2
Present Work	63 ± 1
SRIM 2003 [Zie03]	59
MSTAR [Pau03]	53

shows the maximum angle for the ^{14}N recoils falling at approximately strip 7 on the S1 detector (corresponding to a ^{14}N recoil angle of $\approx 21^o$).

In Figure 3.6, the incident ^{17}O energy is plotted against the reaction vertex as measured from SIDAR (using the detected α particles) and the S1 detector (using the ^{14}N recoils). Using a least-squares fit for the S1 detector data gives a stopping power of $\epsilon = (64 \pm 3)*10^{-15}$ eV cm^2. A weighted average for the two techniques was adopted. Table 3.1 compares the present value found in this study with two widely used semi-empirical models. It should be noted that the values found for the reaction vertices as determined by the two techniques agree (within uncertainty) by the measured geometric distance between the SIDAR array and the S1 detector (14 mm).

The integrated beam current at each energy was determined by normalizing to ^{12}C(^{17}O,^{12}C)^{17}O elastic scattering measured simultaneously with the ^{1}H(^{17}O,α)^{14}N reaction using a carbon foil and two single-collimated surface barrier detectors (monitor detectors) (section 2.4). The solid angles for the monitor detectors were determined by placing a calibrated α source at the same position as the carbon foil (in a separate measurement) and found to be 0.42 ± 0.01 and 0.50 ± 0.01 msr. A sample spectrum is shown in Figure 3.7. The mean scattering angle for both detectors was determined by using the ratio of ^{17}O to ^{12}C yields. Values of 33^o and 32.4^o were adopted, in good agreement with the measured geometry. The number of incident ^{17}O ions was determined from the ^{17}O yield in each monitor detector by using the Rutherford cross

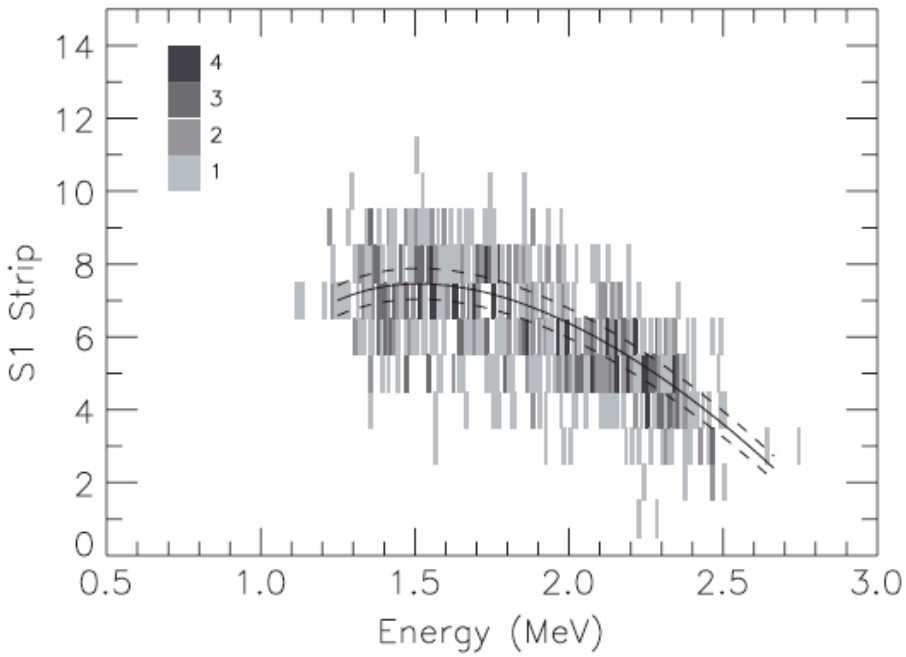

Figure 3.5: The distribution of ^{1}H(^{17}O,α)^{14}N events by ^{14}N angle (strip number) for an incident ^{17}O beam energy of 3.34 MeV. The solid curve shows the best fit to the distrubution by varying the distance to the reaction vertex. The dashed curves represent the upper and lower 1σ limits.

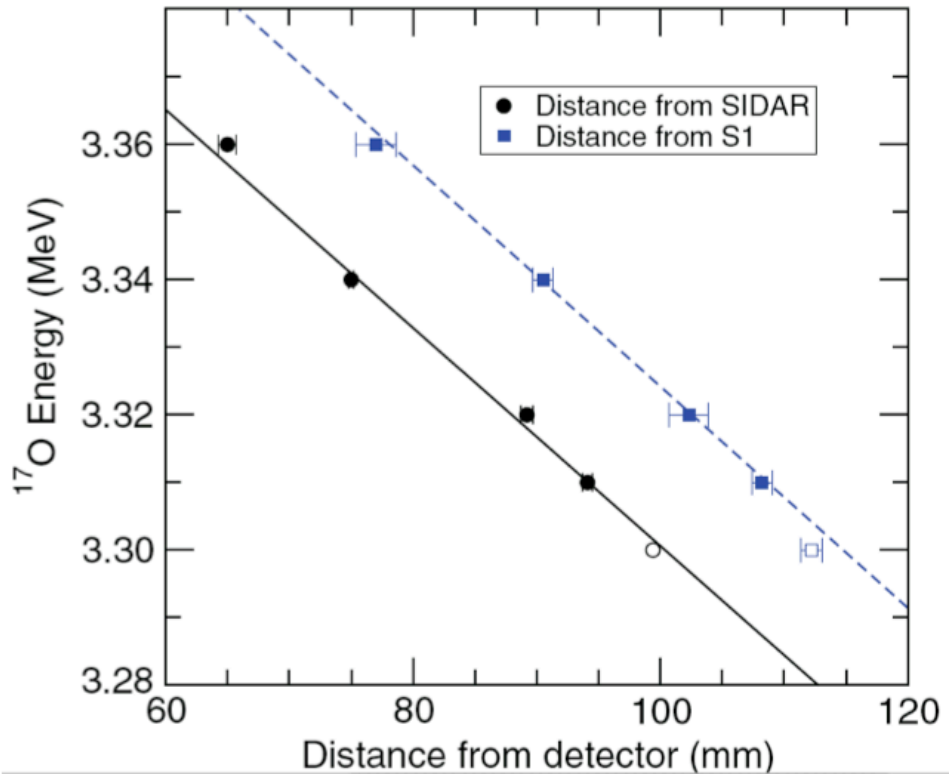

Figure 3.6: Incident beam energy plotted versus the distance to SIDAR (circles) and the S1 detector (squares). The fits do not take into account the lowest incident beam energies where the resonance was not completely contained within the chamber.

section for the ^{12}C(^{17}O,^{12}C)^{17}O reaction. The integrated beam current as determined from each detector typically differed by 6% to 8% and by at most 11%. A weighted average of the two intensities was adopted for each beam energy and the uncertainty reflects both measurements.

3.3 Results

Since the yield originates from a narrow resonance, the resonance strength $\omega\gamma_{p\alpha}$ is related to the yield, Y, to a good approximation, by [Rol88]:

$$\omega\gamma_{p\alpha} = \frac{2}{\lambda^2}\frac{m_p}{m_p + m_{17}} 4\pi\varepsilon \left(\frac{Y}{I\Delta\Omega_{CM}}\right) \tag{3.1}$$

where λ is the wavelength of the incident ^{17}O in the center-of-mass frame, m_p and m_{17} are the masses of the proton and ^{17}O, ε is the stopping power for ^{17}O ions in hydrogen gas, I is the number of incident ^{17}O particles and $\Delta\Omega$ is the efficiency for detection in coincidence given by equation 2.10.

The distribution of yield over the center-of-mass angles covered in this study (θ_α = 70^o - 130^o) was found to be consistent with either an isotropic distribution or with a distrubution from [Cha05] given by:

$$W(\theta_\alpha) = 1 + 0.16 P_2 cos(\theta_\alpha) \tag{3.2}$$

where $P_2 cos(\theta_\alpha)$ is the second-order Legendre polynomial. The distribution in this study was slightly better fit ($\chi^2 \leq 0.1$ lower) using equation 3.2 than with an isotropic distribution. Although not statistically significant, equation 3.2 was adopted, which results in a 6% smaller coincidence efficiency.

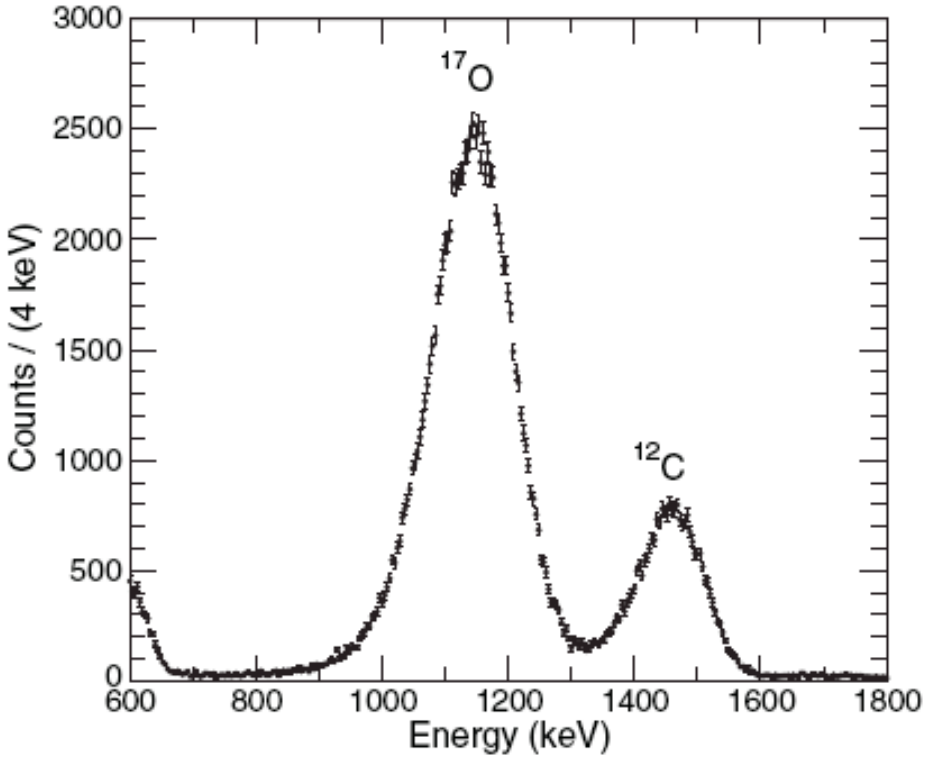

Figure 3.7: Energy spectrum from one of the monitor detectors.

In Figure 3.8, the quantity in parenthesis in equation 3.1 is plotted against the incident beam energy for two data sets taken at different pressures. For incident beam energies with an insufficient number of events to determine a reaction vertex (off-resonance points), an upper limit was set (95% confidence) using the average solid angle for the "on-resonance" points. Also shown in Figure 3.8 are fits to both yield curves which vary the resonance strength, resonance energy, and resonance width. These fits were able to determine an upper limit to the total resonance width ($\Gamma <$ 0.1 keV) at a 95% confidence level.

The resonance strength is mostly independent of the other resonance parameters, and a value ($\omega\gamma_{p,\alpha} = (1.70 \pm 0.09)$ meV) was obtained from the best fit to the data shown in Figure 3.8. The three largest sources of purely systematic uncertainties that potentially impact the overall normalization are the thickness of the carbon foil (6% from the uncertainty in stopping power for α particles in carbon), the strength of the α source used for determining the solid angle of the monitor detectors (section 2.4) (3%), and the stopping power for ^{17}O ions in hydrogen gas (2% as determined in this study). Adding these in quadrature with the results from the fit to the yield curve gives a resonance strength of $\omega\gamma_{p,\alpha} = 1.70 \pm 0.15$ meV.

The best fit to the data at 1 Torr results in a resonance energy that is $\Delta E(^{17}O) =$ 15 keV lower in the laboratory frame than the fit at 4 Torr when identical widths are used. A second value for the resonance energy was extracted by linear extrapolation to zero pressure of the resonance energy obtained from fits to the yield curves with $\Gamma \approx 0$. The result for this method is $\Delta E(^{17}O) = 20$ keV lower in the laboratory frame than the best-fit value at 4 Torr. The uncertainty in the resonance energy was determined from the extrapolation by including appropriate correlations between the uncertainty in the resonance energy and the uncertainty in the width. Since the observed width may result from experimental effects (beam resolution for example)

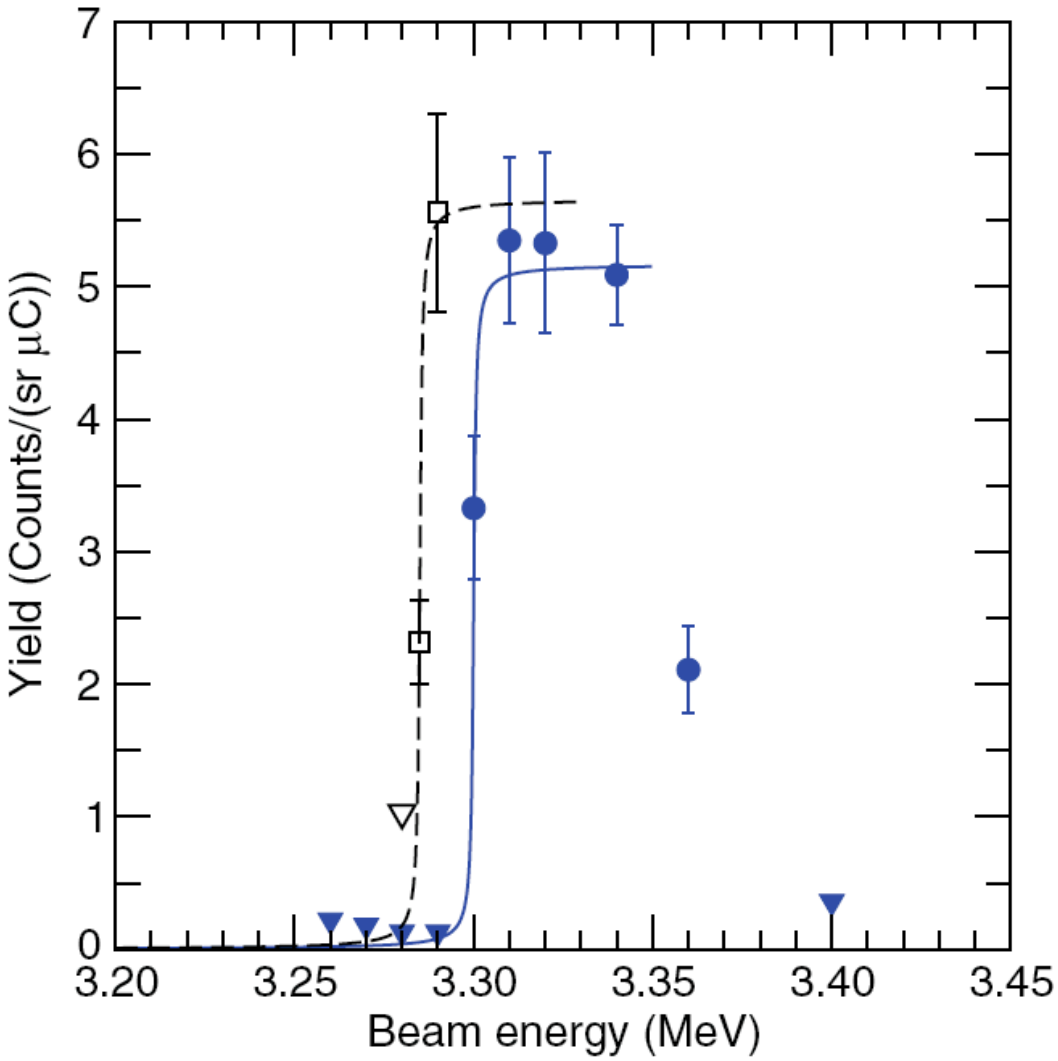

Figure 3.8: Yield curves taken at pressures of 4 Torr(filled circles) and 1 Torr(open squares). Filled(open) trianges represent upper limits. The dashed(solid) lines are fits to the data

Table 3.2: Results of previous and present ^{17}O(p,α)^{14}N studies.

	E_r (keV)	$\omega\gamma_{p,\alpha}$ (meV)
Present Work	$183.5\ ^{0.1}_{-0.4}$	1.70 ± 0.15
Chafa *et al.* [Cha05]	183.2 ± 0.6	1.6 ± 0.2

and since only upper limits were determined for the off-resonance points and for the total width, the uncertainty in the resonance energy is asymmetric, with the result of $E_r = 183.5\ ^{0.1}_{-0.4}$ keV. Table 4.3 compares the results of the previous study and the present findings. The results from the present study are in good agreement with the findings of Chafa *et al.* [Cha05].

3.4 Astrophysical Implications

The contribution from the 183 keV resonance to the ^{17}O(p,α)^{14}N astrophysical reaction rate can be expressed in the narrow, isolated resonance approximation (equation 1.39) as:

$$N_A < \sigma\nu >_{183keV} \approx 276 T_9^{-3/2} exp(-2.128/T_9) \tag{3.3}$$

where a weighted average of the current results and previous results [Cha05] were adopted. The total cross section for the ^{17}O(p,α)^{14}N reaction rate was calculated using the R-matrix code SAMMY [Lar06]. Resonance properties were taken from [Ang99], except for the 183 and 530 keV resonances. A weighted average of the present results and those of Ref. [Cha05] were used for the properties of the 183 keV resonance, as described in section 3.3. The contribution of the 530 keV resonance made an insignificant contribution to the total reaction rate, therefore a strength of $\omega\gamma_{p,\alpha} = 0$ was adopted for this resonance. The adopted resonance properties are summarized in Table 3.3.

Table 3.3: Adopted resonance parameters for the reaction rate calculations. Resonance properties taken from Ref. [Ang99] except where noted.

E_r (keV)	$\omega\gamma_{p,\alpha}$ (eV)
66.0	5.5 x 10^{-9}
183.5	1.65 x 10^{-6} [a]
489.9	49
556.7	2.25
633.9	35.5
635.5	19.7
655.5	5.0
676.7	704.0

[a] Weighted average of present work and Ref. [Cha05]

The reaction rate was calculated by numerically integrating the calculated cross sections using SAMMY. A total reaction rate was found that is in good agreement (differing by at most 4%) with the recommended rate from [Cha07]. This rate is also in good agreement with [Ang99], differing by less than 4% for $T_9 < 0.5$.

The new total ^{17}O(p,α)^{14}N was parameterized in a widely-used format:

$$N_A < \sigma\nu >= \sum_{i=1}^{3} exp\left(a_{i1} + \sum_{j=2}^{6} a_{ij} T_9^{2j/3-7/3} + a_{i7} ln T_9\right) \tag{3.4}$$

from [Ang99] using online tools available from the Computation Infrastructure for Nuclear Astrophysics (CINA) [CINA]. The coefficients in equation 3.4 determined from a best fit to the new ^{17}O(p,α)^{14}N reaction rate are given in Table 3.4. The ^{17}O(p,γ)^{18}F reaction rate from [Ang99] was also parameterized and the coefficients are given in Table 3.5. These parameterizations are valid over the entire temperature range and deviate less than 5% [2%] from the numerically integrated ^{17}O(p,α)^{14}N [^{17}O(p,γ)^{18}F] rates. Figure 3.9 shows the previous (NACRE) ^{17}O(p,α)^{14}N reaction rate as well as the reaction rate from the present work using the new strength for the

Table 3.4: The 21 coefficients a_{ij} used to parameterize the $^{17}O(p,\alpha)^{14}N$ rate via a fit of equation 3.4 to the numerically integrated rate. The parameterization is valid over the temperature range 0.01-10 GK and reproduces the rate to within 5% over this range.

j/i	1	2	3
1	-1.01810 x 10^2	7.98035 x 10^{-1}	2.87049 x 10^2
2	-7.79071 x 10^2	2.95898 x 10^0	2.70110 x 10^{-1}
3	-1.12473 x 10^1	-2.23640 x 10^2	-1.37840 x 10^2
4	2.10956 x 10^2	2.40491 x 10^2	-7.76691 x 10^2
5	-1.38581 x 10^2	-1.04420 x 10^1	2.22662 x 10^3
6	2.32187 x 10^1	4.70954 x 10^{-1}	-3.08826 x 10^3
7	-1.34335 x 10^1	-1.36987 x 10^2	-8.66862 x 10^1

183 keV resonance. The deviation in the $0.1 > T_9 > 0.4$ temperature range is due to the larger 183 keV resonance strength.

The impact of the new ^{17}O + p rates was studied using CINA. A "post processing" approach similar to Parete-Koon *et al.* [Par03] was utilized following a reaction network through time profiles of temperature and density in 28 radial zones taken from one-dimensional hydrodynamic calculations of nova outbursts on 1.15, 1.25, and 1.35 $M_\odot$ ONeMg white dwarf stars [Sta98]. A full reaction network was used in each zone with 169 isotopes. Reaction rates were taken from the NACRE collaboration [Ang99] where available and otherwise from the REACLIB database [Rau01]. Models were also calculated by using the new $^{17}O(p,\alpha)^{14}N$ and $^{17}O(p,\gamma)^{18}F$ reaction rates with all other reaction rates unchanged. The final abundances were determined by summing the contributions of each zone weighted by the total mass of the zone.

Models using the new rates were found to reduce the production of ^{18}F by a factor of 10 with hydrodynamic profiles from a 1.15 $M_\odot$ white dwarf (Figure 3.10). This was comparable to reductions in ^{18}F production by a factor of 7.9 reported from full hydrodynamic simulations on a 1.15 $M_\odot$ white dwarf by Chafa *et al.* [Cha05]. However, the impact of the new ^{17}O + p reaction rates have less influence on ^{18}F

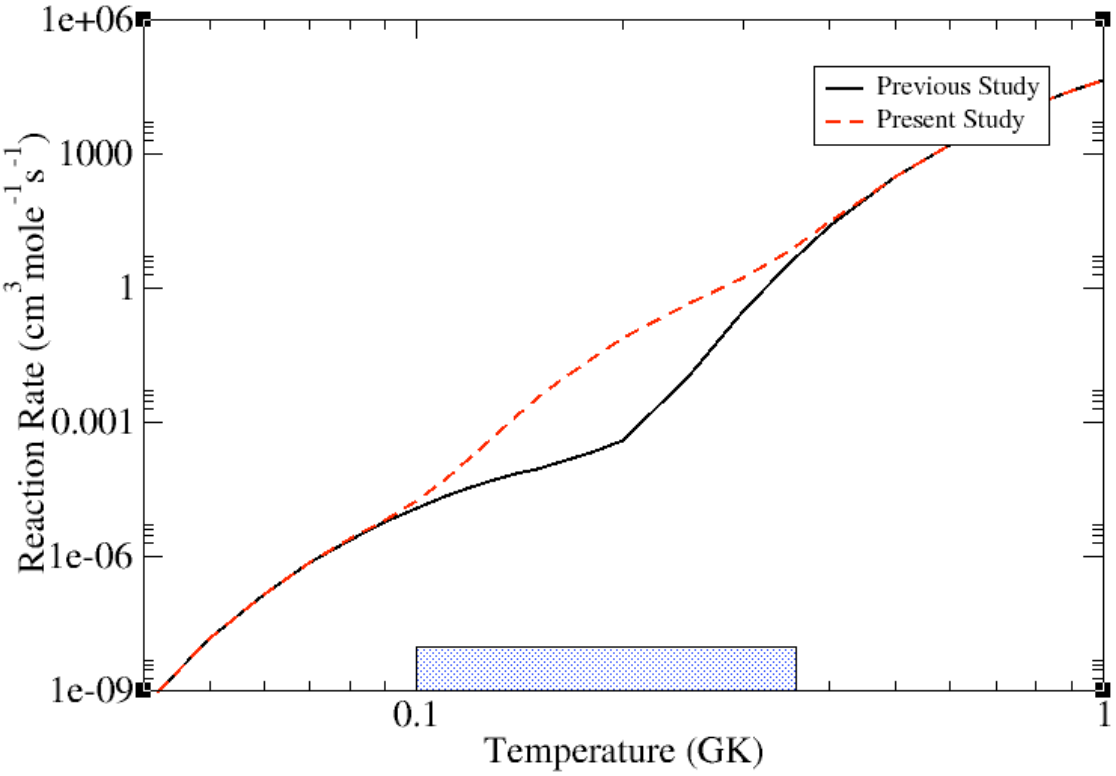

Figure 3.9: The ^{17}O(p,α)^{14}N reaction rate as a function of temperature. The black curve is from a parametrization of the NACRE reaction rate [Ang99] while the red curve utilizes the new 183 keV resonance strength. The shaded region indicates nova temperatures.

Table 3.5: The 21 coefficients a_{ij} used to parameterize the $^{17}O(p,\gamma)^{14}N$ rate via a fit of equation 3.4 to the tabulated rate from [Cha07]. The parameterization is valid over the temperature range 0.01-10 GK and reproduces the rate to within 2% over this range.

j/i	1	2	3
1	-9.18598 x 10^2	-5.57168 x 10^1	6.77712 x 10^3
2	-2.28606 x 10^0	-4.92403 x 10^{-1}	-2.75532 x 10^0
3	3.19374 x 10^1	2.47608 x 10^1	8.93484 x 10^2
4	1.31299 x 10^3	7.43767 x 10^1	-1.05467 x 10^4
5	-6.56844 x 10^2	-4.97559 x 10^1	4.94580 x 10^3
6	2.17931 x 10^2	1.17175 x 10^1	-2.34713 x 10^3
7	-1.33934 x 10^2	1.83200 x 10^1	1.84163 x 10^3

production as the mass of the white dwarf increases. The new reaction rates reduce ^{18}F production by only a factor of 2 in the 1.25 solar mass model (Figure 3.10) and have a negligible effect on the 1.35 solar mass model. This results from the reaction sequence $^{16}O(p,\gamma)^{17}F(p,\gamma)^{18}Ne(\beta)^{18}F(p,\alpha)^{15}O$ that bypasses ^{17}O becoming more important for more energetic novae owing to the strong temperature dependence of the $^{17}F(p,\gamma)^{18}Ne$ reaction rate [Bar00] (Figure 3.11). The much stronger influence of the ^{17}O + p reaction rates in lower mass white dwarf simulations results from the decreased $^{17}F(p,\gamma)^{18}Ne$ reaction rate relative to ^{17}F β-decay in cooler models.

The final abundance of ^{18}F in each model is strongly dependent on the somewhat uncertain $^{17}F(p,\gamma)^{18}Ne$ reaction rate. The $^{17}F(p,\gamma)^{18}Ne$ reaction rate in the previous nova simulations was taken from the NACRE reaction rate compilation [Ang99]. However, measurements over the last several years, most notably by Bardayan [Bar00] and Chipps [Chi09], have reduced this reaction rate by approximately a factor of 10 at temperatures of 0.3 GK and higher (see Figure 3.11). Nova simulations using this new $^{17}F(p,\gamma)^{18}Ne$ reaction rate showed no significant change in the ^{18}F ratio than that found with the previous $^{17}F(p,\gamma)^{18}Ne$ reaction rate. This is because while the new $^{17}O(p,\alpha)^{14}N$ reaction rate deviates from the previous rate in the temperature

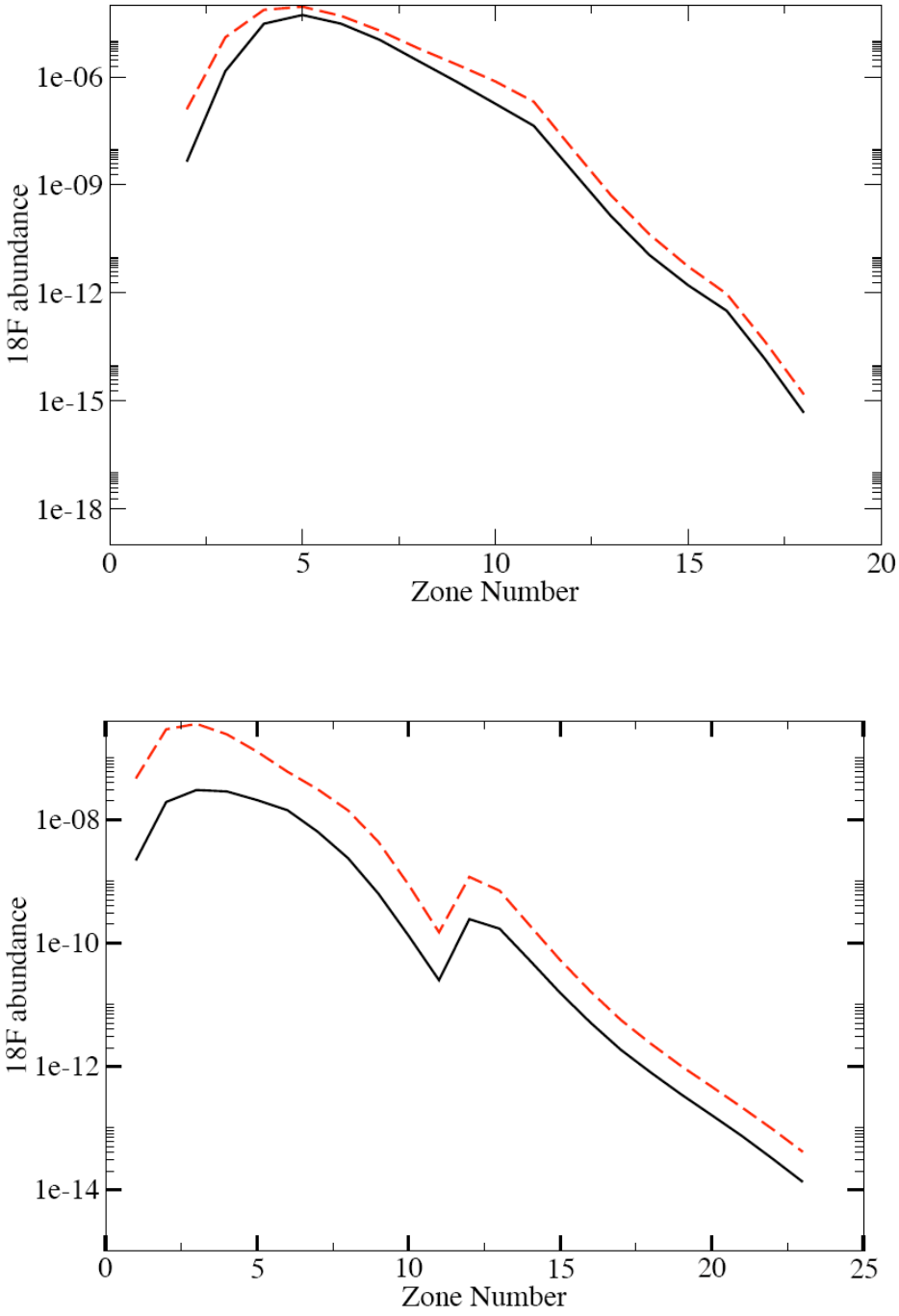

Figure 3.10: Final ^{18}F abundances by zone from simulations of a 1.25 (top) and 1.15 (bottom) $M_{\odot}$ white dwarf. The red(dashed) curve utilize the reaction rates from [Ang99] while the black(solid) curve changes only the strength of the 183 keV resonance in ^{17}O(p,α)^{14}N to that of the findings of the present study.

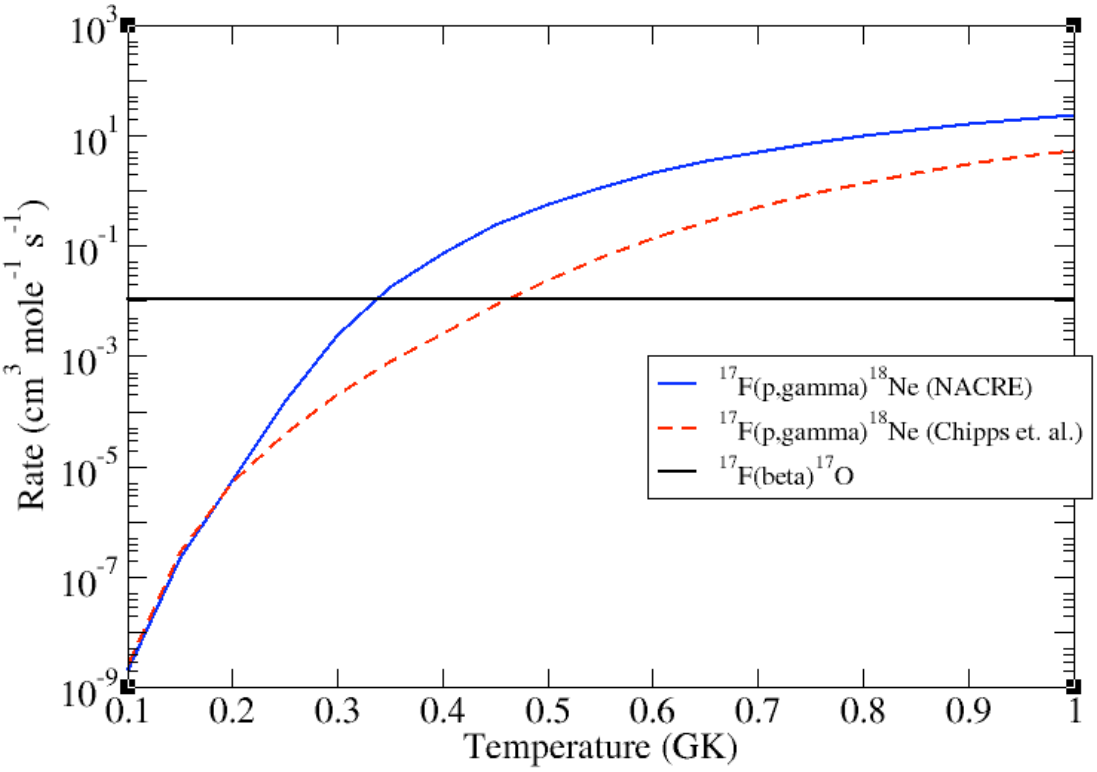

Figure 3.11: The competing ^{17}F(β)^{17}O and ^{17}F(p,γ)^{18}Ne reaction rates. The blue (solid) curve is the ^{17}F(p,γ)^{18}Ne reaction rate from Ref. [Ang99] while the red (dashed) is from the more recent study by Chipps et al. [Chi09].

Table 3.6: Ratio of the final ^{18}F abundance produced in ONeMg nova models using the reaction rates from Ref. [Ang99] to the final ^{18}F abundance in models using the rates from Tables 3.4 and 3.5.

Mass	^{18}F ratio
1.15 $M_\odot$	10.2
1.25 $M_\odot$	2.0
1.35 $M_\odot$	1.0

range T_9 = 0.1 - 0.3 (Figure 3.9), the change in the ^{17}F(p,γ)^{18}Ne rate in this same temperature range is minimal in comparison to the ^{18}F β-decay.

Chapter 4

The ^{1}H(^{31}P,α)^{28}Si and ^{1}H(^{35}Cl,α)^{32}S Reaction Studies

4.1 Motivation

Explosive hydrogen burning in novae, X-ray bursts and supernovae moves CNO cycle material into the heavier Fe-Ni region. While proton capture reactions will transfer material into heavier regions, β-decay and (p,α) reactions move material back to lower mass regions. Reaction cycles have been proposed in the Si-Ar region [Ili93] with the strength of these cycles depending on the ratio of the competing (p,γ) and (p,α) reactions on ^{31}P and ^{35}Cl. Two possible SiP and SCl cycles are shown in figure 4.1.

Resonance strengths for the ^{31}P(p,γ)^{32}S and ^{35}Cl(p,γ)^{36}Ar reactions are well-known in the energy range $E_{cm} \geq 400$ keV, however, only upper limits have been established for possible lower energy resonances [Ros95]. This is not particularly problematic, since the reaction rates can be well-approximated by Hauser-Feshbach

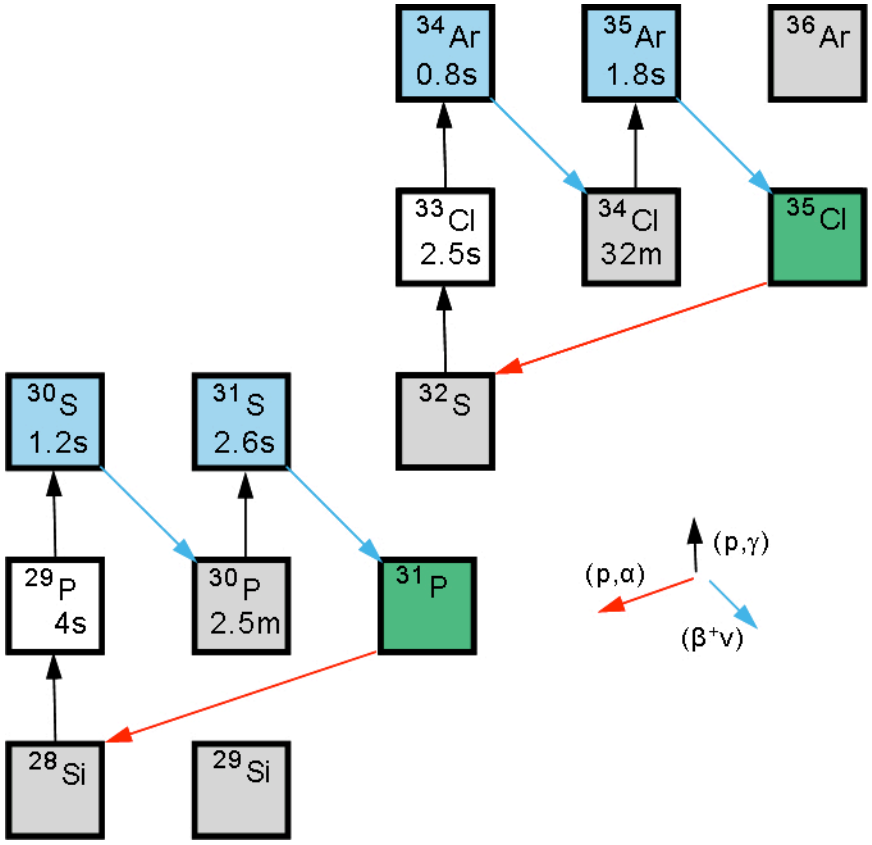

Figure 4.1: Possible cycles in the sequence of reactions in the SiP and SCl regions.

calculations due to the high level density in the compound nuclei [Ili93] [Ili94]. However, this is not the case for the competing ^{31}P(p,α)^{28}Si and ^{35}Cl(p,α)^{32}S reactions, where there are only a few allowed resonances due to the low Q-values of these reactions. Since the α decay is only possible to the natural parity states (from the smaller Q-value), there are fewer available resonances and approximations using Hauser-Feshbach calculations are not valid.

The most recent direct measurements of the strengths of low-energy resonances in ^{31}P(p,α)^{32}S and ^{35}Cl(p,α)^{36}Ar performed in Toronto and Bochum utilized a proton beam impinging on targets implanted with ^{31}P and ^{35}Cl, respectively [Ili91] [Ili94]. Both of these measurements were hampered by beam-induced proton scattering and background from the ^{11}B(p,3α) reaction from ^{11}B contamination in the tantalum backings of the targets. Due to this background, only upper limits were determined for the resonance strengths except for the resonance at $E_{cm} = 371$ keV in ^{31}P(p,α)^{32}S. The only other resonance strengths in ^{31}P(p,α)^{32}S that have been measured directly are from a study performed in 1963, where the strengths of the $E_{cm} = 600$ keV and 622 keV resonances were determined [Kup63]. No direct measurements of the strengths of resonances in ^{35}Cl(p,α)^{36}Ar for the energy range $E_{cm} \leq 611$ keV have been successful.

The most recent study of low-energy resonances in ^{31}P(p,α)^{28}Si and ^{35}Cl(p,α)^{36}Ar was performed at Notre Dame University using an indirect method [Ros95]. In this study, proton unbound states in ^{32}S and ^{36}Ar were populated using the ^{31}P(^{3}He,d)^{32}S and ^{35}Cl(^{3}He,d)^{36}Ar reactions and alpha particles from the α-decay of ^{32}S and ^{36}Ar were detected in coincidence with deuterons from the (^{3}He,d) reaction [Ros95]. Resonance strengths at $E_{CM} = 371$ and 599 keV in ^{31}P(p,α)^{28}Si were determined, however, only upper limits were able to be extracted for resonance strengths in ^{35}Cl(p,α)^{36}Ar. A summary of resonance strengths and upper limits for the ^{31}P(p,γ)^{32}S, ^{31}P(p,α)^{28}Si,

Table 4.1: Resonance energies and strengths in ^{31}P(p,γ)^{32}S and ^{31}P(p,α)^{28}Si. Values are taken from Ref. [Ros95] except where noted.

E_r (MeV)	J^π	$\omega\gamma_{p,\gamma}$ (eV)	$\omega\gamma_{p,\alpha}$ (eV)
0.195	$(1,2)^-$	$(4.8\pm1.6)\text{x}10^{-7}$	$\leq1.9\text{x}10^{-8}$
0.201	4^+	$\leq3.3\text{x}10^{-9}$	$\leq3.3\text{x}10^{-9}$
0.306	3^+	$\leq3.7\text{x}10^{-5}$	
0.332	2^+	$\leq6.1\text{x}10^{-5}$	$\leq4.2\text{x}10^{-4}$
0.344	1^+	$(4.2\pm0.7)\text{x}10^{-3}$	
0.371	1^-	$(6.0\pm1.2)\text{x}10^{-5}$	$(2.7\pm0.7)\text{x}10^{-3}$
0.391	2^+	$(4.5\pm0.7)\text{x}10^{-4}$	$\leq4.2\text{x}10^{-5}$
0.426	1^+	$(2.5\pm0.4)\text{x}10^{-2}$	
0.524	2^-	$(1.2\pm0.2)\text{x}10^{-1}$	
0.600	2^+	$(1.1\pm0.2)\text{x}10^{-3}$	$(2.5\pm0.4)\text{x}10^{-2}$
0.622	1^-		1.87[a]

[a] Taken from [Kup63]

^{35}Cl(p,γ)^{36}Ar, and ^{35}Cl(p,α)^{36}Ar reactions from previous studies are listed in Tables 4.1 and 4.2.

The ratio of the ^{31}P(p,α)^{28}Si to ^{31}P(p,γ)^{32}S reaction rates is shown in Figure 4.2. At low temperatures, where the ^{31}P(p,γ)^{32}S reaction rate is much stronger than that of ^{31}P(p,α)^{28}Si, weak cycling is expected in the SiP region [Ros95]. The (p,α) reaction on ^{31}P is not expected to significantly compete with the (p,γ) reaction except at higher temperatures (T $\geq$ 0.3 GK), where the E_{cm} = 371 and E_{cm} = 600 keV resonant rate contributions are expected to dominate the (p,α) reaction rate [Ili93] (Figure 4.3).

The lower panel of Figure 4.2 shows the ratio of the ^{35}Cl(p,α)^{32}S reaction rate to the ^{35}Cl(p,γ)^{36}Ar reaction rate. Due to the large uncertainty in the ^{35}Cl(p,α)^{32}S reaction rate from the fact that only upper limits for resonance strengths are established for the energy range $E_{cm} \leq$ 610 keV, the competition between the (p,α) and (p,γ) reactions is uncertain by up to 8 orders of magnitude at lower temperatures. The only (p,α) resonant rate contribution that is expected to compete with that of

Table 4.2: Resonance energies and strengths in ^{35}Cl(p,γ)^{36}Ar and ^{35}Cl(p,α)^{32}S. Values are taken from [Ros95].

E_r (MeV)	J^π	$\omega\gamma_{p,\gamma}$ (eV)	$\omega\gamma_{p,\alpha}$ (eV)
0.049	2^+	$(2.8\pm1.2)\text{x}10^{-24}$	$\leq 2.0\text{x}10^{-25}$
0.165	1^-	$(3.4\pm1.6)\text{x}10^{-10}$	$\leq 4.0\text{x}10^{-11}$
0.302	$(1,2,3^-)$	$(1.5\pm0.5)\text{x}10^{-5}$	$\leq 1.6\text{x}10^{-6}$
0.380		$\leq 3.1\text{x}10^{-5}$	$\leq 6.2\text{x}10^{-6}$
0.402	2^+	$(6.6\pm3.3)\text{x}10^{-5}$	$\leq 1.0\text{x}10^{-3}$
0.416		$\leq 1.3\text{x}10^{-4}$	$\leq 7.8\text{x}10^{-6}$
0.431	$2^+,3^-$	$(1.4\pm0.3)\text{x}10^{-2}$	$\leq 3.2\text{x}10^{-4}$
0.507	$(3^-\text{-}5^-)$	$(1.2\pm0.3)\text{x}10^{-3}$	$\leq 4.5\text{x}10^{-5}$
0.517	2	$(3.2\pm0.7)\text{x}10^{-2}$	
0.559	3^-	$(3.1\pm0.6)\text{x}10^{-2}$	$\leq 7.2\text{x}10^{-3}$
0.610	1^-	$(7.6\pm1.8)\text{x}10^{-4}$	$\leq 1.6\text{x}10^{-1}$

the (p,γ) is from the E_{cm} = 610 keV, where the upper limits of the (p,α) resonance strength is $\approx$ 200 times larger than the measured (p,γ) strength (Figure 4.4).

Though weak reaction cycling has been predicted in both the SiP and SCl mass regions [Ros95], these predictions have been drawn based on indirect studies paired with older measurements (in the case of ^{31}P(p,α)^{28}Si) as well as upper-limit resonance strengths (for ^{35}Cl(p,α)^{32}S). Direct measurements of low-energy resonance strengths in ^{31}P(p,α)^{28}Si and ^{35}Cl(p,α)^{32}S could reduce the uncertainties in these reaction rates and improve the understanding of possible reaction cycling in the SiP and SCl mass regions.

4.2 Experimental Approach

The experimental setup was the same as that described in section 2.2. Low-energy pure beams of stable ^{31}P and ^{35}Cl with intensities of $\approx$1 pnA from the Holifield Radioactive Ion Beam Facility (HRIBF) bombarded hydrogen gas which filled the scattering chamber at pressures of up to 3 Torr. Problems with pumping upstream

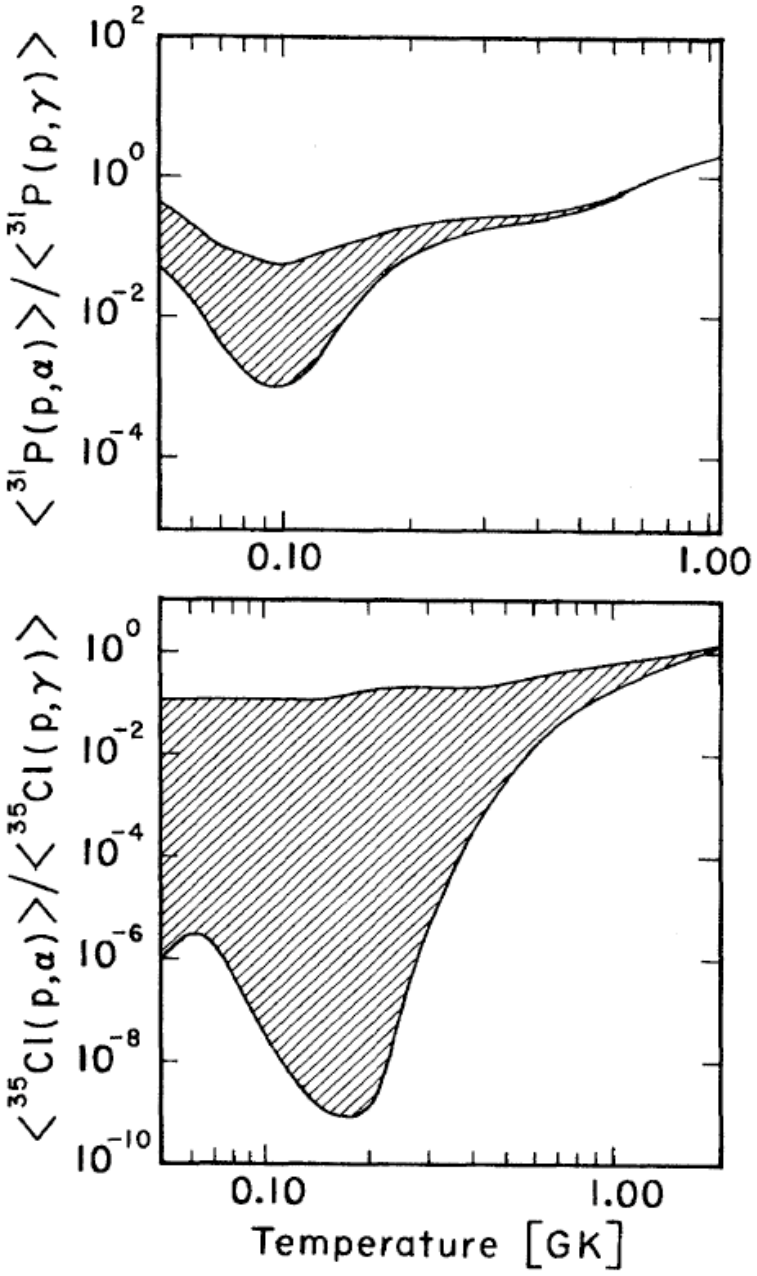

Figure 4.2: The ratio of the ^{31}P(p,α)^{28}Si to ^{31}P(p,γ)^{32}S (upper panel) and ^{35}Cl(p,α)^{32}S to ^{35}Cl(p,γ)^{36}Ar (lower panel) reaction rates. Dashed areas indicate the range of uncertainties in the ^{31}P(p,α)^{28}Si and ^{35}Cl(p,α)^{32}S reaction rates. The upper limits shown take into account the upper limits for (p,α) resonance strengths while the lower limits omit all contributions from unobserved (p,α) or (p,γ) reaction channels. Figure taken from Ross *et al.* [Ros95].

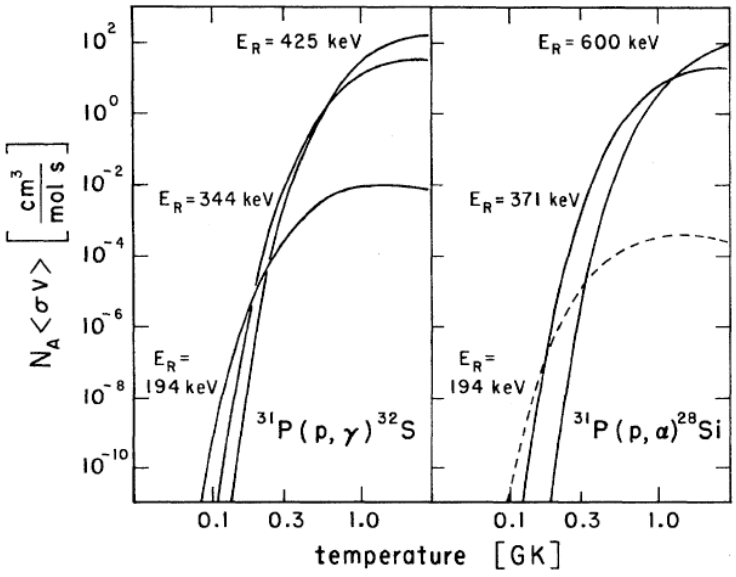

Figure 4.3: Resonant reaction rate contributions in ^{31}P(p,γ)^{32}S and ^{31}P(p,α)^{28}Si. Figure taken from Ross *et al.* [Ros95].

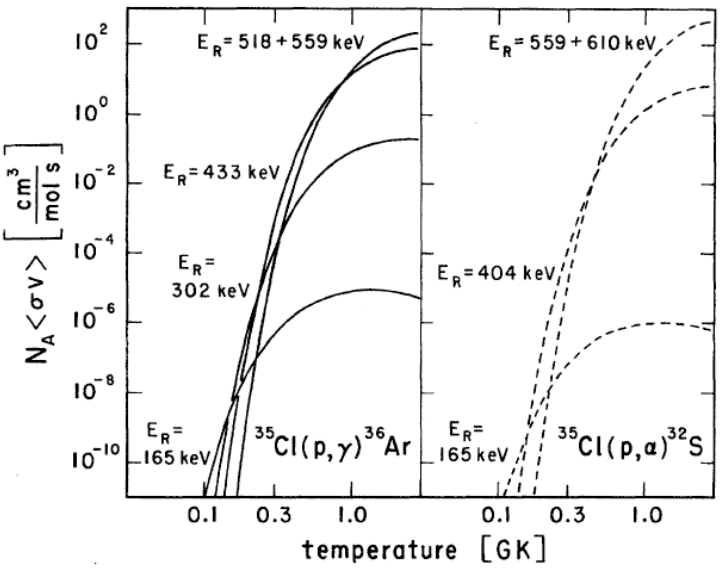

Figure 4.4: Resonant reaction rate contributions in ^{35}Cl(p,γ)^{36}Ar and ^{35}Cl(p,α)^{32}S. Figure taken from Ross *et al.* [Ros95].

of the gas target prevented running at higher pressures inside the target while still maintaining the required beamline pressure.

The α particles and heavy recoils were detected in coincidence within the gas-filled chamber by the SIDAR silicon detector array and the S1 detector, respectively (section 2.4). The SIDAR array was located 115 mm from the entrance of the chamber, while the S1 detector was positioned 208 mm downstream of SIDAR. Both detectors were individually calibrated using a ^{244}Cm source. Plots of the energy detected in the S1 detector versus the energy detected in the SIDAR detector gated on the time between events in the two detectors were used to identify ^{1}H(^{31}P,α)^{28}Si and ^{1}H(^{35}Cl,α)^{32}S events.

The segmentation of SIDAR and the energy of the emitted α particle were used to determine the reaction vertex for ^{1}H(^{31}P,α)^{28}Si and ^{1}H(^{35}Cl,α)^{32}S events (section 2.5). Small corrections to the measured α energy were made for the energy loss of the particle as it traveled through the hydrogen gas and the energy loss as the particle traveled through the dead layer of SIDAR as described in section 2.5.

The integrated beam current at each energy was determined by normalizing to ^{12}C(^{31}P,^{12}C)^{31}P and ^{12}C(^{35}Cl,^{12}C)^{35}Cl elastic scattering measured simultaneously with the ^{1}H(^{31}P,α)^{28}Si and ^{1}H(^{35}Cl,α)^{32}S reactions using a carbon foil and two single-collimated surface barrier detectors (monitor detectors) (section 2.4). Using a calibrated ^{244}Cm α-source mounted at the same position as the ^{12}C foil, the solid angle subtended by each monitor detector were determined to be 1.62 and 1.89 msr at $\theta_{lab} = 38.3^{o}$ and 35.7^{o} respectively. An average of the integrated beam current as determined by the two monitor detectors was used for normalization.

4.3 Data and Results

4.3.1 The 371 keV resonance in ^{31}P(p,α)^{28}Si

In order to determine the strength of the 371 keV resonance in ^{31}P(p,α)^{28}Si, data was taken at incident ^{31}P bombarding energies of E_{lab} = 11.894, 11.864, and 11.824 MeV. An off-resonance measurement at E_{lab} = 11.7 MeV was taken in order to subtract possible background from off-resonant ^{31}P(p,α)^{28}Si yield from on-resonance (p,α) yield.

A plot of the energy of particles detected in the SIDAR array versus the energy of coincident particles detected in the S1 detector is shown in Figure 4.5 for energies of E_{lab} = 11.864 MeV(on-resonance) and E_{lab} = 11.7 MeV (off-resonance) with a total integrated incident beam ratio of $\approx$ 1.4:1. Due to the large amount of beam scattering off the entrance aperture (section 2.7), it was extremely difficult to distinguish ^{1}H(^{31}P,α)^{28}Si events from the background scattering at higher energies in the S1 detector. Furthermore, non-resonant (p,α) background subtracted using the off-resonant E_{lab} = 11.7 MeV measurement (scaled for total incident beam) left the on-resonant energies with insufficient yield to determine a resonance strength. Therefore, no improvement on the strength of the 371 keV resonance over that of Ross *et al.* [Ros95] could be made in this study.

4.3.2 The 599 keV resonance in ^{31}P(p,α)^{28}Si

Data was taken at incident ^{31}P bombarding energies of E_{lab} = 19.04, 19.07, 19.1 and 19.12 MeV at H_2 pressures of 3 Torr in order to measure the strength of the 599 keV resonance in ^{31}P(p,α)^{28}Si. A measurement at E_{lab} = 19.01 MeV was also taken for purposes of background subtraction.

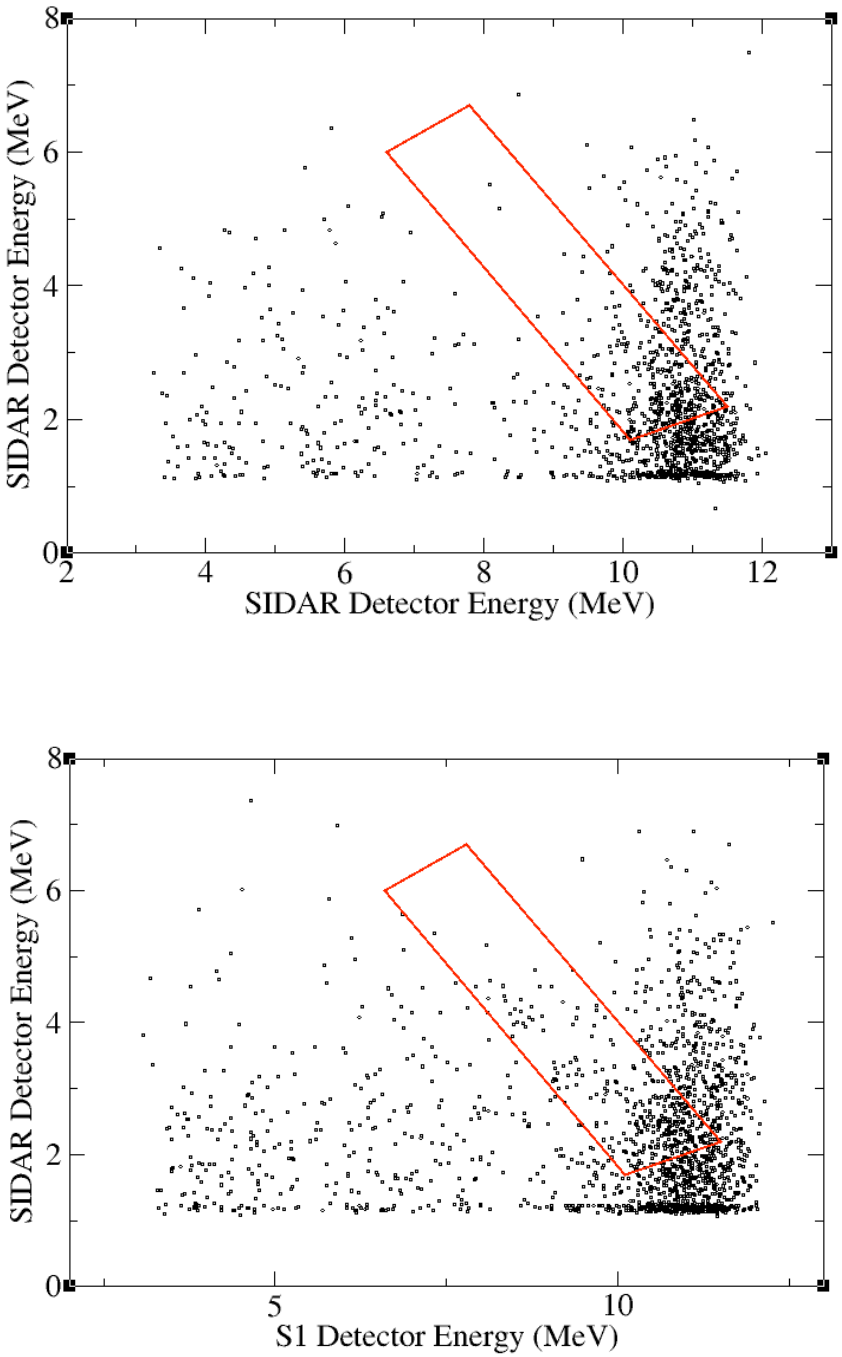

Figure 4.5: The energy of particles detected in SIDAR plotted against the energy of coincident particles in the S1 detector for an incident ^{31}P energy of 11.7 MeV (top) (off-resonance) and 11.864 MeV (bottom) (on-resonance). The drawn box is where (p,α) events are expected to fall.

Figure 4.6 shows plots of the energy of particles detected in the SIDAR detector versus the energy of coincident particles detected in the S1 detector for incident ^{31}P energies of 19.01 MeV (off-resonance) and 19.07 MeV (on-resonance) with both plots gated on their respective peaks in the TAC spectrum (Figure 4.7). The ratio of the incident number of ^{31}P particles for the two energies depicted in Figure 4.6 is $\approx$ 8:1. The number of counts in the gate for the off-resonant energy measurement was scaled for the total incident beam and used for background subtraction at each on-resonance energy. The remaining counts in the gate drawn in Figure 4.6 after background subtraction determined the ^{1}H(^{31}P,α)^{28}Si yield.

The reaction vertex at each energy was determined using the segmentation of the SIDAR array and the energies of the emitted α particles from the (p,α) reaction as described in section 2.5. A plot of ^{1}H(^{31}P,α)^{28}Si counts versus reaction vertex (measured from the plane of the SIDAR array) for events that fall within the within the gate in the TAC spectrum (Figure 4.7 as well as the kinematics gate drawn in Figure 4.6), is show in Figure 4.8. Due to the low ^{1}H(^{31}P,α)^{28}Si yields for the on-resonance energies, the uncertainty in the reaction vertex ($\pm$7 mm from a Gaussian fit to each data set), upon which the solid angle directly depends, dominates the overall uncertainty in the resonance strength.

A strong angular distribution for the emitted α particle of:

$$W(\theta_\alpha) = 1 + 1.22P_2cos(\theta_\alpha) + 1.32P_4cos(\theta_\alpha) \tag{4.1}$$

where P$_n$cos(θ) is the nth-order Legendre polynomial and θ_α is the center-of-mass angle of the emitted α particle was reported by Kuperus *et al.* [Kup63] for the 599 keV resonance and increases the effective solid angle by up to 20% over that of an isotropic distribution. Due to the low ^{1}H(^{31}P,α)^{28}Si yield in this study, this angular

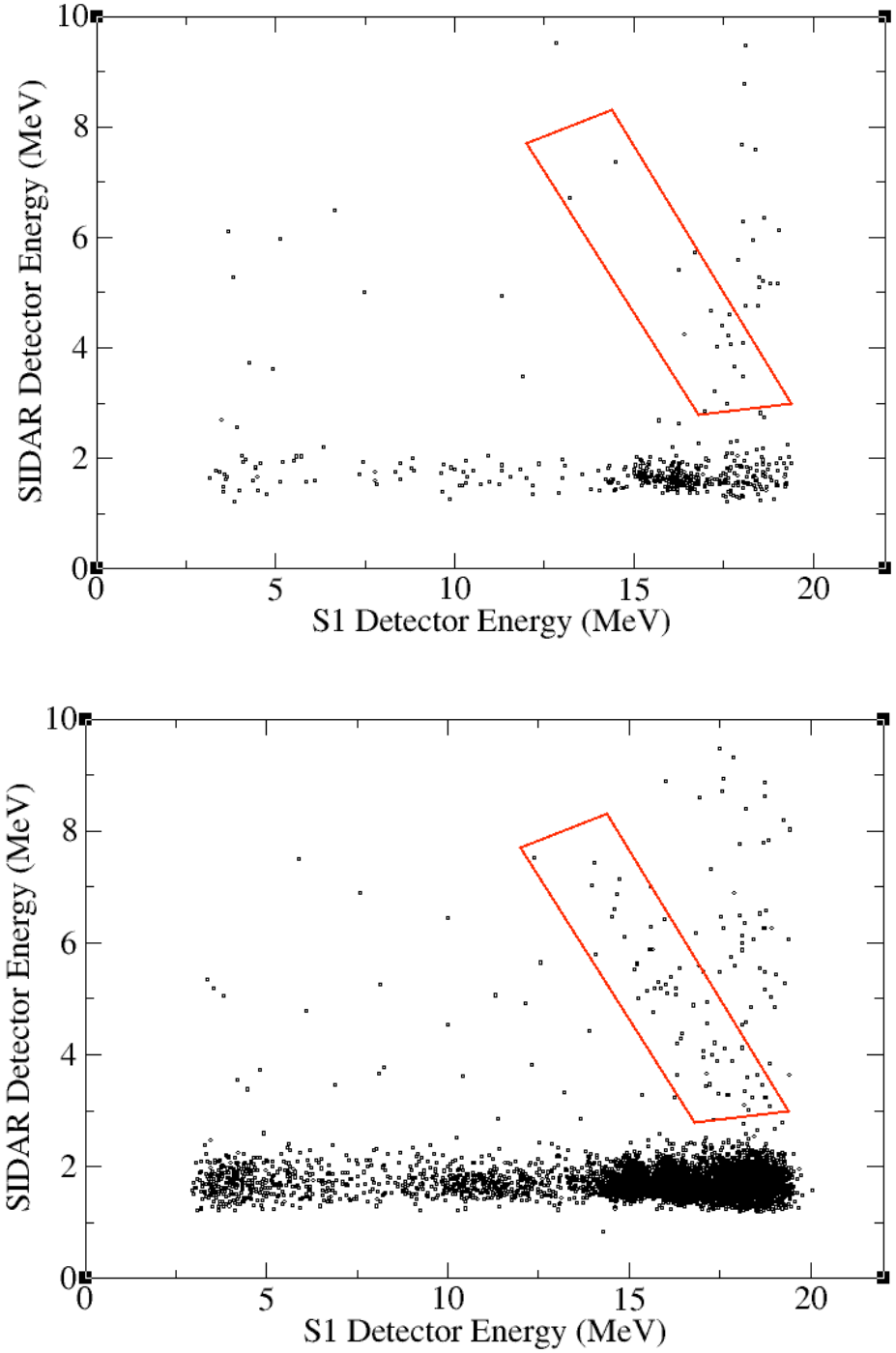

Figure 4.6: The energy of particles detected in SIDAR plotted against the energy of coincident particles in the S1 detector for incident ^{31}P energies of 19.01 MeV (top) (off-resonance) and 19.07 MeV (bottom) (on-resonance). The drawn box is where (p,α) events are expected to fall.

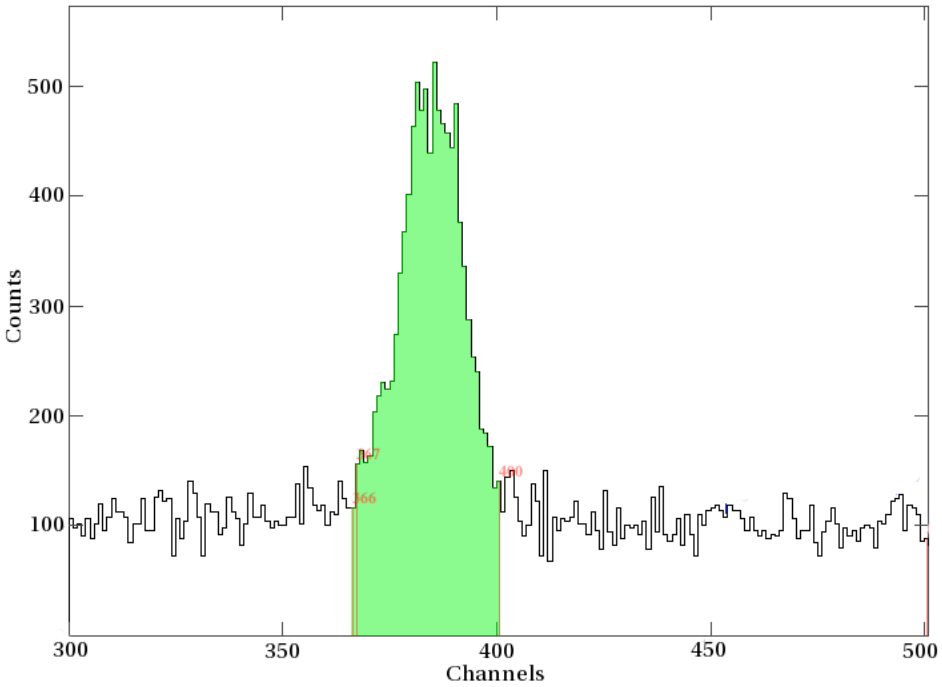

Figure 4.7: TAC spectrum for the E_{lab} = 19.07 MeV measurement. The shaded region indicates the region in which the events in Figure 4.6 fall.

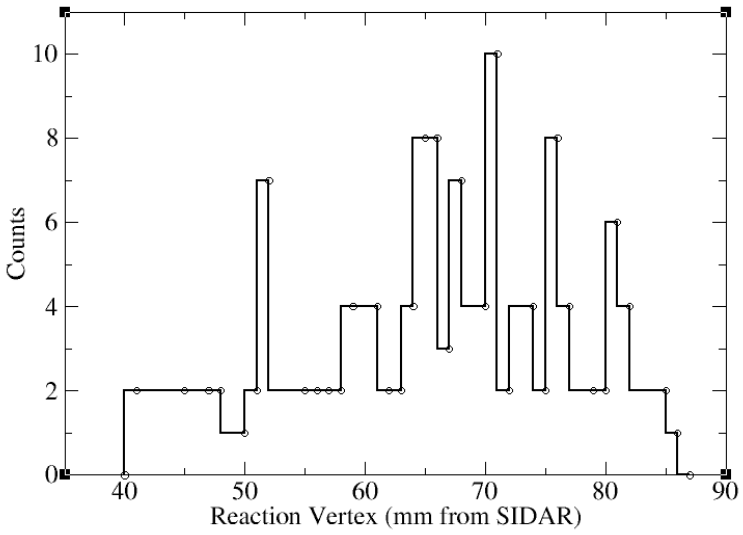

Figure 4.8: The distribution of ^{1}H(^{31}P,α)^{28}Si events as a function of the distance from the plane of SIDAR (mm) at an incident ^{31}P energy of E_{lab} = 19.07 MeV.

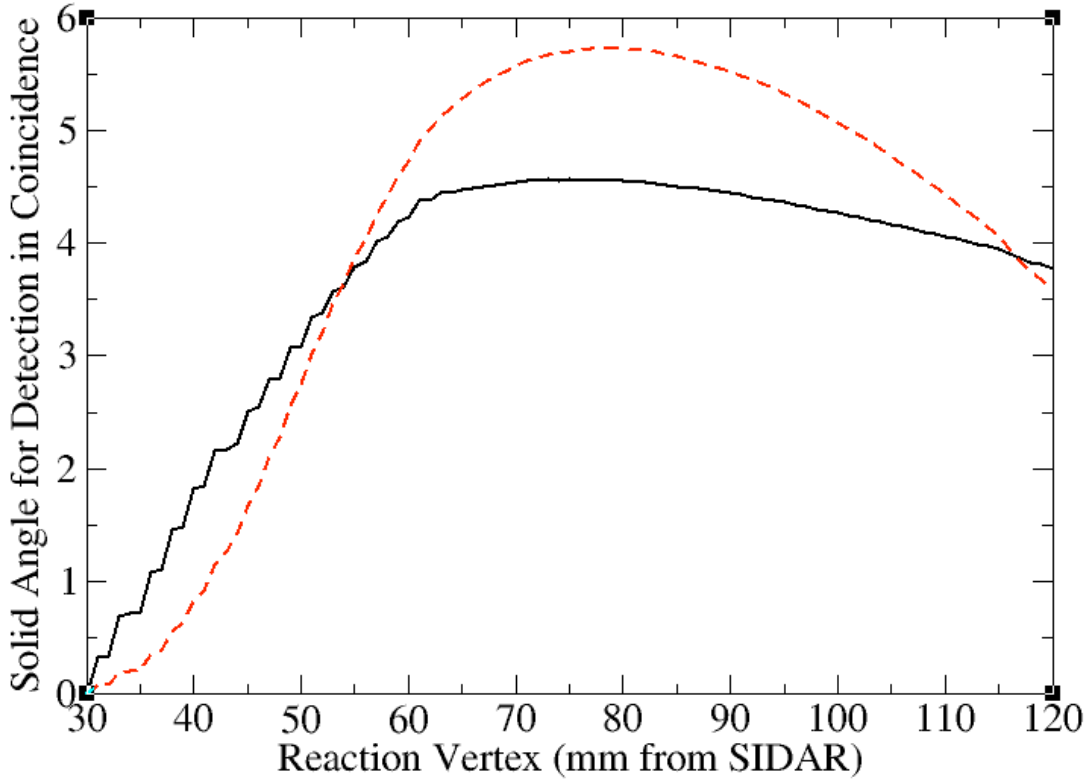

Figure 4.9: Total solid angle (center-of-mass frame) for detection of α particles in coincidence with detection of the ^{28}Si recoil versus the reaction vertex (measured from the plane of SIDAR) for the E_{cm} = 599 keV resonance in ^{31}P(p,α)^{28}Si. The solid (black curve) uses an isotropic angular distribution while the dashed (red curve) uses the distribution from [Kup63].

distribution could not be confirmed. Figure 4.9 shows the solid angle for detection of the α particle in coincidence with the ^{28}Si recoil as a function of the distance from the plane of the SIDAR array using both angular distributions. The rapid change in the solid angle using the distribution given by equation 4.1 has a profound effect on the uncertainties in the solid angle, increasing the error from $\approx$ 20% using an isotropic distribution to $\approx$ 50%.

A weighted average of the resonance strengths as determined from each on-resonant beam energy, which incorporated the uncertainties at each energy was used to determine the overall resonance strength. The uncertainties that were common to each energy are as follows: 1% in the uncertainty in the stopping power of ^{31}P ions in hydrogen gas determined from a calculation using the ORNL stopping power code STOPIT and the measurements at E_{CM} = 622 keV (section 4.3.3), 3% uncertainty in the strength of the ^{244}Cm α source used for determining the solid angle of the monitor detectors (section 2.4), and the thickness of the carbon foil (6% from the uncertainty in stopping power for α particles in carbon). A resonance strength of $\omega\gamma_{p,\alpha} = (1.6 \pm 0.4)*10^{-2}$ eV (using an isotropic angular distribution) and $\omega\gamma_{p,\alpha} = (1.3 \pm 0.9)*10^{-2}$ eV (using the angular distribution given by equation 4.1) was determined, the latter of which agrees with the findings of Ross *et al.* [Ros95] due to the high uncertainty. It is unknown if the present resonance strength agrees with that of Kuperus *et al.* [Kup63] ($2.3*10^{-2}$ eV) since no uncertainty was reported for that study. A summary of the previous and present resonance strengths is given in Table 4.3.

Table 4.3: Results of previous and present studies of the 599 keV resonance in ^{31}P(p,α)^{28}Si

	Ross *et al.*[a]	Kuperus *et al.*[b]	Present Work	
$\omega\gamma_{p,\alpha}$ (10^{-2} eV)	(2.5 ± 0.4)	2.3	(1.6 ± 0.4)[c]	(1.3 ± 0.9)[d]

[a] Ref. [Ros95]
[b] Ref. [Kup63]
[c] Using an isotropic angular distribution
[d] Using the angular distribution from [Kup63]

4.3.3 The 622 keV resonance in ^{31}P(p,α)^{28}Si

Data was taken at incident ^{31}P bombarding energies of E_{lab} = 19.78, 19.80, 19.845 and 19.875 MeV at H_2 pressures of 3 Torr in order to measure the strength of the 622 keV resonance in ^{31}P(p,α)^{28}Si. Data was also taken at an energy of 19.73 MeV for purposes of background subtraction.

Figure 4.10 shows plots of the energy of particles detected in the SIDAR detector versus the energy of coincident particles detected in the S1 detector for incident ^{31}P energies of 19.73 MeV (off-resonance) and 19.78 MeV (on-resonance) with both plots gated on their respective peaks in the TAC spectrum. The ratio of the incident number of ^{31}P particles for the two energies depicted in Figure 4.10 is $\approx$ 5:1. Due to the large strength of this resonance and the low background present in the data, the ^{1}H(^{31}P,α)^{28}Si events were easily identified by gating on the peak in the TAC spectrum.

The segmentation of SIDAR and the energy of the emitted α particle were used to determine the reaction vertex for ^{1}H(^{31}P,α)^{31}P events (section 2.5). In Figure 4.11, the reaction yield is plotted versus distance from the reaction vertex to the plane of SIDAR, z, for bombarding energies of E_{lab} = 19.78 and 19.80 MeV. Small corrections to the measured α energy were made for the energy loss as described in section 2.5 (equation 2.1).

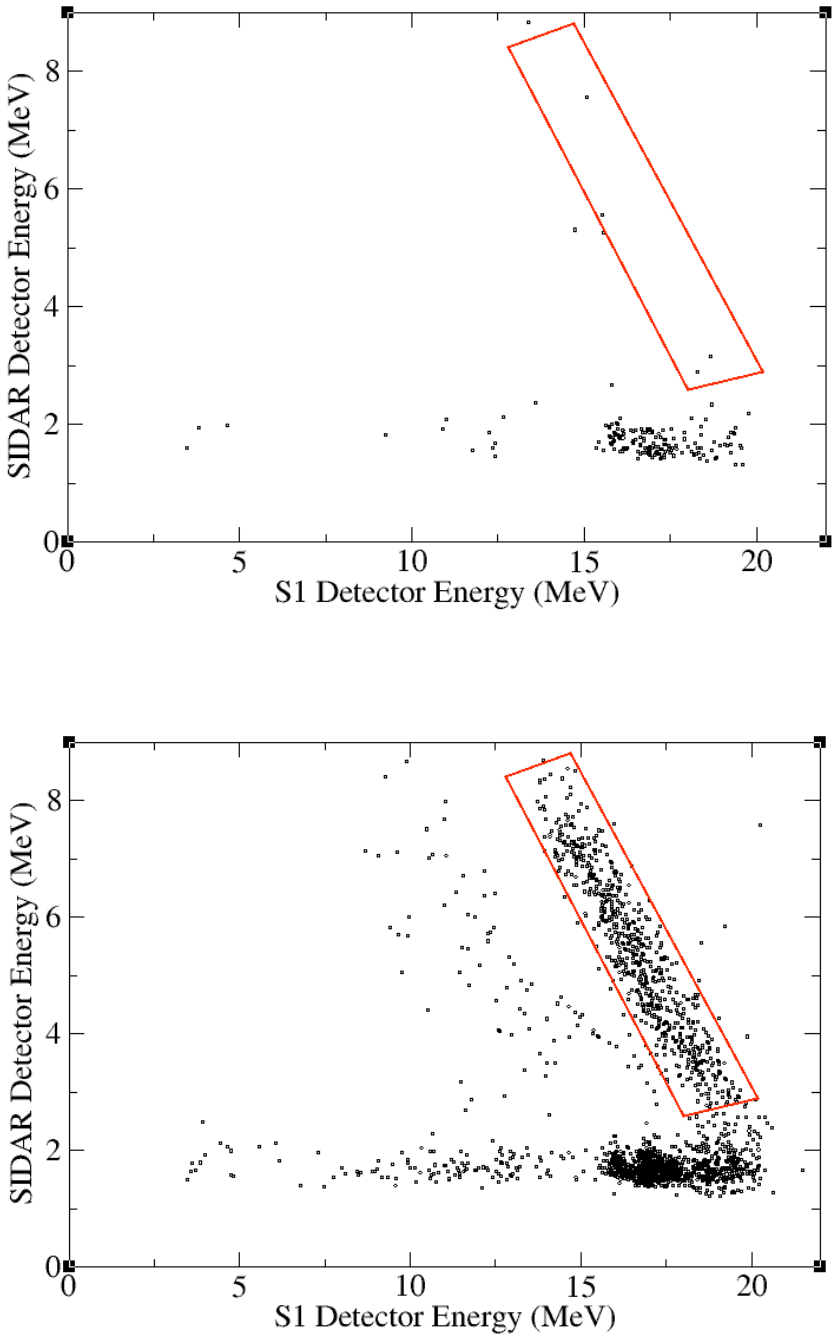

Figure 4.10: The energy of particles detected in SIDAR plotted against the energy of coincident particles in the S1 detector for incident ^{31}P energies of 19.73 MeV (top) (off-resonance) and 19.78 MeV (bottom) (on-resonance). The drawn box is where (p,α) events are expected to fall.

An angular distribution for the emitted α particle of:

$$W(\theta_\alpha) = 1 + 0.62 P_2 cos(\theta_\alpha) \tag{4.2}$$

where $P_2\cos(\theta)$ in the 2^{nd}-order Legendre polynomial and θ_α is the center-of-mass angle of the emitted α particle was reported by Kuperus *et al.* [Kup63] for the 622 keV resonance and increases the solid angle up to 8% over that of an isotropic distribution. In Figure 4.12, the solid angle for detection of the α particle and ^{28}Si recoil in coincidence is plotted as a function of the distance from the plane of SIDAR using the angular distribution of equation 4.2 as well as an isotropic distribution. Though the angular distribution of Kuperus *et al.* gives a slightly higher solid angle (and thus a slightly lower resonance energy), it has little effect on the overall uncertainty since the solid angle remains fairly constant over the range of vertices in this study.

The reaction vertex was also determined using the ^{28}Si recoils and the segmentation of the S1 detector (section 2.5). In Figure 4.13, the reaction vertex is plotted against the incident ^{31}P energy as determined from the S1 detector (using the ^{28}Si recoils) (top panel) and the SIDAR detector (using the detected α particles) (bottom panel). A least-squares fit to the S1 detector data gives a stopping power of ϵ = 108 x 10^{-15} eV cm^2 while the stopping power extracted from the fit to the SIDAR data gives $\epsilon = 103$ x 10^{-15} eV cm^2. Table 4.4 compares the stopping power value extracted from these fits to the values obtained by the semi-empirical model SRIM [Zie03] and the ORNL stopping power code STOPIT. The values for the stopping power obtained in the present study and from STOPIT differ from that of SRIM by $\approx$ 33%. Also shown in Figure 4.13 are fits where the slope has been fixed to correspond to the stopping power from SRIM and the intercept is varied in order to minimize the χ^2. Since both data sets are better fit using the stopping power that agrees with STOPIT,

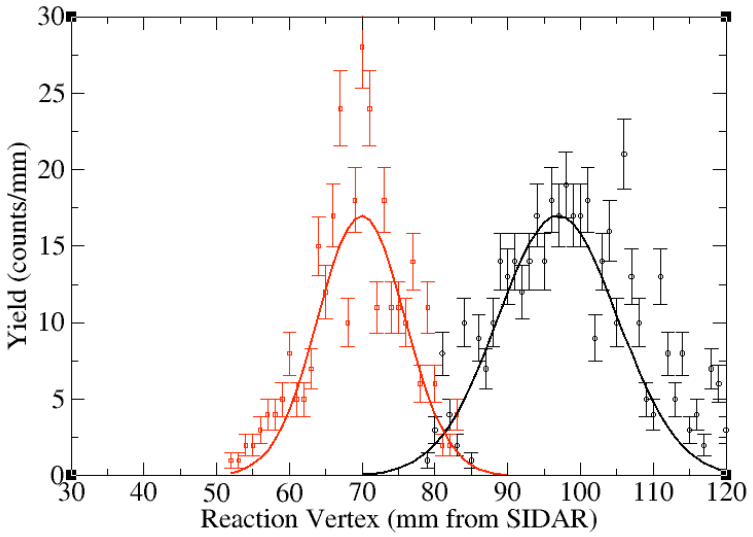

Figure 4.11: The distribution of ^{1}H(^{31}P,α)^{28}Si events as a function of the distance (z) from the plane of SIDAR (mm) at incident ^{31}P energies of 19.78 MeV (black circles) and 19.80 MeV (red squares). The black (red) curve is a gaussian fit used to determine the centroid.

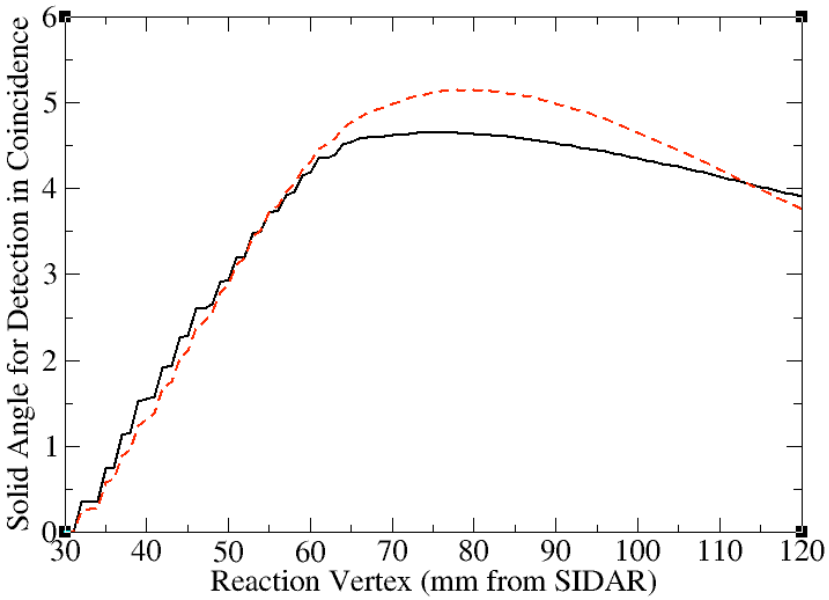

Figure 4.12: Total solid angle (center-of-mass frame) for detection of α particles in coincidence with detection of the ^{28}Si recoil versus the reaction vertex (measured from the plane of SIDAR) for the E_{CM} = 622 keV resonance in ^{31}P(p,α)^{28}Si. The solid (black curve) uses an isotropic angular distribution while the dashed (red curve) uses the distribution from [Kup63].

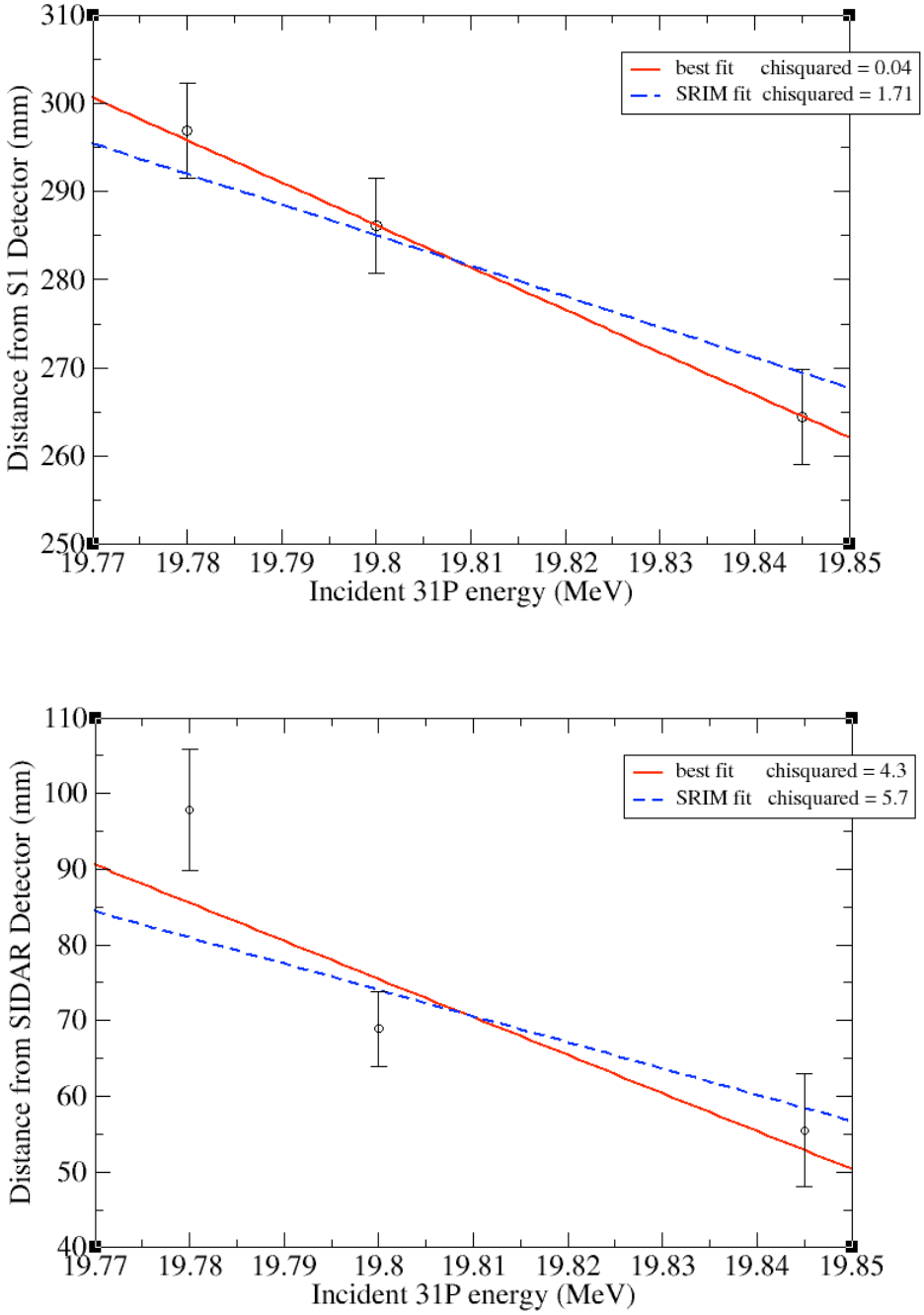

Figure 4.13: The reaction vertex plotted against the distance to the plane of the S1 detector (top) and SIDAR (bottom). The red (solid) lines represent the best least-squares fits to the data while the blue (dashed) lines are fits using a slope from the stopping power given by SRIM [Zie03] where the intercept was varied in order to minimize χ^2.

Table 4.4: Results for the stopping power for phosphorous in hydrogen gas at 641 keV/u compared to the semi-empirical model SRIM 2003 [Zie03] and the ORNL stopping power code STOPIT.

	ϵ (10^{-15} eV cm^2)
Present Work	106 ± 1
SRIM 2003 [Zie03]	150
STOPIT	104

no previous measurement of the stopping power of ^{31}P ions in hydrogen gas exists around the energy range of 641 keV/u, and the stopping power given by SRIM is an extrapolation using only 7 data points (compared with 138 points in ^{17}O + p), the average stopping power obtained from fits to the S1 and SIDAR detector data was used in determining the strength of both the 599 keV and 622 keV resonances. The largest source of uncertainty in the stopping power arises from the uncertainty in the gas pressure inside the target chamber ($\approx 1\%$).

The calculated resonance strength at each energy agreed to within 10% when using an isotropic angular distribution and within 2% when using the angular distribution in equation 4.2. A weighted average using each distribution which incorporates the uncertainty in the strength at each energy gives $\omega\gamma_{p,\alpha} = (0.76 \pm 0.09)$ eV and (0.7 ± 0.1) eV using the isotropic angular distribution and the angular distribution given by equation 4.2, respectively. Both strengths are ≈ 2.5 times smaller than the measured strength of Kuperus *et al.* ($\omega\gamma_{p,\alpha} = 1.8$ eV with no uncertainty reported).

4.3.4 The 559 keV resonance in ^{35}Cl(p,α)^{32}S

In order to determine the strength of the 559 keV resonance in ^{35}Cl(p,α)^{32}S, data was taken at incident ^{35}Cl bombarding energies of E_{lab} = 19.98, 20.01, and 20.04 MeV. An off-resonance measurement at E_{lab} = 21.70 MeV was taken in order to subtract possible off-resonant ^{35}Cl(p,α)^{32}S yield from on-resonance (p,α) yield.

A plot of the energy of particles detected in the SIDAR array versus the energy of coincident particles detected in the S1 detector is shown in Figure 4.14 for energies of E_{lab} = 20.01 MeV (on-resonance) and E_{lab} = 21.70 MeV (off-resonance) with a total incident beam ratio of $\approx$ 9.7:1. Due to the large amount of scattering off the entrance aperture (section 2.7), it was extremely difficult to distinguish ^{1}H(^{35}Cl,α)^{32}S events from the background scattering at higher energies in the S1 detector. Furthermore, non-resonant (p,α) background subtracted using the off-resonant E_{lab} = 21.70 MeV measurement (scaled for total incident beam) left the on-resonant energies with insufficient yield to determine a resonance strength. Therefore, no improvement on the strength of the 559 keV resonance over that of the upper limits set by Ross *et al.* [Ros95] could be made in this study.

4.3.5 The 611 keV resonance in ^{35}Cl(p,α)^{31}S

Data was taken at incident "on-resonant" ^{35}Cl bombarding energies of E_{lab} = 21.83, 21.85, 21.87 and 21.90 MeV and "off-resonant" energy E_{lab} = 21.70 MeV at H_2 pressures of 3 Torr in order to measure the strength of the 611 keV resonance in ^{35}Cl(p,α)^{31}S.

Figure 4.15 shows a plot of the energy of particles detected in the SIDAR detector versus the energy of coincident particles detected in the S1 detector for incident ^{35}Cl energy of 21.87 MeV (on-resonance). The ratio of the incident number of ^{35}Cl particles for the 21.87 MeV measurement and the off-resonance 21.7 MeV measurement depicted in Figure 4.14 was $\approx$ 8:1. The number of counts in the gate for the off-resonant energy measurement was scaled for the total incident beam and used for background subtraction at each on-resonance energy. The remaining counts in the

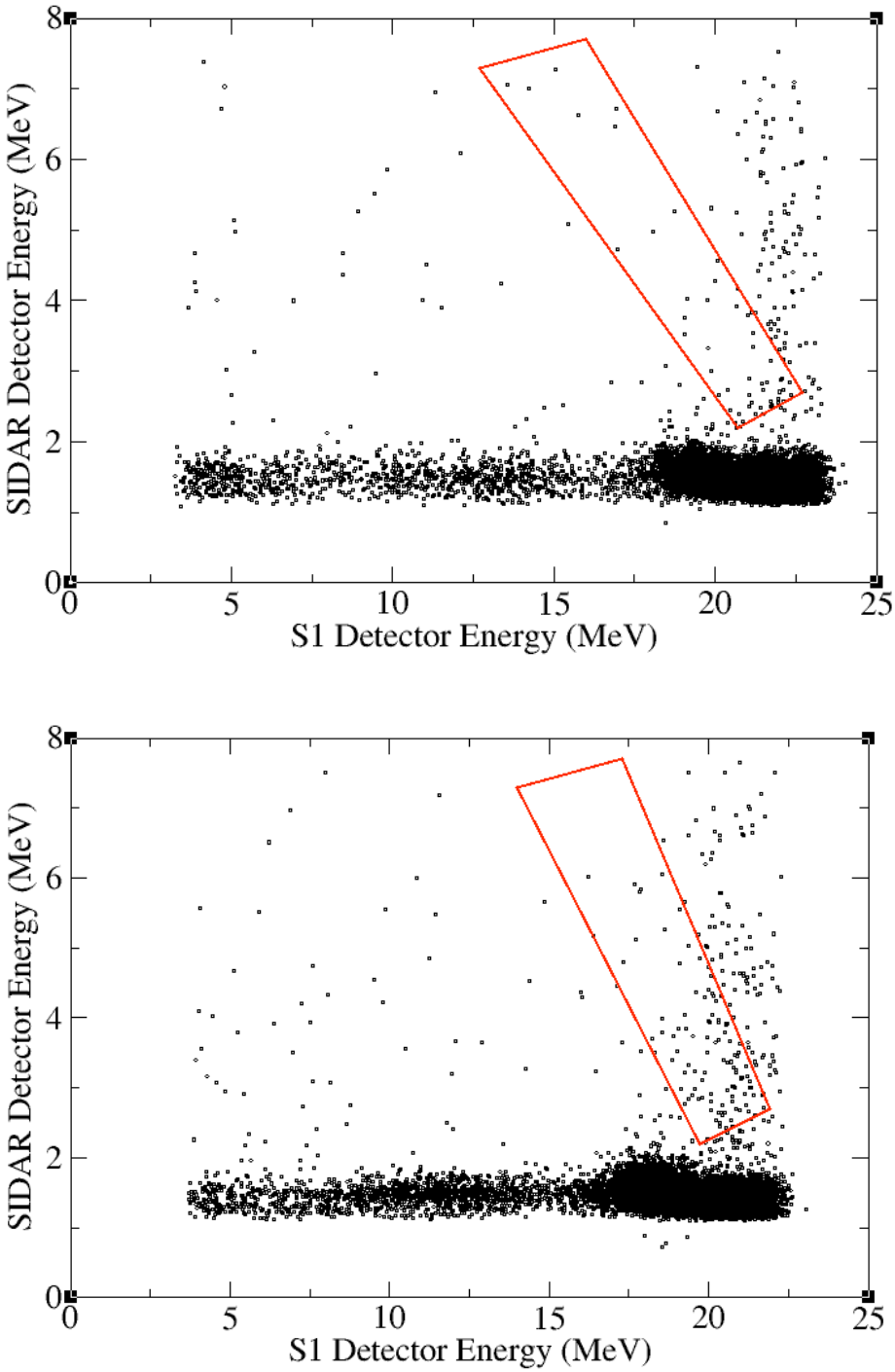

Figure 4.14: The energy of particles detected in SIDAR plotted against the energy of coincident particles in the S1 detector for an incident ^{35}Cl energy of 21.70 MeV (top) (off-resonance) and 20.01 MeV (bottom) (on-resonance). The drawn box is where (p,α) events are expected to fall.

gate drawn in Figure 4.14 after background subtraction determined the ^{1}H(^{35}Cl,α)^{31}S yield at each energy.

In Figure 4.16, the distribtion of the ^{1}H(^{35}Cl,α)^{31}S events is plotted as a function of the distance from the plane of SIDAR for an incident beam energy of E_{lab} = 21.87 MeV. Due to the low ^{1}H(^{31}P,α)^{28}Si yields for the on-resonance energies, the uncertainty in the reaction vertex (taken to be $\pm$ 7 mm), upon which the solid angle directly depends, dominates the overall uncertainty in the resonance strength.

The total solid angle for detecting the α particle and ^{31}S in coincidence is shown as a function of the distance from SIDAR in Figure 4.17. Since this is the first time this resonance has been seen, directly or indirectly, and the ^{1}H(^{35}Cl,α)^{31}S yield was too low to determine an angular distribution, an isotropic distribution was assumed.

A weighted average of the resonance strengths as determined from each on-resonant beam energy which incorporated the uncertainties at each energy was used to determine the overall resonance strength. The uncertainties that were common to each energy are as follows: 5% in the uncertainty in the stopping power of ^{35}Cl ions in hydrogen gas determined from a calculation using the ORNL stopping power code STOPIT and SRIM [Zie03], 3% uncertainty in the strength of the ^{244}Cm α source used for determining the solid angle of the monitor detectors (section 2.4) and the thickness of the carbon foil (6% from the uncertainty in stopping power for α particles in carbon). A resonance strength of $\omega\gamma_{p,\alpha}$ = (1.8 $\pm$ 0.2)*10^{-2} eV was determined, a factor of 10 less than the previously set upper limits from Ross *et al.* [Ros95] for this resonance (Table 4.2).

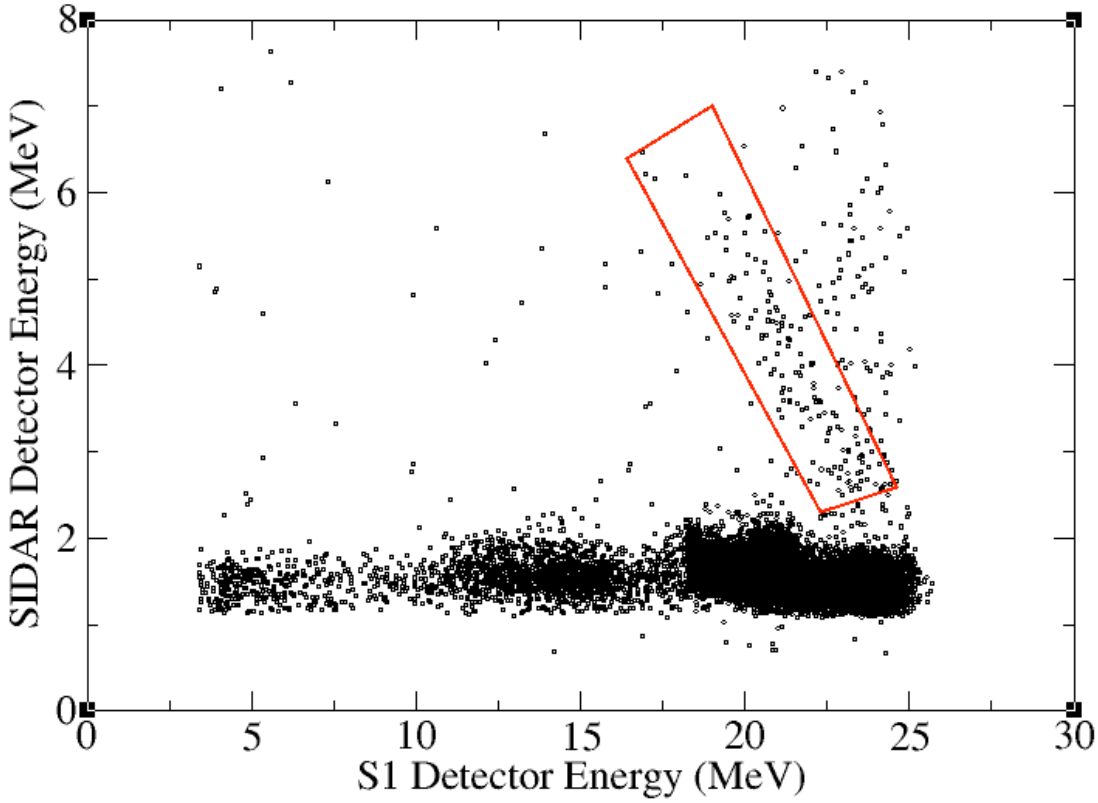

Figure 4.15: The energy of particles detected in SIDAR plotted against the energy of coincident particles in the S1 detector for an incident ^{35}Cl energy of 21.87 MeV (on-resonance). The drawn box is where (p,α) events are expected to fall.

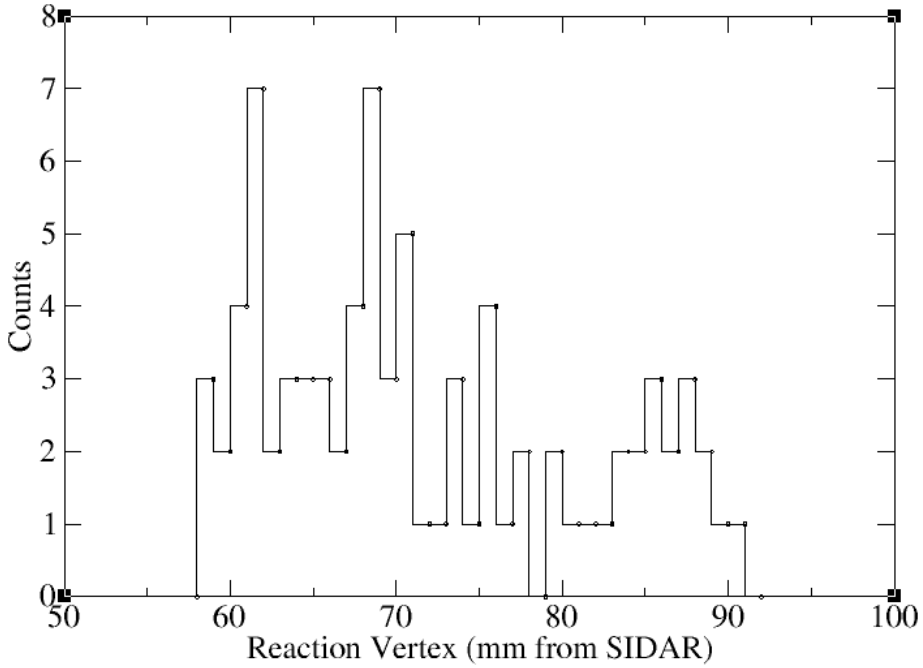

Figure 4.16: The distribution of ^{1}H(^{35}Cl,α)^{31}S events as a function of the distance from the plane of SIDAR (mm) at an incident ^{35}Cl energy of E_{lab} = 21.87 MeV.

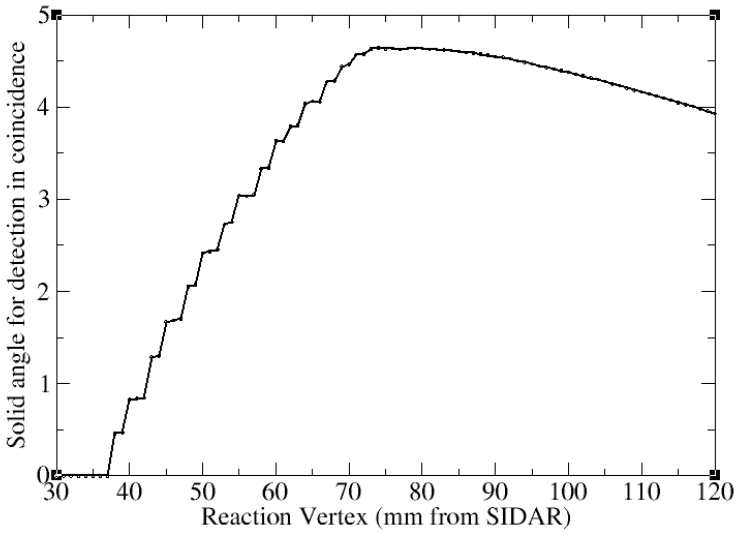

Figure 4.17: Total solid angle (center-of-mass frame) for detection of α particles in coincidence with detection of the ^{31}S recoil versus the reaction vertex (measured from the plane of SIDAR) for the E_{cm} = 611 keV resonance in ^{35}Cl(p,α)^{31}S.

4.4 Astrophysical Implications

4.4.1 The ^{31}P(p,α)^{28}Si reaction rate

The ^{31}P(p,α)^{28}Si reaction rate is dominated by narrow resonances in the temperature range $T_9 \leq 0.1$ [Ili93]. Since the 599 and 622 keV resonances are not expected to contribute to the reaction rate below this temperature range, the overall contributions to the astrophysical reaction rate due to the new strengths measured in this study can be expressed in the narrow, isolated resonance approximation as:

$$N_A < \sigma\nu >_{599keV} \approx 2557 T_9^{-3/2} exp(-6.951/T_9) \tag{4.3}$$

for the 599 keV resonance, and:

$$N_A < \sigma\nu >_{622keV} \approx 121463 T_9^{-3/2} exp(-7.218/T_9) \tag{4.4}$$

for the 622 keV resonance where T_9 is the temperature in units of 10^9 K. The resonant (p,α) and (p,γ) reaction rates at each temperature were determined by summing the individual contributions from each resonance in the energy range E_{CM} = 195-1963 keV, where the properties of each resonance were taken from Ross *et al.* [Ros95] where available and otherwise from the energy levels compilation by Endt [End90].

The ratio of the ^{31}P(p,α)^{28}Si and ^{31}P(p,γ)^{32}S resonant reaction rates is shown in Figure 4.18. The upper limits for both the previous and present studies take into account upper limits of resonance strengths of previously undetected resonances (see Table 4.1), while the lower limits omit the contributions of these resonances. While the previous studies of Ross and Iliadis [Ros95] [Ili93] had the ^{31}P(p,α)^{28}Si reaction starting to compete with the ^{31}P(p,γ)^{32}S reaction around a temperature of $T_9 \sim 0.7$,

the decreased resonance strengths of the 599 keV and 622 keV resonances in this study lower the ^{31}P(p,α)^{28}Si rate so that this competition does not occur until higher temperatures ($T_9 \geq 0.9$) with the new lower limit a factor of ≈2 below the previous lower limit in the $0.6 \leq T_9 \leq 1$ temperature range. Since no improvement on the strength of the 371 keV resonance could be made, cycling at lower temperatures in the SiP region is still uncertain.

4.4.2 The ^{35}Cl(p,α)^{32}S reaction rate

The resonant contribution of the newly-measured strength of the 611 keV resonance to the ^{35}Cl(p,α)^{32}S astrophysical reaction rate can be expressed in the narrow, isolated resonance approximation as:.

$$N_A < \sigma\nu >_{611keV} \approx 2861 T_9^{-3/2} exp(-7.091/T_9) \tag{4.5}$$

The resonant (p,α) and (p,γ) reaction rates at each temperature were determined by summing the individual contributions from each resonance in the energy range E_{CM} = 49-2344 keV, where the properties of each resonance were taken from Ross et al. [Ros95] where available and otherwise from the energy levels compilation by Endt [End90].

The ratio of the ^{35}Cl(p,α)^{32}S and ^{35}Cl(p,γ)^{36}Ar resonant reaction rates are shown in Figure 4.19. The upper limits for both the previous and present studies take into account upper limits of resonance strengths of previously undetected resonances (see Table 4.2), while the lower limits omit the contributions of these resonances.

At lower temperatures ($T_9 \leq 0.4$), the new strength of the 611 keV resonance greatly improves upon the previous lower limits of the resonant reaction rate (up to

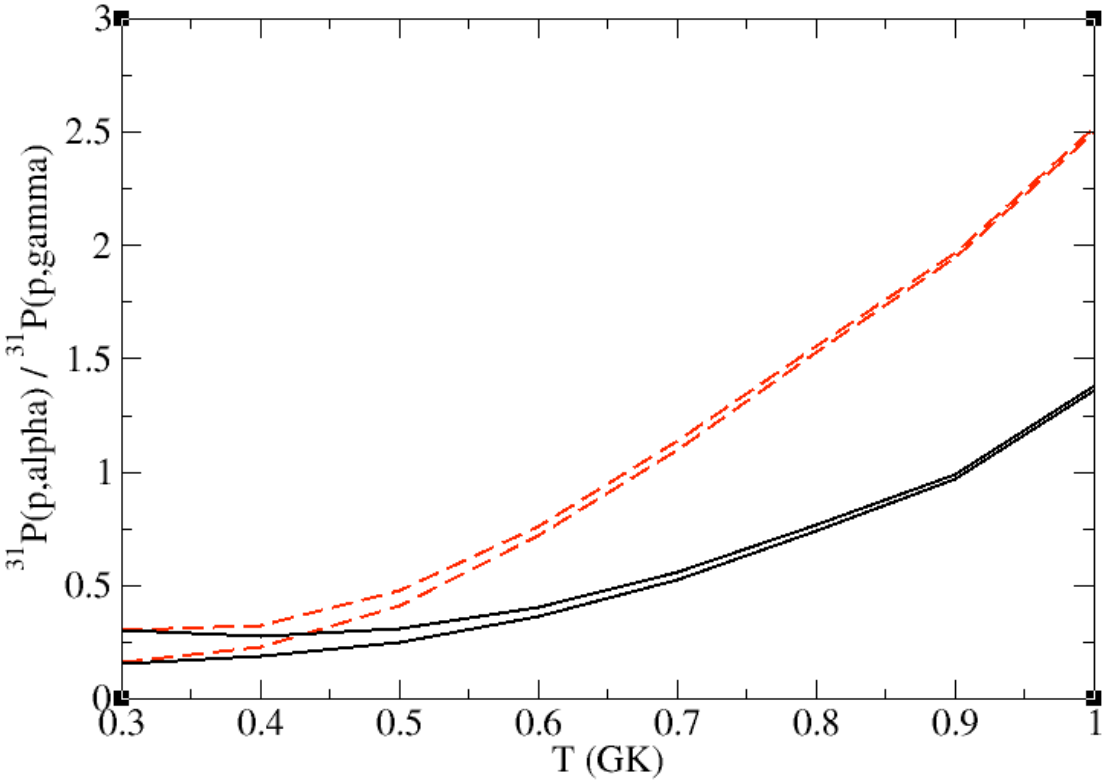

Figure 4.18: The ratio of the astrophysical reaction rates of the ^{31}P(p,α)^{28}Si and ^{31}P(p,γ)^{32}S reactions. Only resonant contributions are considered. The red(dashed) curves are the previous upper and lower limits while the black(solid) curves change only the strengths of the 599 and 622 keV resonances to the results of this study.

two orders of magnitude), but has little effect on the upper limits where the contributions of lower lying resonances are expected to dominate. At higher temperatures where this resonance dominates the reaction rate, the factor of 10 reduction in the strength compared to the previous upper limit suggests even weaker cycling that what was previously stated [Ros95]. Overall, even if the previously unmeasured strengths of the lower-lying resonances are close to the upper limits, less than 10% of SCl material will proceed through an SCl reaction cycle in hot hydrogen burning environments.

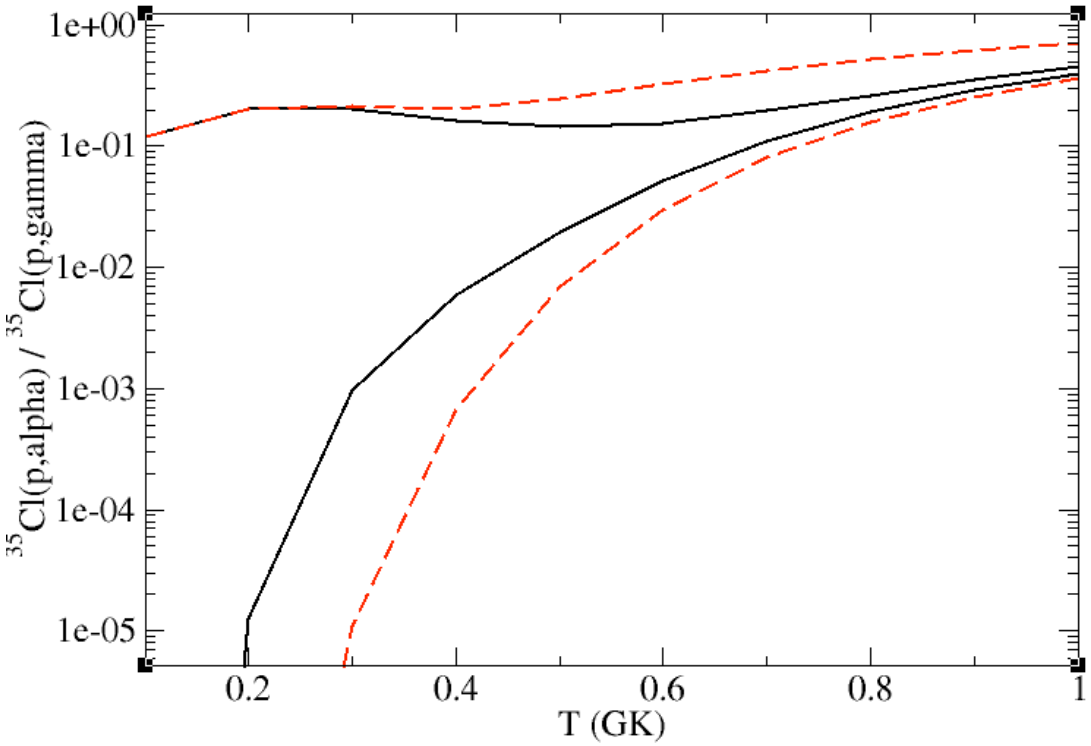

Figure 4.19: The ratio of the astrophysical reaction rates of the ^{35}Cl(p,α)^{32}S and ^{35}Cl(p,γ)^{36}Ar reactions. Only resonant contributions are considered. The red(dashed) curves are the previous upper and lower limits while the black(solid) curves change only the strength of the 611 keV resonance to the result of this study.

Chapter 5

Conclusions and Future Directions

5.1 Summary of Performed (p,α) Studies

A new experimental technique has been developed in order to study narrow resonant (p,α) reactions. In this technique, a heavy ion beam bombards hydrogen gas which fills a large scattering chamber at pressures up to 4 Torr. The chamber is differentially pumped so that no windows or foils obstruct the beam as it enters the chamber. The alpha particles from the (p,α) reaction is detected by a silicon detector array (SIDAR) and the heavy recoil pass through the center of SIDAR and are detected by a type S1 silicon detector. The reaction vertex from the (p,α) reaction is determined independently using the energy of the emitted alpha particle and the maximum angle of the heavy recoil. Unreacted beam passes through the centers of both detectors and impinges upon a carbon foil and scattered carbon is detected by two surface barrier monitor detectors for purposes of beam normalization. Advantages of this new technique are that the pure nature of the target maximizes the resonance yield, the target stoichiometry is well-known due to utilizing hydrogen gas instead of a

mixed foil target, and the target density can be varied in order to match the expected width of the resonance.

This new technique was utilized in order to measure the strength of the E_{CM} = 183 keV resonance in $^{17}O(p,\alpha)^{14}N$ which had previously been measured [Cha05] and found to be up to 50 times greater than that inferred from a $^{17}O(p,\gamma)^{18}F$ study [Fox04]. This increased strength was reported to decrease ^{18}F production in novae by as much as a factor of 10. The results from the present study ($\omega\gamma_{p\alpha} = 1.70 \pm 0.15$ meV) were in good agreement with the previous increased strength ($\omega\gamma_{p\alpha} = 1.6 \pm 0.2$ meV). A $^{17}O(p,\alpha)^{14}N$ reaction rate was calculated using the new strength and nova model simulations using the new rate showed decreased ^{18}F production in 1.15$M_\odot$ ONeMg by approximately a factor of 10, though higher mass novae showed a much smaller effect.

Low-energy resonances in $^{31}P(p,\alpha)^{28}Si$ and $^{35}Cl(p,\alpha)^{32}S$ were studied in order to gain a better understanding of reaction cycling in the Si-Ar region. Previous studies of these resonances were either outdated or performed indirectly, resulting in high uncertainties in the $(p,\alpha)/(p,\gamma)$ reaction rate ratios which determine the strength of cycling in the region. Resonance strengths at E_{CM} = 599 and 622 keV in $^{31}P(p,\alpha)^{28}Si$ were measured as well as the E_{CM} = 610 keV resonance in $^{35}Cl(p,\alpha)^{32}S$, which is the lowest energy that any resonance in this reaction has been observed. The strengths for each resonance were found to lower than the previous results, sometimes by as much as a factor of 2. Reaction rates using these new strengths resulted in weak cycling in the Si-Ar regions except at higher temperatures, in agreement with the findings of Ross *et al* [Ros95].

5.2 Future Plans: The 330 keV resonance in ^{18}F(p,α)^{15}O

The ^{18}F(p,α)^{15}O reaction plays an important role in the hot-CNO cycle that drives nova explosions (sections 1.2.2 and 1.3). The ^{18}F(p,α)^{15}O reaction rate significantly influences nucleosynthesis in novae, including the production of ^{18}F, which is believed to be the largest source of observable gamma rays after the initial explosion [Coc00] [Jos99]. The special importance of the ^{18}F(p,α)^{15}O reaction has resulted in measurements at several radioactive ion beam facilities including the HRIBF. These measurements have greatly reduced uncertainties in the ^{18}F(p,α)^{15}O reaction rate, but some significant questions remain.

The largest uncertainty in the ^{18}F(p,α)^{15}O currently results from the potential contributions of resonances with spins of $J^{\pi} = 3/2^{-}$. There are believed to be 4 or more $3/2^{-}$ resonances in the energy region relevant for novae. The ^{18}F(p,α)^{15}O reaction rate depends sensitively on the properties of these resonances. Therefore, the resonance strengths, widths, widths, and signs of inference between these resonances must be accurately determined in order to reduce the uncertainties in the ^{18}F(p,α)^{15}O reaction rate, In addition, there are many known states in the mirror nucleus ^{19}F that have yet to be observed in ^{18}F.

Three direct studies of the ^{18}F(p,α)^{15}O reaction cross section have been conducted at the HRIBF thus far. The combined results from these measurements are shown in figure 5.1. In the first measurement, the properties of a resonance at E_{CM} = 665 keV were accurately measured [Bar01]. In the second, the strength of what may be the single most important resonance for ^{18}F production in novae (E_{CM} = 330 keV) was measured with about 30% precision [Bar01]. The most recent measurements at energies above the E_{CM} = 665 keV resonance set the first constraints on the sign of interference between the $3/2^{-}$ states in the region [Cha06] (see Figure 5.2). These

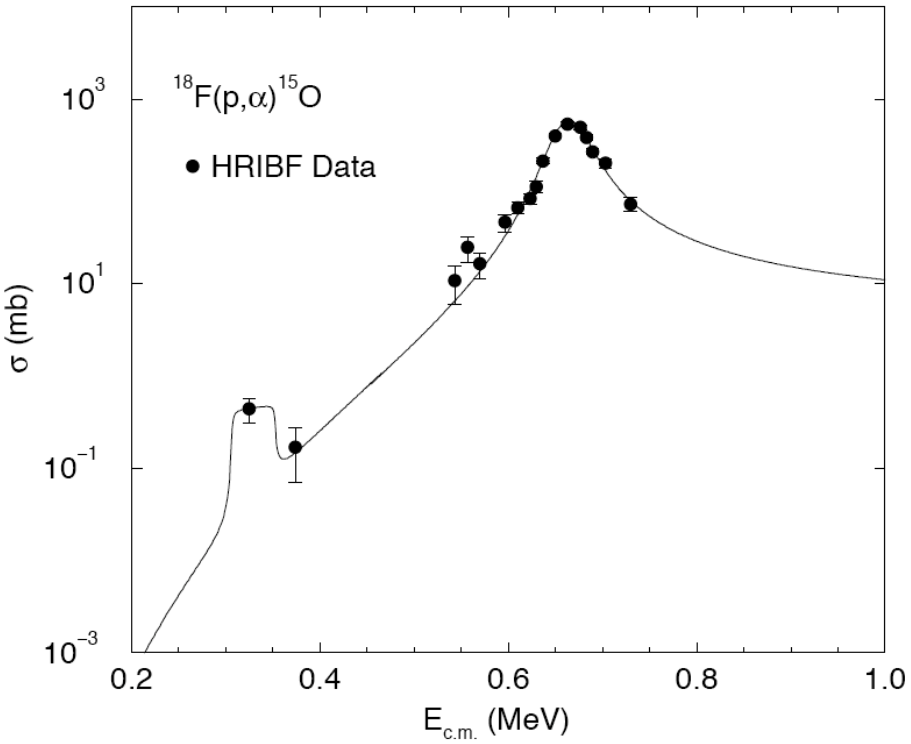

Figure 5.1: A plot of the cross section σ versus E_{CM} showing the previous studies done at the HRIBF on the ^{18}F(p,α)^{15}O reaction [Bar01] [Bar02] [Cha06].

measurements resulted in the reduction of the uncertainties in ^{18}F production in novae between 1 and 2 orders of magnitude. However, large uncertainties still remain in the ^{18}F(p,α)^{15}O reaction rate due to the uncertain properties of the narrow resonance near 330 keV.

The previous measurements all used CH_2 targets. However, the total widths of the resonances in the shaded energy range in Figure 5.2 are expected to be less than 5 keV (for the 330 keV resonance), while the targets commonly used produce beam energy loss of 50 keV or greater in the center-of-mass frame. Therefore, the technique discussed in chapter 2 is better suited for measurements in this energy range, as the pressure of the hydrogen gas inside the target chamber can be adjusted to match the expected total width.

Using the technique discussed in chapter 2, the placement of the detectors will be the same as for the ^{17}O(p,α)^{14}N measurement, with the SIDAR array located 115 mm from the entrance of the chamber, covering an angular range of $\approx$32 - 60^o. The S1 detector will be located $\approx$14 mm downstream, covering an angular range of $\approx$14 - 27^o in order to detect the maximum ^{15}O recoil angle of 22.4^o.

Since the ^{18}F(p,α)^{15}O reaction study will be using a radioactive ^{18}F beam, a considerable amount of stable ^{18}O contamination is expected to be present in the incoming beam as well, possibly with a ratio of ^{18}O/^{18}F as high as 10:1. The ^{18}F(p,α)^{15}O and ^{18}O(p,α)^{15}N events can be distinguished from one another by the differing Q-values of the two reactions (2.882 MeV for the ^{18}F(p,α)^{15}O reaction compared to 3.981 MeV for ^{18}O(p,α)^{15}N) using a similar technique in past measurements with CH_2 targets (see Figure 5.3) [Bar01] [Bar02] [Cha06]. Use of a thin target will also greatly reduce yield from the ^{18}O(p,α)^{15}N reaction, which is nonresonant in this energy range. Measurements with a pure ^{18}O will also be taken for purposes of background subtraction.

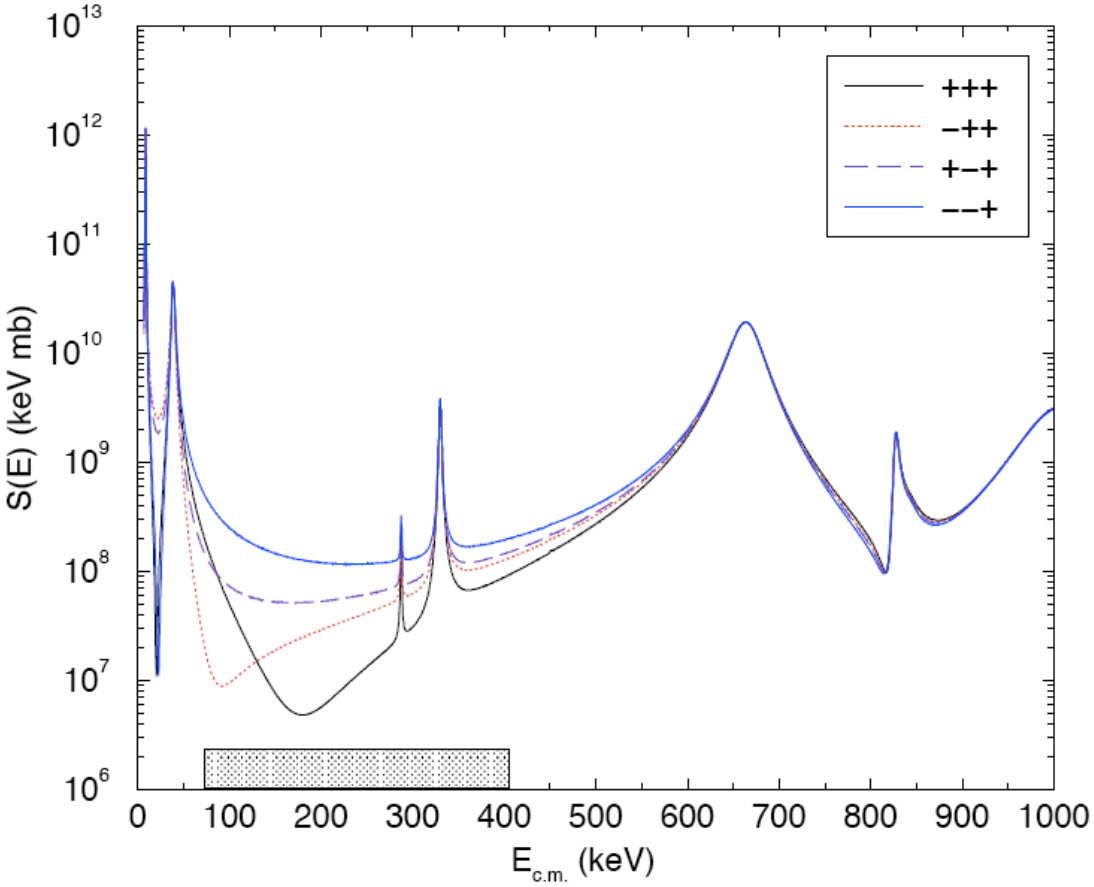

Figure 5.2: Astrophysical S-factor vs. energy for the four allowed possibilities for interference. The signs of the reduced widths for the E_{CM} = 8, 38, and 665 keV resonances are shown in the legend. The shaded region shows the energies most relevant for novae.

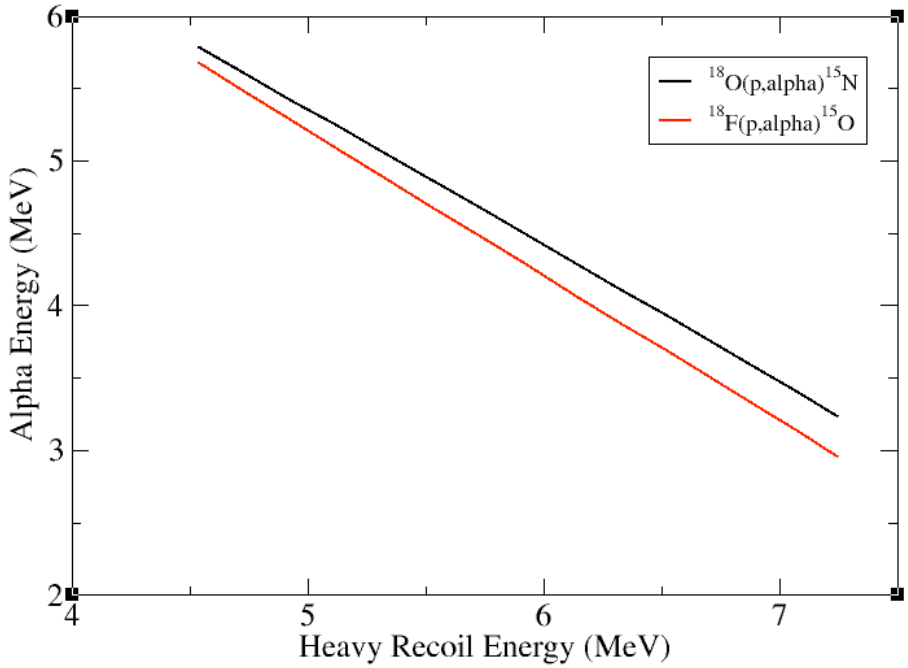

Figure 5.3: Alpha energy versus heavy recoil energy for the ^{18}F(p,α)^{15}O and ^{18}O(p,α)^{15}N reactions for the E_{CM} = 330 keV resonance in ^{18}F(p,α)^{15}O

In order to determine the total number of incident beam particles (sum of both the incoming ^{18}F and ^{18}O), a carbon foil will be utilized in the same manner as described in chapter 2. However, the kinematics of ^{18}F and ^{18}O scattering off of carbon is nearly indistinguishable. To determine the ratio of incoming ^{18}O to ^{18}F, incoming beam that scatters at low angles will enter a gas-filled ionization counter placed after the gas target. A schematic of the ion counter can be seen in Figure 5.4. The ion counter that will be used is a 30 cm long particle detector with 3 anodes of length 5 cm, 5 cm and 20 cm, and one cathode and is filled with isobutane gas. As the scattered beam enter the chamber, energy from both the ^{18}F and ^{18}O particles is transferred to the gas, creating electron-ion pairs along the track of the particle. An external electric field attracts the electrons and ions to the electrodes, creating a voltage signal whose amplitude is proportional to the total number of ion pairs produced. Since the stopping power (proportional to Z^2, where Z is proton number) is different for the incoming ^{18}F and ^{18}O, the two beam constituents will lose energy in the ion counter at a different rate and therefore create electron-ion pairs at a different rate in each anode. Plotting the energy lost in the first two anodes versus the total energy lost will show separation between the ^{18}F and ^{18}O (see Figure 5.5), allowing the ratio of incoming ^{18}F to ^{18}O to be determined. Scaling the total incident beam (as determined from the monitor detectors) by the ^{18}F to ^{18}O ratio will allow the determination of the total incident number of particles of each beam species

The current plans are to measure the strength and energy of the 330 keV resonance and possibly the 287 keV resonance if sufficient ^{18}F beam is available. Measurements of off-resonance yield between these two resonances will also be taken in order to differentiate between the curves shown in Figure 5.2. The ^{18}F(p,α)^{15}O reaction study was approved in December of 2006 by the HRIBF Program Advisory Committee (PAC).

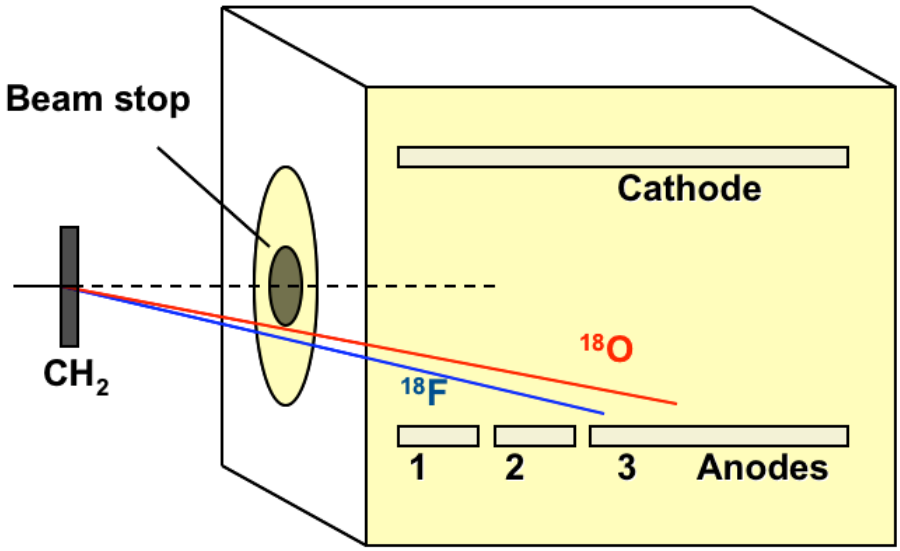

Figure 5.4: Schematic of the gas-filled ionization chamber.

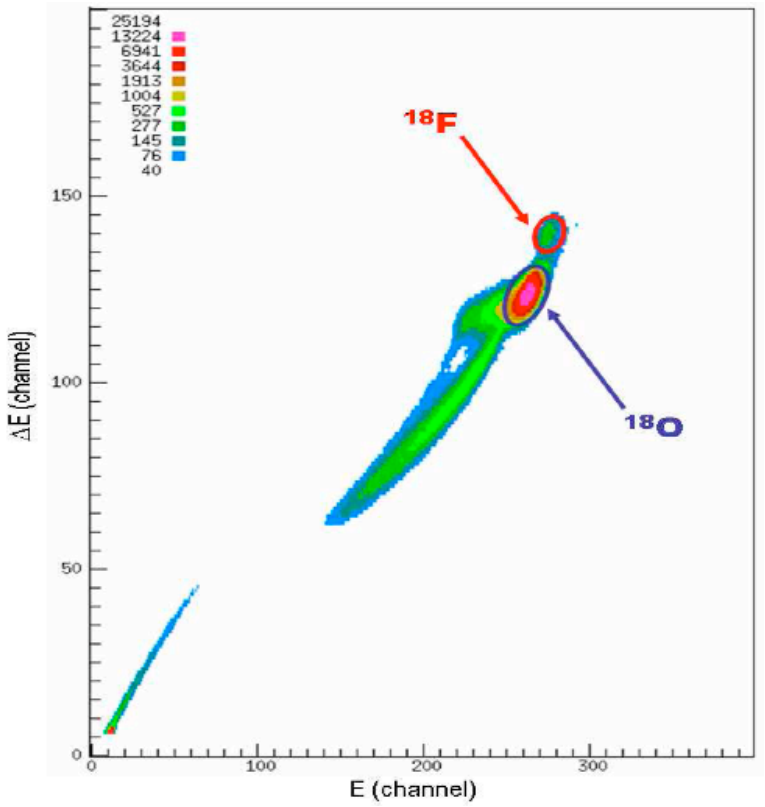

Figure 5.5: Sample ion counter spectrum from the ^{18}F(p,α)^{15}O reaction study by Chae [Cha06].

Bibliography

Bibliography

[Ang99] C. Angulo, M. Arnould, M. Rayet, P. Descouvemont, D. Baye, C. Leclercq-Willain, A. Coc, S. Barhoumi, P. Auger, C. Rolfs, R. Kunz, J. Hammer, A. Mayer, T. Paradellis, S. Kossionides, C. Chronidou, K. Spyrou, S. Degl'Innocenti, G. Florentini, B. Ricci, S. Zavatarelli, C. Providencia, H. Wolters, J. Soares, C. Grama, J. Rahighi, A. Shotter, and M. L. Rachti, Nucl. Phys. A **656**, 3 (1999).

[Bar00] D. W. Bardayan, J. C. Blackmon, C. R. Brune, A. E. Champagne, A. A. Chen, J. M. Cox, T. Davinson, V. Y. Hansper, M. A. Hofstee, B. A. Johnson, R. L. Kozub, Z. Ma, P. D. Parker, D. E. Pierce, M. T. Rabban, A. C. Shotter, M. S. Smith, K. B. Swartz, D. W. Visser, and P. J. Woods, Phys. Rev. C **62**, 055804 (2000).

[Bar01] D. W. Bardayan, J. C. Blackmon, W. Bradfield-Smith, C. R. Brune, A. E. Champagne, T. Davinson, B. A. Johnson, R. L. Kozub, C. S. Lee, R. Lewis, P. D. Parker, A. C. Shotter, M. S. Smith, D. W. Visser, and P. J. Woods, Phys. Rev. C **63**, 065802 (2001).

[Bar02] D. W. Bardayan, J. C. Batchelder, J. C. Blackmon, A. E. Champagne, T. Davinson, R. Fitzgerald, W. R. Hix, C. Iliadis, R. L. Kozub, Z. Ma,

S. Parete-Koon, P. D. Parker, N. Shu, M. S. Smith, and P. J. Woods, Phys. Rev. Lett. **89**, 262501 (2002).

[Bet67] H. Bethe, *Energy Production in Stars*, Nobel Lecture, available at http://www.jinaweb.org/html/Rhistory.html, December 11, 1967.

[Bol07] B. Boltwood, Am. J. Sci. **23**, 77 (1907).

[Bur57] E. Burbidge, G. Burbidge, W. Fowler, and F. Hoyle, Rev. Mod. Phys. **29**, 547 (1957).

[Cha92] A. Champagne and M. Wiescher, Ann. Rev. Nucl. Part. Sci. **42**, 39 (1992).

[Cha05] A. Chafa, V. Tatischeff, P. Aguer, S. Barhoumi, A. Coc, F. Garrido, M. Hernanz, J. José, J. Kiener, A. Lefebvre-Schuhl, S. Ouichaoui, N. de Séréville, and J.-P. Thibaud, Phys. Rev. Lett. **95**, 031101 (2005).

[Cha06] K. Chae, D. Bardayan, J. Blackmon, D. Gregory, M. Guidry, M. Johnson, R. Kozub, R. Livesay, Z. Ma, C. Nesaraja, S. Pain, S. Paulaskas, M. Porter-Peden, J. Shriner Jr, N. Smith, M. Smith, and J. Thomas, Phys. Rev. C **74**, 012801 (2006).

[Cha07] A. Chafa, V. Tatischeff, P. Aguer, S. Barhoumi, A. Coc, F. Garrido, M. Hernanz, J. José, J. Kiener, A. Lefebvre-Schuhl, S. Ouichaoui, N. de Séréville, and J.-P. Thibaud, Phys. Rev. C **75**, 035810 (2007).

[Chi09] K. Chipps, D. Bardayan, J. Blackmon, K. Chae, U. Greife, R. Hatarik, R. Kozub, C. Matei, B. Moazen, C. Nesaraja, S. Pain, W. Peters, S. Pittman, J. Shriner Jr., and M. Smith, Phys. Rev. Lett. **102**, 152502 (2008).

[CINA] http://www.nucastrodata.org.

[Cla83] D. Clayton, *Principles of Stellar Evolution and Nucleosynthesis*, Univ. of Chicago Press, Chicago, 1983.

[Coc00] A. Coc, M. Hernanz, J. José, and J.-P. Thibauld, Astron. Astrophysics **357**, 561 (2000).

[Edd20] A. Eddington, Nature **106**, 14 (1920).

[End90] P. Endt, Nuc. Phys. A **521**, 830 (1990).

[Fit05] R. Fitzgerald, *Measurement of the* $^1H(^7Be,^8B)\gamma$ *cross section*, Ph.D. thesis, University of North Carolina, 2005.

[Fox04] C. Fox, C. Iliadis, A. Champagne, A. Coc, J. José, R. Longland, J. Newton, J. Pollanen, and R. Runkle, Phy. Rev Lett. **93**, 081102 (2004).

[Ili91] C. Iliadis, U. Giesen, J. Görres, J. Ross, S. Graff, M. Wiescher, R. Azuma, J. King, M. Buckby, C. Barnes, and T. Wang, Nuc. Phys. A **533**, 153 (1991).

[Ili93] C. Iliadis, J. Görres, J. Ross, K. Scheller, M. Wiescher, C. Grama, T. Schange, H. Trauvetter, and H. Evans, Nuc. Phys. A **559**, 83 (1993).

[Ili94] C. Iliadis, J. Görres, J. Ross, K. Scheller, M. Wiescher, R. Azuma, G. Rotors, H. Trauvetter, and H. Evans, Nuc. Phys. A **571**, 132 (1994).

[Jos98] J. José and M. Hernanz, Astrophys. J **494**, 680 (1998).

[Jos99] J. José and M. Hernanz, Astrophys. J **520**, 347 (1999).

[Kra88] K. Krane, *Introductory Nuclear Physics*, John Wiley & Sons, Hoboken, New Jersey, USA, 1988.

[Kup63] J. Kuperus, P. Glaudemans, and P. Endt, Physica **29**, 1281 (1963).

[Lar06] N. Larson, Oak Ridge National Laboratory Report No. ORNL/TM-9179/R7, 2006.

[Mic05] http://www.micronsemiconductor.co.uk.

[Moa07] B. Moazen, D. Bardayan, J. Blackmon, K. Chae, K. Chipps, C. Domizioli, R. Fitzgerald, U. Greife, W. Hix, K. Jones, R. Kozub, E. Lingerfelt, R. Livesay, C. Nesaraja, S. Pain, L. Roberts, J. S. Jr., M. Smith, and J. Thomas, Phys. Rev. C **75**, 7 (2007).

[Gui] M.W.Guidry, *Theoretical Astrophysics*, unpublished.

[Pau03] H. Paul and A. Shinner, At. Nucl. Data Tables **85**, 377 (2003).

[Par03] S. Parete-Koon, W. Hix, M. Smith, S. Starrfield, D. Bardayan, and A. Mezzacappa, Astrophys. J. **598**, 1239 (2003).

[Pea05] I. Pearson Prentice Hall, 2005.

[Rau01] T. Rauscher and F. Theilmann, At. Nucl. Data Tables **79**, 47 (2001).

[Rol88] C. Rolfs and W. Rodney, *Cauldrons in the Cosmos*, Univ. of Chicago Press, Chicago, 1988.

[Ros95] J. G. Ross, J. Görres, C. Iliadis, S. Vouzoukas, M. Wiescher, R. B. Vogelaar, S. Utku, N. P. T. Bateman, and P. D. Parker, Phys. Rev. C **52**, 1681 (1995).

[Sch98] H. Schatz, A. Aprahamian, J. Görres, M. Wiescher, T. Rauscher, J. Rembges, F. Thielemann, B. Pfeiffer, K. Moller, P. andKratz, H. Herndl, B. Brown, and H. Rebel, Physics Reports **294**, 167 (1998).

[Sta98] S. Starrfield, J. Truran, M. Wiescher, and W. Sparks, Mon. Not. R. Astron. Soc. **296**, 502 (1998).

[Tho05] J. Thomas, *Single-Neutron Excitations of the N=51 Isotones in* ^{83}Ge *and* ^{85}Se, Ph.D. thesis, Rutgers University, 2005.

[Zie03] J. Ziegler, "SRIM-2003.10", http://www.srim.org.

Vita

Brian Moazen was born in Chattanooga, Tennessee on May 3, 1979. After completing high school at the Chattanooga School for the Arts and Sciences in 1997, he enrolled at Tennessee Technological University in 2001 where he received his Bachelor of Science degree in Physics. He then entered the University of Tennessee at Knoxville in the fall of 2004, successfully defended his thesis on August 25, 2009, and will graduate with his Ph.D. in Physics in December 2009.